Reactive Transport Modelling in Fractured Rock – Redox Stability Study

NWMO TR-2009-04   **March 2009**

S.M. Spiessl[1]
K.U. Mayer[1]
K.T.B. MacQuarrie[2]

[1]Department of Earth and Ocean Sciences, University of British Columbia

[2]Department of Civil Engineering, University of New Brunswick

nwmo

NUCLEAR WASTE   SOCIÉTÉ DE GESTION
MANAGEMENT   DES DÉCHETS
ORGANIZATION   NUCLÉAIRES

Reactive Transport Modelling in Fractured Rock – Redox Stability Study

NWMO TR-2009-04

March 2009

S.M. Spiessl[1]
K.U. Mayer[1]
K.T.B. MacQuarrie[2]

[1]Department of Earth and Ocean Sciences, University of British Columbia

[2]Department of Civil Engineering, University of New Brunswick

ABSTRACT

Title:	**Reactive Transport Modelling in Fractured Rock – Redox Stability Study**
Report No.:	**NWMO TR-2009-04**
Author(s):	S.M. Spiessl[1], K.U. Mayer[1], K.T.B. MacQuarrie[2]
Company:	[1]Department of Earth and Ocean Sciences, University of British Columbia
	[2]Department of Civil Engineering, University of New Brunswick
Date:	March 2009

Abstract

The Nuclear Waste Management Organization (NWMO) is responsible for implementing Adaptive Phased Management, the approach selected by the Government of Canada for long-term management of used nuclear fuel waste generated by Canadian nuclear reactors (NWMO 2005). The ultimate objective of Adaptive Phased Management is centralized containment and isolation in a suitable geological formation in either sedimentary or crystalline rock. In the crystalline rocks of the Canadian Shield, geochemical conditions are currently reducing at depths of 500 to 1000 m. Such reducing conditions are well suited for a deep geologic repository for used nuclear fuel. However, during future glacial periods, altered hydrologic conditions could potentially result in recharge of glacial melt water containing a relatively high concentration of dissolved oxygen (O_2).

In this study, the reactive transport code MIN3P is employed to investigate redox processes in fractured crystalline rock under the simplifying assumption of vertical groundwater flow to a depth of 500 m. The primary objectives of the research are to provide a greater understanding of the basic processes controlling the transport of O_2 and to identify the important parameters controlling oxygen ingress and the uncertainty associated with these parameters. Base case scenarios are developed that represent present-day and hypothetical glacial melt water recharge into a single fracture-matrix system and into a fracture zone. For the single fracture base case, which is constrained to the extent possible by parameter values characteristic of Canadian Shield rocks, oxygen diffusion into the rock matrix and consumption by reduced iron minerals (e.g. biotite) was found to limit the depth of dissolved oxygen migration to less than 15 m below the assumed zone of oxygenated groundwater during a simulated melt water production period of 10,000 years. For the fracture zone case, which is characterized by a significantly increased O_2-mass loading, the ingress of O_2 is limited to approximately 70 m below the assumed zone of oxygenated groundwater. The results of the uncertainty analyses indicate that for the single fracture case, the most influential factors controlling O_2 ingress are flow velocity in the fracture, fracture aperture, and biotite reaction rate. The most important parameters for the fracture zone simulations are flow velocity, pO_2 in the recharge water, biotite reaction rate, and to a lesser degree the abundance and reactivity of chlorite in the fracture zone, and the fracture zone width. These parameters should therefore be reasonably well constrained if site-specific modelling is to be undertaken.

CONTENTS

LIST OF TABLES

LIST OF FIGURES

1. INTRODUCTION

The Nuclear Waste Management Organization (NWMO) is responsible for implementing Adaptive Phased Management, the approach selected by the Government of Canada for the lon-term management of used nuclear fuel waste generated by Canadian nuclear reactors (NWMO 2005). The ultimate objective of Adaptive Phased Management is centralized containment and isolation in a suitable geological formation in either sedimentary or crystalline rock. The long-term isolation of nuclear waste in deep geologic repositories requires consideration of many technical aspects, including the selection of a host rock mass that is geochemically stable. Crystalline rock environments of the Canadian Shield potentially offer stable mechanical and biogeochemical conditions for containment of wastes over periods of tens to hundreds of thousands of years (McMurry 2004). It is anticipated that the existing geochemically reducing conditions at depths of 500 to 1000 m in Shield bedrock will provide a stable and largely unreactive environment (McMurry 2000). One of the key requirements for geochemical stability is that oxidizing conditions do not develop in the vicinity of the repository after closure and over extended periods of time. The presence of dissolved oxygen may promote corrosion of emplaced waste containers (Glynn et al. 1997, Puigdomenech et al. 2001a), possible instability of some of the engineered barriers (McMurry 2000), and in the event of repository failure, increased mobility of radionuclides and metals (Glynn et al. 1997, McMurry 2000, Puigdomenech et al. 2001a).

After repository closure, oxidizing conditions may develop if groundwater containing dissolved oxygen (O_2) reaches repository depths. Such migration will depend on site-specific conditions such as the temporal and spatial hydraulic boundary conditions, host rock permeability distribution, the presence of hydraulically-conductive fractures, density contrasts between recharge waters and deep saline waters (Sykes et al. 2003), mineralogy, and groundwater composition (McMurry 2000). As depicted in Figure 1-1, groundwater flow along fractures or fracture zones is the most likely mechanism to promote dissolved O_2 ingress to significant depths. The ingress of oxygenated water may be limited by two main factors:

- The absence of an active flow system that reaches repository depth due to the lack of a connected fracture network, and/or the existence of significant density contrasts between fresh recharge water and dense brines present at depth (e.g. Sykes et al. 2003).
- The occurrence of biogeochemical reactions that consume oxygen along the flow path. Downward migration of dissolved oxygen may be counteracted by the reduction capacity present in the water, provided by dissolved organic carbon (DOC) for example, and in the crystalline bedrock, provided by mineral phases containing elements in reduced form. It is expected that the reduction capacity of the host rock and fractures will be strongly influenced by the amount of Fe(II)-bearing minerals, such as biotite and chlorite, present.

The present study focuses on the investigation of the second scenario as it is assumed that groundwater flow within conductive fractures does occur to depths of hundreds of metres. This is an oversimplification of the groundwater flow system in the Canadian Shield because, as shown by Sykes et al. (2003) and Chan and Stanchell (2004), surface recharge water may not reach depths greater than 300 m. Sykes et al. (2003) noted that a volume of inter-connected fractured rock exists only in the upper 300 m at the Whiteshell Research Area (WRA); below 300 m, the rock contained a small number of sets of relatively widely-spaced discrete open

fractures and sparsely fractured rock (containing microcracks and very sparsely distributed open fractures, which are not interconnected). However, if attenuation of dissolved oxygen migration can be demonstrated for the unlikely case of a single fracture or fracture zone extending to repository depths, then this provides an additional line of evidence that repository redox conditions will not be influenced by changing surficial recharge. If oxygen ingress is shown to be significant, then demonstrating limited groundwater circulation to repository depths increases in importance.
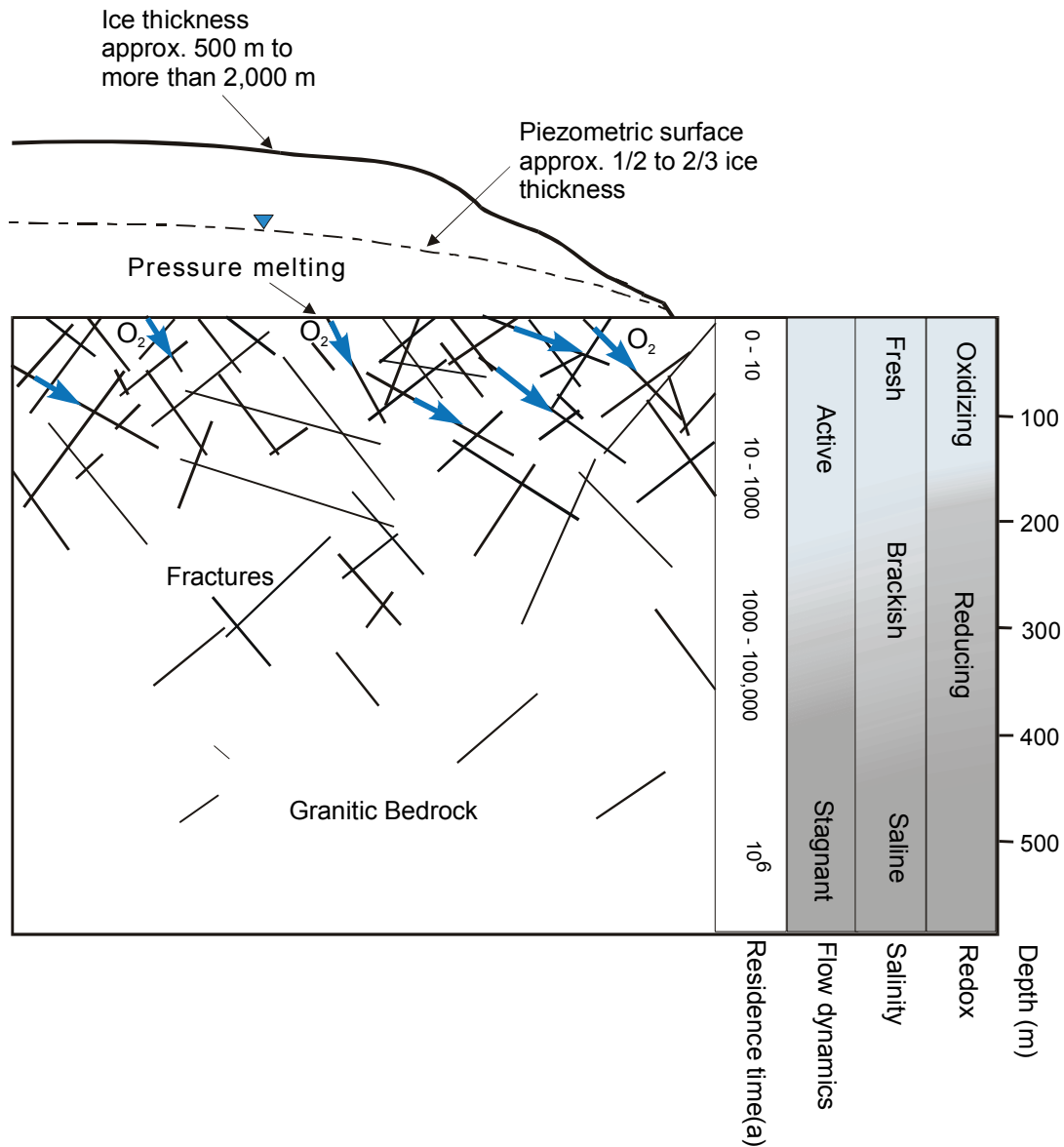
Figure 1-1: Conceptual view of surface and subsurface conditions during a glacial period. Blue arrows indicate advective mass transport of recharge waters. Groundwater characteristics derived, in part, from Gascoyne (2000).

Considering the time scales of interest (> 10,000 years), it is necessary to consider the effect of glaciation events on recharge water quantity and composition. In recent years several groups (e.g. SKI 1996, Nirex 1997, Vieno and Nordman 1999, SKB 1999, Peltier 2002) have investigated the possible effects of glaciation on deep geologic repositories as it is expected that large ice sheets will form over parts of the Northern Hemisphere during the time scales of interest. During periods of glaciation, the rock mass overlying a repository might undergo hydrogeological, geomechanical and geochemical changes, caused for example by permafrost and ice loading (McMurry 2000). Of particular importance for the current study, is the suggestion that during periods of glacial melt water production, recharge waters may be enriched with dissolved oxygen relative to present-day interglacial conditions. The potentially higher oxygen content in melt water during glacial periods has been attributed to:

(i) release of air bubbles that are trapped in ice (Glynn et al. 1997),
(ii) the elevated pressure below the melting ice, causing increases in dissolved O_2 concentrations by a factor of 3 to 5 (e.g. Guimerà et al. 1999), and
(iii) a reduction in near-surface organic carbon as a result of erosion of the soil horizon by glacial action (McMurry 2000) and minimized photosynthesis (Puigdomenech et al. 2001a).

Furthermore, increases in groundwater recharge rates have been suggested during periods of glacial melt water production. Ice melting is expected to occur under warm-based ice sheets and this melt water may be in contact with exposed bedrock fractures (McMurry 2000). Additionally, velocities may also be increased due to mechanical loading resulting from the accumulation of ice sheets (Chan and Stanchell 2004).

A better understanding of how subsurface redox conditions may evolve in response to the recharge of oxidizing groundwater is important for demonstrating the geochemical stability of deep geologic repositories. Reactive transport modelling is one method that can yield insights into the interactions between the controlling physical and biogeochemical processes in these settings (MacQuarrie and Mayer 2004).

1.1. STUDY OBJECTIVES AND SCOPE

The key objectives of this work program are to provide:

(i) an improved understanding of basic processes controlling redox stability, under assumed vertical transport of oxygenated recharge water in sparsely-fractured crystalline rock and fracture zones in crystalline rock, and based on parameters selected to be representative for the Canadian Shield and an approximation of potential glacial conditions,

(ii) the identification of the most important parameters controlling oxygen ingress and an evaluation of the uncertainty associated with these parameters, and

(iii) a demonstration of the capabilities of multicomponent reactive transport models in fractured crystalline rock.

These objectives are achieved by using an existing multicomponent reactive transport code and data currently available in the literature. The simulation of long-term climate change associated with glaciation - deglaciation and the resulting evolution of large-scale groundwater flow

systems in the Canadian Shield are beyond the scope of this work program; however, the results of ongoing studies on these topics are integrated whenever possible.

2. STUDY APPROACH

The study is composed of six modelling stages, which include both small-scale mechanistic simulations and more comprehensive larger-scale geochemical stability investigations.

2.1. MODELLING STAGES

In Stage I of this study, a single fracture scenario is formulated which approximates 2,000 years of present-day groundwater recharge conditions, followed by a 10,000-year period of glacial melt water production. This scenario is a simplified representation of recharge water quantity and composition during interglacial and glacial periods and is designed to represent a base case with respect to oxygen input into a fractured rock system. A literature review is conducted to identify key processes and parameter values and the Stage I single fracture-matrix model is developed using a set of parameter values considered characteristic of the Canadian Shield. The behaviour of key redox species is investigated, as are selected grid discretization issues. A previous modelling scenario proposed by Glynn et al. (1997) is also investigated in Stage I. This previous work used a different conceptualization of oxygen migration and reaction than used in the present study and the effect of these different conceptualizations on the model results is evaluated.

The literature review conducted in Stage I is used to guide the selection of parameter values that are employed in the Stage II uncertainty analyses. The analyses focus on identifying the parameters which have the most influence on dissolved oxygen ingress in a single fracture and the adjacent rock matrix. A factorial design approach is used to efficiently and systematically conduct the uncertainty analyses.

Different model formulations for simulating reactive transport in sparsely fractured rock systems are evaluated in Stages III and IV. Stage III provides a comparison between a discrete fracture model (DFM) and a dual continuum model (DCM), which may be more computationally efficient than the discrete fracture model (DFM) used in Stages I and II. Stage IV introduces simple two-dimensional fracture network simulations designed to illustrate the potential effect of spatial complexity on the movement of dissolved oxygen and associated attenuation reactions.

In Stage V, selected simulations are undertaken to determine the influence of the occurrence of a low recharge period during the onset of glaciation (e.g. due to permafrost development)and the influence of different durations of melt water production. Again the key focus of these simulations is the depth of migration of dissolved oxygen in a single fracture-matrix system under the assumption of vertical flow.

Finally in Stage VI, the investigation of basic processes controlling redox stability in crystalline rocks is further explored by simulating recharge of oxygenated water through a fracture zone. Similar to Stage I, a base case scenario is developed that is constrained by available field data from the Canadian Shield. In additional simulations, the parameters presented by Glynn et al. (1997) are used and a comparison is made between the fracture zone model used in this study and the fracture-matrix-skin model of Glynn et al. (1997). Analogous to Stage II, an uncertainty

analysis using a factorial design approach is conducted to identify the most influential parameters controlling O_2-ingress for the fracture zone case.

2.2. NUMERICAL MODEL – MIN3P

The multicomponent reactive-transport code MIN3P (Mayer et al. 2002) is used to conduct the simulations. The MIN3P code is based on mass conservation equations for groundwater flow, multicomponent reactive transport of dissolved species, and a mineral mass balance equation (Mayer et al. 2002). The mass conservation equation for saturated groundwater flow is:

$$S_s \frac{\partial h}{\partial t} - \nabla \cdot [K \nabla h] - Q_a = 0 \tag{1}$$

where S_s [m^{-1}] is the specific storage, h [m] represents hydraulic head, t [s] is time, K [m s^{-1}] is the hydraulic conductivity tensor, and Q_a [s^{-1}] is a source-sink term, where a positive quantity defines the injection of water.

The mass conservation equation for a chemical component A_j, written in terms of total component concentrations T_j, takes the form:

$$\frac{\partial}{\partial t}\left[\phi T_j^a\right] + \nabla \cdot \left[q_a T_j^a\right] - \nabla \cdot \left[\phi D_a \nabla T_j^a\right] - Q_j^{a,a} - Q_j^{a,s} - Q_j^{a,ext} = 0 \qquad j = 1, N_C \tag{2}$$

where T_j^a [mol L^{-1} H$_2$O] are the total aqueous component concentrations for component A_j^c, ϕ is the porosity [m^3 void m^{-3} porous medium], q_a [m s^{-1}] is the Darcy flux vector, and D_a [m^2 s^{-1}] is the dispersion tensor for the aqueous phase. $Q_j^{a,a}$ [mol dm^{-3} porous medium] and $Q_j^{a,s}$ [mol dm^{-3} porous medium] are internal source and sink terms toward the total aqueous component concentrations due to intra-aqueous kinetic reactions and kinetically controlled dissolution-precipitation reactions. $Q_j^{a,ext}$ [mol dm^{-3} porous medium] are external source and sink terms for the aqueous phase.

To describe the change of mineral quantities over time the following set of mass conservation equations is needed (Steefel and Lasaga 1994):

$$\frac{d\varphi_i}{dt} = V_i^m R_i^m \qquad i = 1, N_m \tag{3}$$

where φ_i is the volume fraction of the mineral [m^3 mineral m^{-3} porous medium], V_i^m is the molar volume of the mineral [dm^3 mineral mol^{-1}], and R_i^m is the overall dissolution-precipitation rate for the mineral [mol dm^{-3} porous medium s^{-1}].

The physical and chemical relationships quantifying the transport and reaction processes implicitly contained in equations 2 and 3 are documented in Mayer et al. (2002). Of importance for the current project is the capability of MIN3P to handle equilibrium speciation of aqueous species and a range of kinetically controlled intra-aqueous and dissolution-precipitation reactions. Monod and inhibition terms can be used to describe microbially-mediated reactions.

The governing equations for flow and reactive transport in MIN3P also include a formulation for the feedback between dissolution-precipitation reactions, porosity and permeability.

The reactive transport equations in MIN3P are solved using the global implicit solution method (Steefel and Lasaga 1994) in combination with a direct substitution approach in which the aqueous components are reduced to primary dependent variables or total components. This minimizes the number of components to be considered (e.g. Yeh and Tripathi 1989). A partial equilibrium approach (Lichtner 1985, Sevougian et al. 1993, Steefel and Lasaga 1994) is used to simultaneously handle equilibrium and kinetic reactions. Equilibrium relationships are employed when the geochemical reactions are fast in comparison to transport processes, whereas a generalized formulation for kinetic reactions is utilized when reactions are characterized by time scales longer than the transport times scales (Bahr and Rubin 1987, Knapp 1989, Lichtner 1993, Steefel and MacQuarrie 1996). The efficiency and robustness of MIN3P are increased by implementation of an adaptive time stepping and update modification algorithm as well as numerous spatial weighting schemes for advective transport. The geochemical database, accessed by MIN3P through an external input file, allows for the definition of problem-specific reaction networks. The code has been applied to a number of field and laboratory studies in which abiotic and microbially mediated oxidation-reduction reactions were considered (e.g. Mayer et al. 2001, Amos et al. 2004, Mayer et al., 2006).

In addition to the standard single continuum modelling approach of MIN3P, a dual continuum approach has been developed recently by Cheng (2005). The single continuum approach was used to approximate solute transport in discretely fractured porous media. In this case the individual fractures are mimicked using a linear set of control volumes, which have fracture material properties (e.g. permeability, porosity, mineral content), within a larger grid of elements that have properties of the rock matrix. With the concept of a dual continuum, the fractures and matrix are treated as two separate interacting continua with the porous matrix acting as a storage/release reservoir. To allow the two continua to interact, a coupling term is introduced which is controlled by a mass transfer coefficient, and the difference in concentrations between the two continua. Typically, dual continuum models are computationally more efficient in comparison to discrete fracture models (MacQuarrie and Mayer 2004; Steefel et al., 2005).

3. STAGE I: SINGLE FRACTURE SCENARIO BASE CASE

A base case is developed and simulated in Stage I to study fracture-matrix interactions during the reactive transport of oxidizing water in a single fracture. Figure 3-1 shows a schematic representation of such a fracture-matrix system. Dissolved oxygen enters the rock mass by advection-dominated transport and simultaneously interacts with reduced mineral phases that are present as coatings on the fracture walls or with dissolved organic carbon that is contained in the recharge water. Oxygen is also lost by diffusion into the rock matrix, where interactions with reduced mineral phases cause additional oxygen consumption. As a result of these processes, the mineralogy of the fracture and rock matrix will be altered. The base case simulations make use of the discrete fracture model (DFM) in an attempt to describe the relevant transport and reaction processes in a mechanistic manner.

3.1. DESCRIPTION OF THE BASE CASE

The parameters and biogeochemical processes considered for the base case are derived from a literature review that is discussed in detail in Appendix A. To the extent possible, parameter

values specific to the Canadian Shield are used. In the following sections a brief rationale for the selection of parameter values is provided, as well as the description of the model boundary conditions and domain discretization.
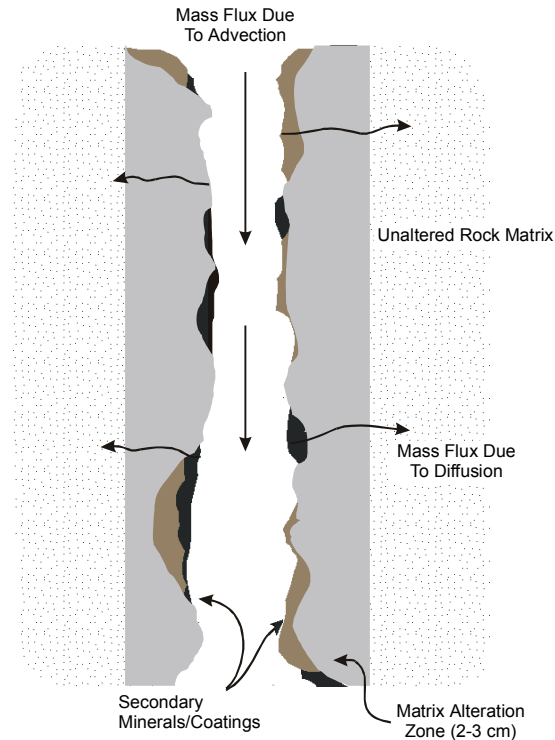
Figure 3-1: Schematic representation of conditions near the fracture-matrix interface.

3.1.1. Physical parameters

The maximum vertical dimension of the model domain is taken as 500 m below ground surface, which is consistent with the expected depth of a repository. A hypothetical single vertical fracture is assumed to extend from the ground surface to a depth of 500 m. This situation is unlikely to occur in nature; however, it can be envisioned that a network of vertical and subvertical fractures may extend to such depths. The domain is assumed to be water-saturated and symmetry about the centre line of the fracture is assumed.

Based on the values discussed in Appendix A.1, a uniform open (porosity of 1) fracture with an aperture of 1×10^{-4} m is selected for the base case (i.e. half fracture aperture (δ) of 5×10^{-5} m). Solute transport and reactions are not expected to propagate into the matrix more than about 20 cm from the fracture and therefore a rock matrix width of 3 m perpendicular to the fracture is selected.

The literature reviewed in Appendix A.2 suggests that a Darcy velocity in the fracture of 3.2×10^{-8} m s^{-1} (1 m yr^{-1}) may be a representative value for the initial interglacial period, while during the glacial period a velocity one order of magnitude higher (i.e. 3.2×10^{-7} m s^{-1}) is assigned to account for potentially larger hydraulic gradients caused by ice sheet loading and increased

recharge during the period of deglaciation. The longitudinal dispersivity in the fracture is selected as 0.1 m which, because of the potentially large transport distance, is somewhat increased from the value of 0.025 m determined by Neretnieks et al. (1982). The effective diffusion coefficient in the open fracture is set equal to the free-solution diffusion coefficient.

A matrix porosity (φ_m) of 5 x 10^{-3}, which falls in the range determined by Vilks et al. (2004), is selected for the base case scenario. By considering the estimated bulk rock permeability values from Davison et al. (1994), and matrix permeability values by Vilks et al. (2004) (see Table A. 1 and Table A. 2), an isotropic permeability value of 1 x 10^{-19} m^2 is assumed for a (nearly) unaltered rock matrix. This yields a hydraulic conductivity for the matrix (in the horizontal and vertical directions) of 1.1 x 10^{-12} m s^{-1}.

Consistent with the range of effective diffusion coefficients (D_{eff}) given by Vilks et al. (2004), a value of 5.4 x 10^{-13} m^2 s^{-1} (average of the geometric means: 3.7 x 10^{-13}, 1.4 x 10^{-13}, 1.1 x 10^{-12}, see Table A. 3) is chosen for solutes in the rock matrix. The experiments by Vilks et al. (2004) were conducted using iodide, which has a free phase diffusion coefficient similar to oxygen (Appendix A.5). Due to model limitations, this diffusion coefficient was applied for all solutes. In the reactive transport simulations, the apparent diffusion coefficient (D_a) is used because this allows the porosity and apparent diffusion coefficient to be varied independently (e.g. for Stage II analyses). D_a is defined as follows (Bradbury and Green 1985, Oscarson and Hume 1994, Ohlsson and Neretnieks 1995, Choi and Oscarson 1996, Vilks et al. 2004):

$$D_a = D_{eff}/\varphi_m \qquad (4)$$

A summary of the physical parameters is provided in Table 3-1. Simulations are initiated by 2,000 years of recharge during interglacial (i.e. present day) conditions, followed by a 10,000 year period of enhanced recharge during glacial melt water production.

Table 3-1: Physical parameters selected for the single fracture base case.

Parameter	Fracture	Matrix
Domain depth	500 m	500 m
Width	1 x 10^{-4} m (2δ)	3 m
Fracture Darcy velocity (q_f)	3.2 x 10^{-8} m s^{-1} (interglacial), 3.2 x 10^{-7} m s^{-1} (glacial)	-
dispersivity (α)	0.1 m	-
Porosity (φ)	1.0	5 x 10^{-3}
Hydraulic conductivity (K)	-	1.1 x 10^{-12} m s^{-1}
Effective diffusion coefficient (D_{eff})	1.1 x 10^{-10} m^2 s^{-1}	5.4 x 10^{-13} m^2 s^{-1}
Simulation time	12,000 years (interglacial: 2000 years, glacial: 10,000 years)	

3.1.2. Geochemical parameters

Initial Mineralogy. For reactive transport simulations in a crystalline rock environment, it is inherently difficult to specify the initial mineralogy in the fracture and matrix because mineral assemblages are incompletely characterized at the required scale, and because mineral alteration may have occurred in the past. There are two options available to obtain the initial mineral composition:

i) run simulations in a history-matching exercise in an attempt to generate realistic present-day mineral assemblages, or
ii) assign mineral fractions based on the best available observations.

The first option would involve long-term reactive transport modelling (on the order of 1,000,000 years or greater) because the rock matrix and fractures have been subjected to cumulative alteration since the time of fracture formation. Fracture and near-fracture rock mineralogy may have been affected by previous glaciation events, changing hydraulic conditions due to uplift and compression (Guimerà et al. 1999, Puigdomenech et al. 2001b, Peltier 2002), and hydrothermal events (Gascoyne 2004). As it is very difficult to account for changes in flow and geochemical conditions in the geologic past, option ii) is chosen for this work.

The initial mineral assemblage is based on observations made in the fractures and rock matrix of the Canadian Shield (Everitt et al. 1998, McMurry 2000, Everitt 2001, 2004, McMurry and Ejeckam 2002, Vilks et al. 2004), which are reviewed in Appendix A.7. Only the primary mineral phases that have the greatest impact on redox conditions as well as secondary phases that control the solubility of ions released by the dissolution of the primary phases, are considered. Because the focus of the current modelling is the description of redox conditions, reactions for other mineral phases that may occur in fractured granitic rock, for example the weathering of plagioclase feldspars that may result in the formation of carbonate mineral phases (Gascoyne 2004), have not been included. This implies that the model results for selected parameters, such as pH, may not be fully representative of field conditions.

Table 3-2 summarizes volume fractions of the different minerals considered in the base case and Figure 3-2 depicts the distribution of these mineral phases. The domain is initially divided into a surficial oxidized zone of 100 m, where weathering products are present, and a deeper reducing zone where reduced mineral phases are present. This subdivision of the domain is an approximation of present day redox conditions within the Canadian Shield (compare Figure 1-1); however, it is expected that the depth of the oxidized zone is spatially variable.

Table 3-2: Initial mineralogy in the fracture and rock matrix; (-) signifies that the mineral is initially absent.

Mineral	Fracture (volume fraction)		Matrix (volume fraction)	
	Oxidized zone	Reducing zone	Oxidized zone	Reducing zone
Biotite	-	-	-	5×10^{-2}
Chlorite	-	1×10^{-1}	-	-
Pyrite	-	-	-	1×10^{-6}
Quartz	Not applicable	Not applicable	3×10^{-1}	3×10^{-1}
SiO_2(am)	-	-	Not applicable	Not applicable
Al(OH)$_3$(am)	5×10^{-4}	-	5×10^{-4}	-
Goethite	3×10^{-3}	-	3×10^{-3}	-
Gypsum	-	-	-	-

Goethite and Al(OH)$_3$(am) are assumed to be present in the oxidized zone of the fracture and matrix as a result of paleohydrogeological alteration, with volume fractions of 3×10^{-3} and $5 \times$

10^{-4}, respectively. These phases are used as surrogates for weathering products that have accumulated from the weathering of primary Al-silicate mineral phases. In the reducing zone of the matrix, the redox-buffering minerals biotite and pyrite are present in volume fractions of 0.05 and 1 x 10^{-6}, respectively. In the reducing zone of the fracture, an initial volume fraction of chlorite of 0.1 is assumed to be present. These volume fractures are consistent with the literature reviewed in Appendix A.7. Throughout the matrix a quartz volume fraction of 0.3 is specified and quartz is allowed to dissolve and precipitate. Although quartz precipitation is unlikely under low temperature conditions, the inclusion of a more suitable secondary phase such as SiO_2(am) in co-existence with quartz is complex and beyond the scope of this work. This simplification may affect the overall evolution of silicate weathering; however, it does not have any effect on the simulated redox evolution in the system. In the fracture, SiO_2(am) is used as a solubility control for dissolved silica; SiO_2(am) is initially absent, but is permitted to precipitate. Furthermore, because pyrite is present in the system, gypsum is allowed to precipitate.
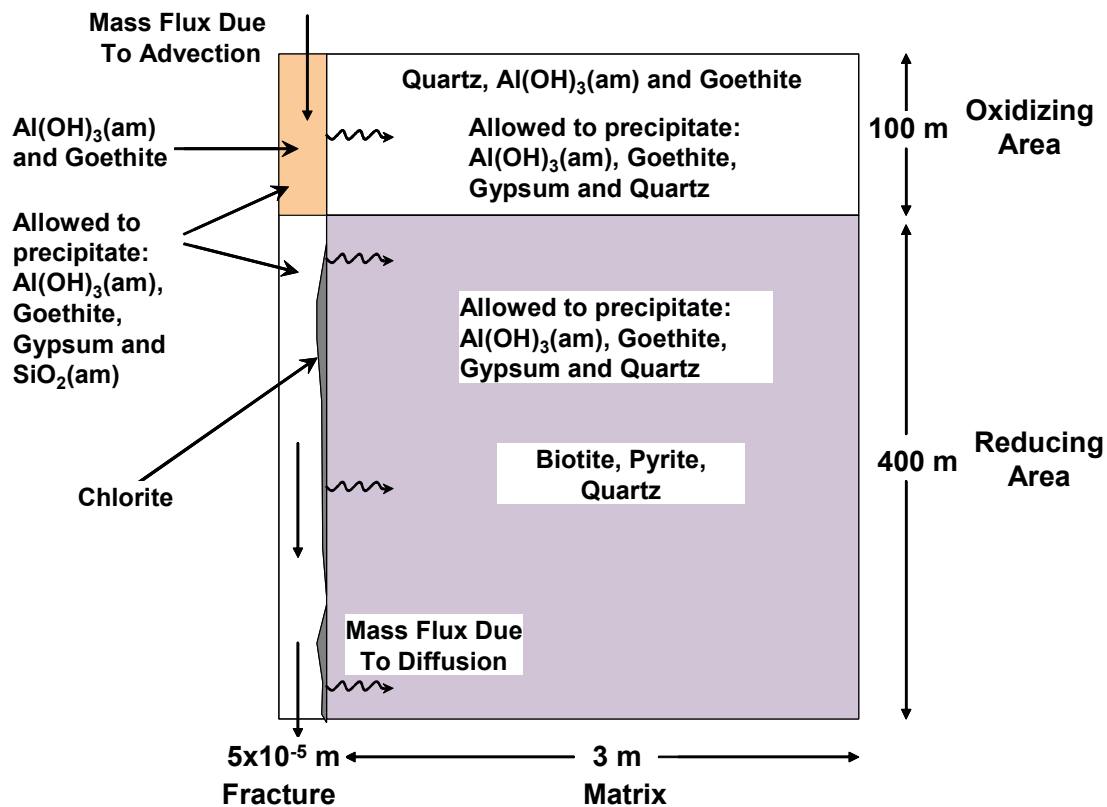
Figure 3-2: Conceptual representation of the base case.

Geochemical reactions and rates. The irreversible oxidative dissolution of biotite and pyrite provide redox-buffering capacity in the matrix, while chlorite provides redox buffering capacity in the fracture. It is assumed that these Fe(II)-bearing mineral phases will dissolve in the presence of O_2, thermodynamic solubility constraints are not applied, and the dissolution of biotite, chlorite and pyrite are represented by Monod-type rate expressions. The half saturation constants are set such that reaction rates are reduced for O_2 concentrations approaching

detection limit. The base case simulation assumes that microbial populations are at a quasi-steady state, which does not require the explicit consideration of microbial growth and decay. $Al(OH)_3(am)$, gypsum, goethite, quartz and $SiO_2(am)$ are considered to provide solubility control for ions released during biotite, chlorite, and pyrite dissolution. Table 3-3 summarizes the relevant reactions used in the base case simulations (see also Appendix A.8).

The effective reaction rate coefficients for the redox buffering minerals (Table 3-3) are obtained by multiplying literature values of mineral dissolution rates by mineral reactive surface areas in the matrix rock and the fracture, respectively (for details see Appendices A.8 and A.9). For example, using an intrinsic reaction rate for biotite of 5.6×10^{-13} mol m^{-2} s^{-1} (Samson et al. 2005) and an estimated biotite reactive surface area of 6.6×10^{-2} m^2 biotite L^{-1} bulk rock (see Appendix B.2), an effective biotite rate of 3.7×10^{-14} mol biotite L^{-1} bulk s^{-1} is obtained. For the calculation of the biotite reactive surface area, a BET surface area of 1 m^2 g^{-1}, which falls in the range of literature values for fresh and weathered granite (White and Brantley 2003), was reduced by a factor of 2,000 to account for the inaccessibility of the reactive surface area by pore fluids. An alternative method of estimating the reactive surface area using information from microfracture studies (Schild et al. 2001, Alonso et al. 2003) yields a larger reactive surface area of approximately 0.5 m^2 biotite L^{-1} bulk rock; however, the smaller value of 6.6×10^{-2} m^2 biotite L^{-1} bulk rock is used because it is conservative with respect to oxygen consumption in the rock matrix. Appendix 0 provides further details regarding the calculation of the effective biotite dissolution rate.

Table 3-3: Geochemical reactions for the mineral phases considered in the base case.

	Mineral	Reaction	Type	Log K	O_2-rate (mol L^{-1} bulk s^{-1})
Redox buffering minerals	Fe-Mg-biotite	$K(Mg_2Fe)(Si_3Al)O_{10}(OH)_2 + 0.25O_2 + 11H^+ \rightarrow K^+ + 2Mg^{2+} + Al^{3+} + 3H_4SiO_4 + Fe^{3+} + 0.5H_2O$	Irreversible (Monod kinetics)	29.53	3.7×10^{-14}
	Pyrite	$FeS_2 + 3.75O_2 + 0.5H_2O \rightarrow Fe^{3+} + 2SO_4^{2-} + H^+$	Irreversible (Monod kinetics)	206.79	$10^{-12} [O_2]^{0.5}$
	Fe-Mg-chlorite	$Mg_2Fe_3Al_2Si_3O_{10}(OH)_8 + 0.75O_2 + 19H^+ \rightarrow 2Mg^{2+} + 2Al^{3+} + 3H_4SiO_4 + 3Fe^{3+} + 7.5H_2O$	Irreversible (Monod kinetics)	38.08	1.12×10^{-12}
Other Mineral Phases	Quartz	$SiO_2 + 2H_2O \leftrightarrow H_4SiO_4$	Reversible	-3.98	1×10^{-16}
	$SiO_2(am)$	$SiO_2(am) + 2H_2O \leftrightarrow H_4SiO_4$	Reversible	-3.02	1×10^{-10}
	$Al(OH)_3(am)$	$Al(OH)_3(am) + 3H^+ \leftrightarrow Al^{3+} + 3H_2O$	Reversible	10.80	1×10^{-10}
	Goethite	$FeOOH + 3H^+ \leftrightarrow Fe^{3+} + 2H_2O$	Reversible	-1.00	1×10^{-10}
	Gypsum	$CaSO_4{:}2H_2O \leftrightarrow Ca^{2+} + SO_4^{2-} + 2H_2O$	Reversible	4.58	1×10^{-10}
Intra-aqueous kinetic reaction	DOC	$CH_2O + O_2 \rightarrow CO_3^{2-} + 2H^+$	Irreversible (Monod-kinetics)		[a] 1.5×10^{-10}

a) in units of mol L^{-1} H_2O s^{-1}

For chlorite, a literature-based intrinsic rate of 5.6×10^{-13} mol m^{-2} s^{-1} is assumed (Murphy et al. 1998, White and Brantley 2003, see also Appendix A.8). For calculation of the effective rate, the reactive surface area for chlorite is computed by multiplying a physical surface area for the fracture of 10 m^2 L^{-1} H$_2$O (Andersson et al. 1989, Malmström et al. 1996, see also Appendix A.8) by a chlorite fraction of 0.2. This results in a reactive surface area of 2 m^2 chlorite m^{-2} fracture. Multiplication of this value by the intrinsic rate of 5.6×10^{-13} mol m^{-2} s^{-1} yields an effective chlorite rate of 1.1×10^{-12} mol L^{-1} bulk s^{-1}.

For pyrite, a rate expression of $r = 10^{-7.42} [O_2]^{0.5}$ mol m^{-2} s^{-1} is used which is based on the expression derived by Williamson and Rimstidt (1994) for a pH of 7 (see also Appendix A.8). Using a reactive surface area of 2.64×10^{-5} m^2 pyrite L^{-1} bulk yields a rate of approximately 10^{-12} $[O_2]^{0.5}$ mol L^{-1} bulk s^{-1}. The surface area was obtained using the same approach as was used for biotite (Appendix B.2).

All other mineral dissolution-precipitation reactions, with the exception of quartz, are described as quasi-equilibrium reactions using reaction rates of 10^{-10} mol L^{-1} bulk s^{-1}. This approach can be justified considering the relatively rapid kinetics of these phases, the poor constraints on rates of precipitation, and the long time scale of interest. The dissolution of quartz is assigned a rate of 1×10^{-16} mol L^{-1} bulk s^{-1}, which is slower than that of the other silicate phases considered here reflecting the fact that quartz is the most stable phase under weathering conditions (Appelo and Postma 2005).

Table 3-3 also provides the intra-aqueous kinetic reaction for DOC which is commonly represented using Monod kinetics (e.g. Lensing et al. 1994, Park and Jaffe 1996). This rate was chosen based on literature values for organic carbon decomposition in aerobic environments (see Appendix A.8).

Table 3-4: Initial composition of the fracture and matrix water.

Primary component	Fracture water (mol L^{-1})		Matrix water (mol L^{-1})	
	Oxidized zone (0-100 m)	Reducing zone (100 – 500 m)	Oxidized zone (0-100 m)	Reducing zone (100 – 500 m)
K	9.0×10^{-5}	9.0×10^{-5}	9.0×10^{-5}	9.0×10^{-5}
Ca(II)	3.2×10^{-4}	3.2×10^{-4}	3.2×10^{-4}	3.2×10^{-4}
Mg(II)	1.6×10^{-4}	1.6×10^{-4}	1.6×10^{-4}	1.6×10^{-4}
Fe(III)	5.0×10^{-14}	5.0×10^{-14}	5.0×10^{-14}	5.0×10^{-14}
S(VI)	9.0×10^{-5}	9.0×10^{-5}	9.0×10^{-5}	9.0×10^{-5}
pCO$_2$	6.3×10^{-3} (atm)	5.9×10^{-3}	6.2×10^{-3}	5.9×10^{-3}
Si(II)	2.3×10^{-3}	2.3×10^{-3}	1.3×10^{-4}	1.3×10^{-4}
Al(III)	1.6×10^{-5}	1.2×10^{-5}	1.7×10^{-5}	1.2×10^{-5}
O$_{2(aq)}$	2.7×10^{-4}	-	2.7×10^{-4}	-
pO$_2$	0.21 (atm)	-	0.21	-
pH [a]	6.9	7.0	6.9	7.0

[a] dimensionless

Initial aqueous concentrations. The initial composition of the fracture and matrix water (Table 3-4) is derived from the reference Granite Groundwater (GGW) which represents shallow conditions in felsic rocks including granites, granitic gneisses, and granodiorites (Abry et al. 1982, Gascoyne 1986, McMurry 2004). For the fracture water in the oxidized zone, the pore water is equilibrated with respect to $Al(OH)_3(am)$, $SiO_2(am)$ and atmospheric oxygen (pO_2 of 0.21 atm), while the water in the reducing zone is equilibrated only with $SiO_2(am)$. Similarly, the matrix water in the oxidized zone is equilibrated with respect to $Al(OH)_3(am)$, quartz, which is abundant throughout the host rock, and atmospheric oxygen (pO_2 of 0.21 atm), while the water in the reducing zone is equilibrated only with quartz. The four initial solutions differ slightly with respect to the concentrations of carbonate, silica, aluminium and pH (Table 3-4).

3.1.3. Flow and transport boundary conditions

The average duration of glacial melt water production for 13 glacial-cycle realizations simulated by Peltier (2005, pers. comm.) is approximately 3,000 years, with a maximum duration of approximately 20,000 years. The base case scenario considers a period of 2,000 years of present day conditions (interglacial period), followed by a period of glacial melt water production lasting 10,000 years. The duration of melt water production used here is likely a conservative estimate because it neglects conditions of reduced recharge during periods of permafrost at the onset of glacial periods, and lies significantly above the average of the predictions by Peltier (2005, pers. comm.).

For reactive transport modelling, the interglacial period and the period of glacial melt water production are represented by a simplified scenario based on different fracture flow velocities (i.e. recharge rates) and transport boundary conditions. Specifically, after 2,000 years the fracture Darcy velocity and dissolved oxygen concentration in the melt water are increased, while DOC concentration in the melt water is decreased.

Table 3-5: Composition of recharge water for the base case.

Primary component	Interglacial period (mol L^{-1})	Glacial period (mol L^{-1})
K	3.8×10^{-6}	3.8×10^{-6}
Ca(II)	3.2×10^{-6}	3.2×10^{-6}
Mg(II)	4.1×10^{-6}	4.1×10^{-6}
Fe(III)	3.2×10^{-13}	3.2×10^{-13}
S(VI)	8.6×10^{-6}	8.6×10^{-6}
Si(II)	1.7×10^{-7}	1.7×10^{-7}
Al(III)	3.7×10^{-9}	3.7×10^{-9}
C(IV)	1.3×10^{-5}	1.2×10^{-5}
pCO_2	3.2×10^{-4} (atm)	3.2×10^{-4}
pO_2	0.21 (atm)	0.5
$O_{2(aq)}$	2.7×10^{-4}	6.3×10^{-4}
DOC	7.14×10^{-5}	-
pH [a]	5.8	5.8

[a] dimensionless

The compositions of the two recharge waters are provided in Table 3-5; these concentrations were derived from a data set provided by Pitkänen et al. (2004) representing an estimated quaternary glacial water. During the interglacial period, a pO_2 of 0.21 atm representative of

atmospheric conditions is assumed, while during the period of melt water production the pO_2 is increased to 0.5 atm. A pCO_2 value for water in equilibrium with present-day atmospheric CO_2 (pCO_2 of $10^{-3.5}$ atm) is assigned for both the interglacial period and the period of glacial melt water production. The melt water simulated in the base case has a pH similar to that of rainwater (pH = 5.8) for both periods.

During the interglacial period, a concentration of DOC of 7.14×10^{-5} mol L^{-1} (2.14 mg L^{-1}) is assumed in the recharge water, while DOC is assumed absent from the recharge water during the period of melt water production (see Appendix A.6). The changing transport boundary conditions for pO_2 and DOC are presented graphically in Figure 3-3.
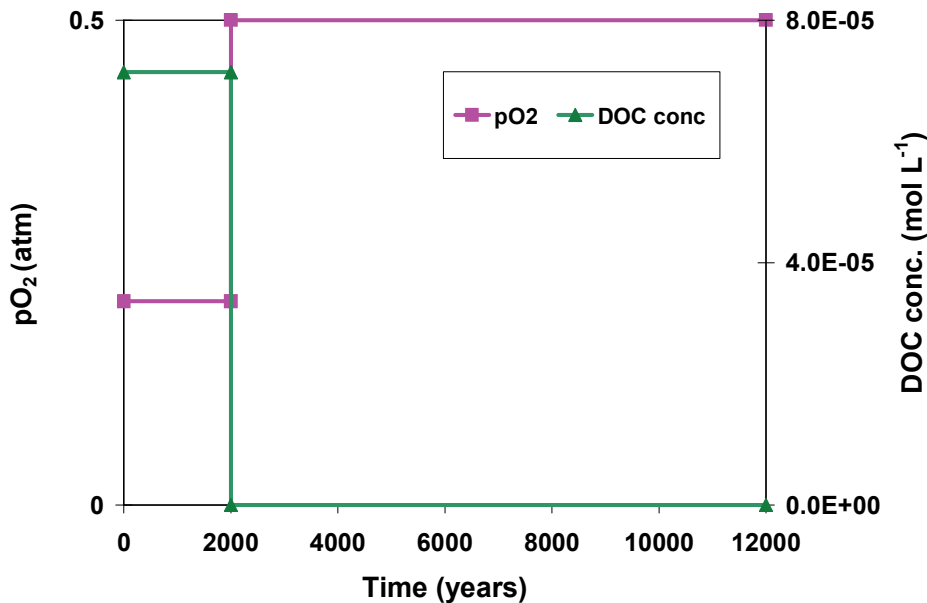
Figure 3-3: Transport boundary conditions for pO_2 and DOC during interglacial and glacial periods.

3.1.4. Discretization

Figure 3-4 illustrates the discretization of the model domain. The fracture is represented by a single column of grid cells in the vertical direction. The matrix is subdivided into three zones; a 0.5 m wide zone adjacent to the fracture is discretized into 25 columns, a second zone of 1 m width is discretized into 20 columns, and a third zone of 1.5 m thickness is discretized into 5 columns. Discretization in the vertical direction consists of a 5 m zone near the surface, which is discretized into 10 rows to accurately model degradation of DOC, while the remainder of the oxidized zone is discretized more coarsely. Preliminary simulations indicated that most redox buffering reactions occur in the upper part of the reducing zone; therefore a higher spatial resolution of 1 m is used from 100 m to 150 m. The remainder of the domain down to 500 m is again more coarsely discretized. The discretization presented in Figure 3-4 results in 7344 control volumes.
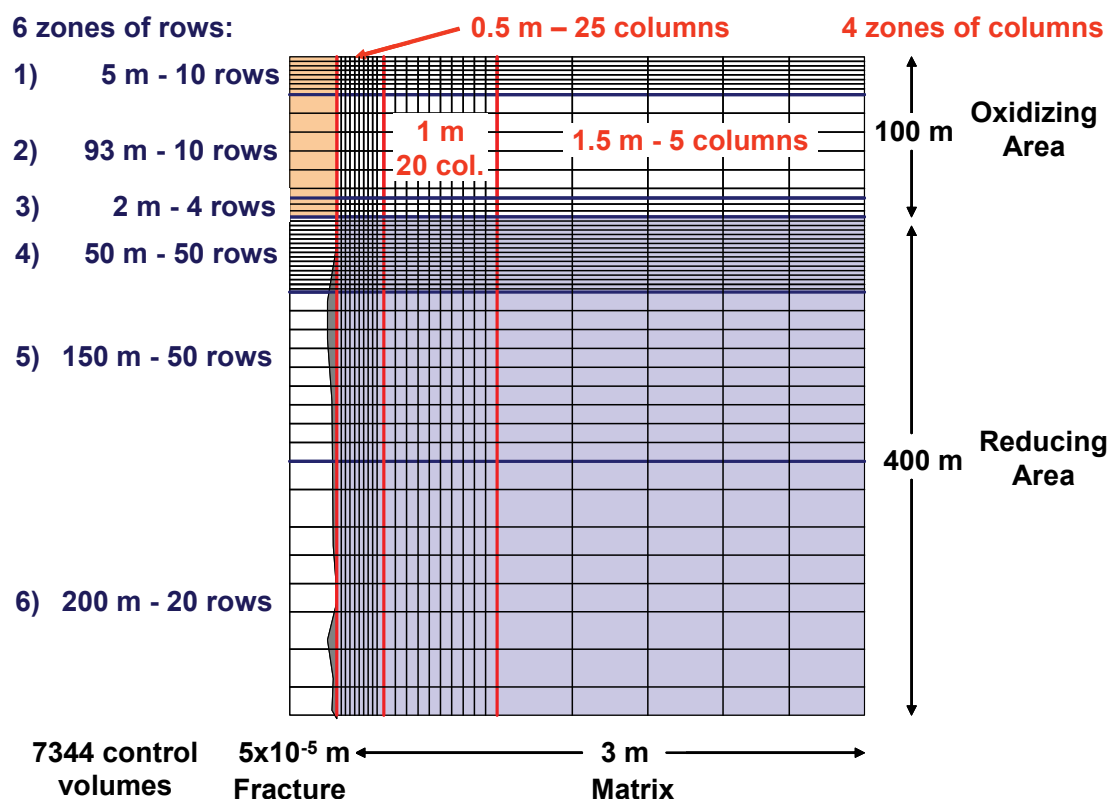
Figure 3-4: Illustration of the discretization of the base case domain (not to scale).

3.2. RESULTS AND DISCUSSION

In this section, the key results of the single fracture base case are presented and discussed. Additional results from the base case can be found in Appendix C, while the results of an investigation into grid discretization effects are presented in Appendix D.

Dissolved oxygen migrates to maximum depths of approximately 102 m and 112 m by the end of the interglacial and melt water production periods, respectively (Figure 3-5). Because the reducing zone was specified to begin at 100 m, this indicates that dissolved O_2 only advances approximately 2 and 12 m into the reducing zone during these two periods. Moreover, Figure 3-5 shows that after about 1,000 years during the interglacial period, and 8,000 years during the melt water period, a quasi-steady state distribution of O_2 is obtained (e.g.: the quasi steady state rate of O_2 advancement is approximately 0.05 mm/yr between 10,000 and 12,000 years). This condition is sustained by diffusive O_2-loss to the matrix balanced by O_2 consumption through oxidative biotite dissolution. After a simulation time of 12,000 years, dissolved O_2 has migrated a maximum distance of about 20 cm into the rock matrix adjacent to the fracture and a wedge-shaped oxidation profile has developed (Figure 3-6). During the interglacial period, approximately 27% of the dissolved oxygen influx is consumed by DOC degradation, while the remaining O_2 flux is consumed by rock-water interaction. DOC is predicted to be degraded aerobically within about 0.5 m depth (Figure 3-7). During the period of melt water production, it

is assumed that no DOC exists in the recharge water and therefore it plays no role in oxygen consumption after 2,000 years.

Chlorite in the fracture (Figure 3-8) and biotite in the matrix column adjacent to the fracture wall (Figure 3-9 and Figure C. 1) both experience dissolution to depths of approximately of 102 m after 2,000 years, and 112 m after 12,000 years. Chlorite is only completely dissolved in the upper metre of the fracture, while only about 4% of the biotite present in the matrix directly adjacent to the fracture is depleted after 12,000 years. Consistent with the dissolution of chlorite and biotite is the precipitation of goethite in the matrix to a depth of approximately 113 m (volume fraction of up to 0.025, Figure 3-11 and Figure C. 3).

Pyrite in the rock matrix also dissolves to depths of approximately 102 m after 2,000 years, and a depth of 113 m after 12,000 years (Figure 3-10 and Figure C. 2). Because of the relatively small initial mineral fraction of pyrite, and its fast reaction rate, pyrite is completely dissolved in the matrix region that contains oxygen.

The penetration of oxygen correlates well with mineral alteration in the rock matrix adjacent to the fracture. The simulations suggest the development of wedge-shaped alteration zones in the matrix adjacent to the fracture wall for biotite and pyrite (e.g. Figure 3-9 and Figure 3-10) which corresponds to the zone of oxygen migration into the matrix. This finding is generally consistent with the findings of Steefel and Lichtner (1998a), who also showed that wedge-shaped alteration zones should develop during reactive transport in discrete fracture-matrix systems. To date, no field observations exist for alteration thicknesses adjacent to fractures in Canadian Shield bedrock that could be used for constraining these model results. This is in part due to the difficulty of identifying a flow system along a single fracture and limited access to representative rock samples.

Additional results for pH, pCO_2, $Al(OH)_3(am)$, $SiO_2(am)$, gypsum and quartz are presented and discussed in Appendix C.

Domain size and discretization: The base case scenario assumes that the initially oxidized zone in the fracture and matrix extends to a depth of 100 m, and that the matrix width adjacent to the fracture is 3 m. The presence of the no flow boundary at a distance of 3 m from the fracture effectively translates to a fracture spacing of 6 m for sets of parallel fractures with equal fracture spacing and recharge rates. Because the influent boundary condition for dissolved O_2 increases at a simulation time of 2,000 years, the resulting concentration gradients created between the fracture and the matrix will result in O_2 diffusion from the fracture into the matrix in the oxidized zone. The implication of this is that a simulation domain with a different matrix width may yield different results if O_2 diffusion reaches the horizontal model boundary in the oxidized zone. To evaluate the effect of the choice of the simulation domain (i.e. fracture spacing), the results for the 3 m-wide matrix (6 m fracture spacing) are compared to the results of a simulation with a 50 m-wide matrix (100 m fracture spacing, all other parameters unaltered, see Appendix D). For a domain width of 50 m, vertical migration of oxygen into the reducing zone is approximately 9 m, compared to 12 m, and the mass of redox-buffering minerals that is dissolved is changed slightly from the 3 m-wide base case. The differences are therefore not of major consequence to the results of the base case, and the narrow fracture spacing used in the base case represents a conservative approach.
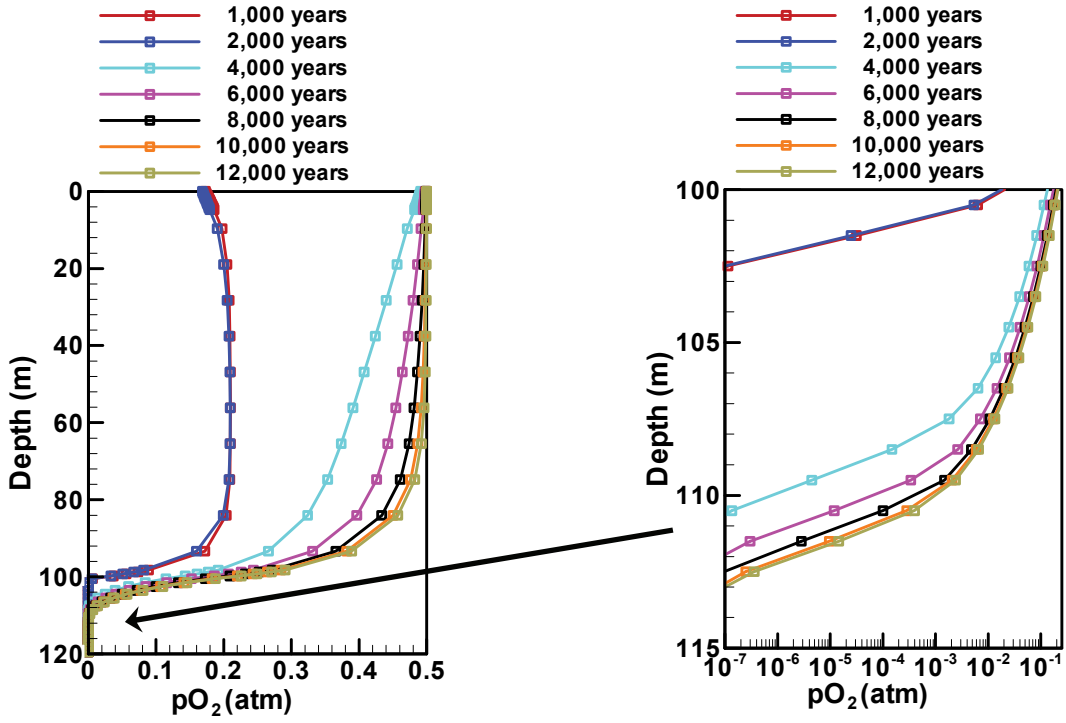
Figure 3-5: pO$_2$ distribution in the fracture with time and depth.
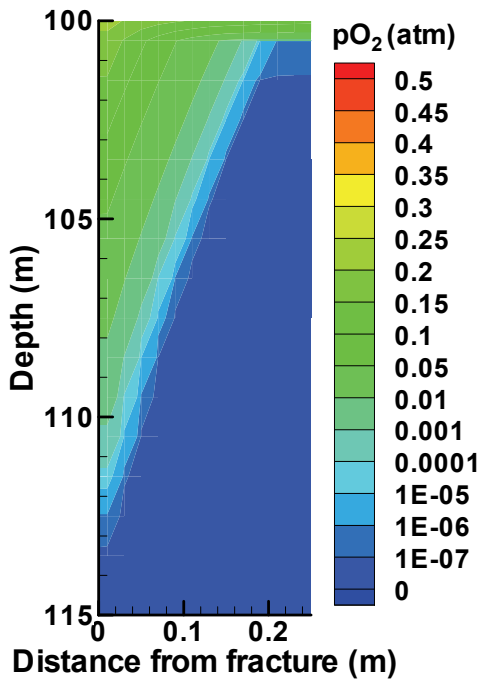
Figure 3-6: pO$_2$ distribution at 12,000 years.
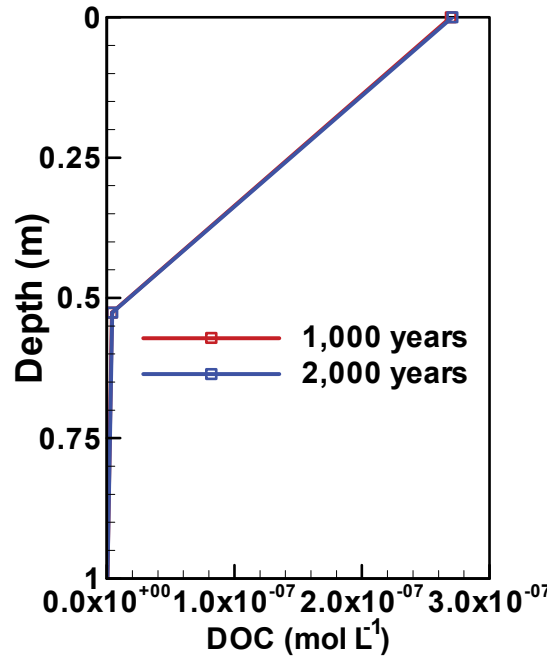
Figure 3-7: DOC distribution in the fracture with time and depth.
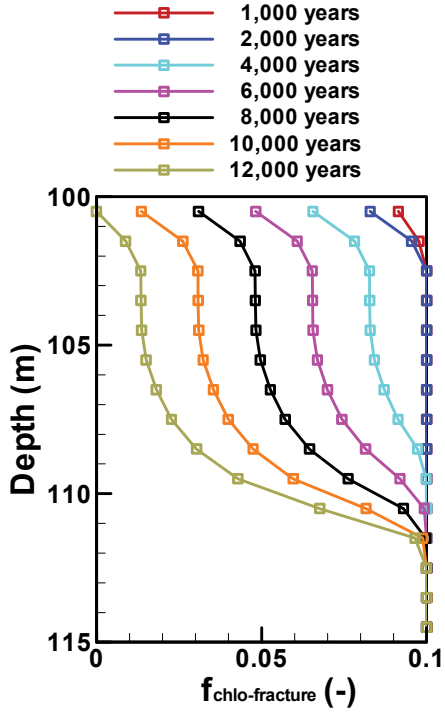
Figure 3-8: Chlorite distribution in the fracture with time and depth.
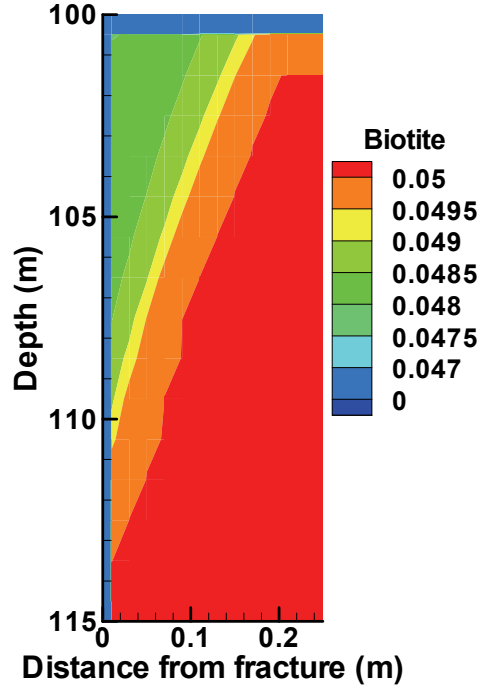
Figure 3-9: Biotite distribution at 12,000 years.
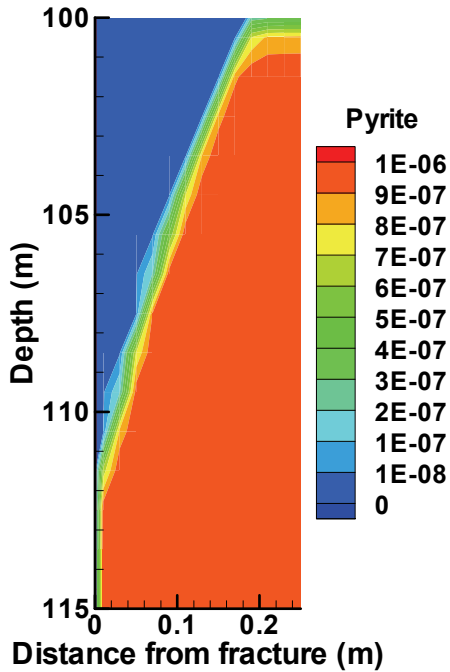
Figure 3-10: Pyrite distribution at 12,000 years.
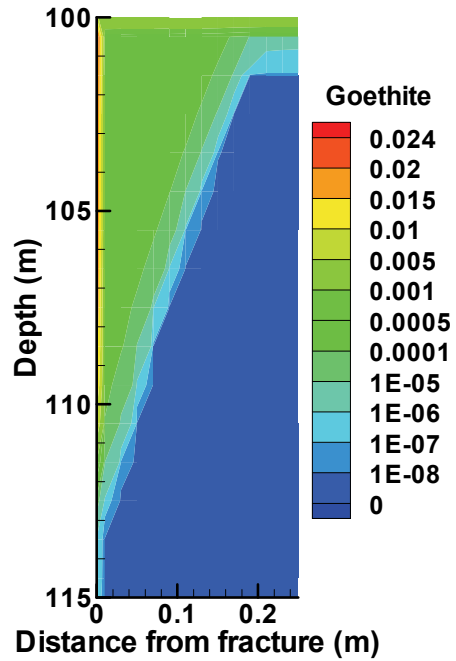
Figure 3-11: Goethite distribution at 12,000 years.

Appendix D also contains results from simulations with various alternative spatial discretizations of the base case domain. It is shown that adequate discretization of the matrix adjacent to the fracture is required to obtain consistent results, and that increasing the grid discretization relative to the base case has only a minor impact on the simulated depth of oxygen migration.

3.3. COMPARISON WITH FINDINGS OF GLYNN ET AL. (1997)

Results from previous calculations have suggested dissolved O_2 penetration to depths of greater than 500 m in fractures within granitic bedrock as a result of penetration of glacial meltwaters (Glynn et al. 1997). However, the matrix-skin-reaction model of Glynn et al. (1997) deals with O_2 transport in a simplified manner because it assumes that a) dissolved oxygen is initially present throughout the 500 m deep fracture-matrix-skin domain, and b) any O_2 consumed by biotite dissolution in the matrix is instantaneously replaced. Consequently, the main differences between the approach of Glynn et al. (1997) and that used here are that in the present model O_2 is initially absent from the domain, O_2-containing recharge water enters the fracture matrix system through the fracture only, and O_2 can only enter into the rock matrix by diffusive transport from the fracture. If matrix diffusion does dominate the transfer of dissolved O_2 to regions containing reduced minerals, which will likely be the case for open fractures in relatively unaltered rock, then the present mechanistic model should more closely represent the key processes during recharge of O_2-bearing glacial waters in fractured crystalline rock.

We have simulated a scenario similar to that of Glynn et al. (1997) by using the Stage I model and modifying selected parameters to more closely match the parameters used by Glynn et al. (1997). The half fracture width used is 1×10^{-4} m (symmetry is assumed) while the matrix width and porosity are 0.1 m and 0.01, respectively. The reactive-transport parameters used are: a fracture velocity of 2.48×10^{-7} m s^{-1} which corresponds to an advection rate of 500 m in 64 years, a D_a of 1.1×10^{-10} m^2 s^{-1} which is equal to the base case value, an influent dissolved O_2 concentration of 1.2×10^{-3} mol L^{-1} (1 atm), and a biotite reaction rate of 1.27×10^{-14} mol L^{-1} bulk s^{-1}, which is equivalent to the rate estimated by Glynn et al. (1997) based on work by Malmström and Banwart (1997). Biotite is assumed to be present only in the matrix with an initial volume fraction of 0.1.

Using the above parameters, dissolved O_2 within the fracture attains a quasi-steady distribution after about 1,000 years, and the simulated O_2 migration depth after 10,000 years (for a concentration of 10^{-5} atm) is approximately 100 m (Figure 3-12). Figure 3-13 shows that the O_2 migration depth is clearly controlled by biotite consumption; however, biotite is never depleted in any regions of the domain. On the other hand, Glynn at al. (1997) predicted oxygen breakthough at 500 m depth in less than 64 years. This significant discrepancy in interpretation despite a nearly identical parameter set can be attributed to differences between the conceptual models and initial conditions.

A further investigation of the Glynn et al. (1997) scenario has been made by performing simulations in which several key parameters are sequentially varied from the values discussed above to those used in the Stage I base case (Section 3). For example, case 2 in Table 3-6 is similar to the Glynn et al. (1997) scenario with the exception that the matrix width is increased to 3 m (see Table 3-1). The results for this case show the influence of increased matrix diffusion into the wider rock matrix. For case 3, the oxygen concentration has been reduced from that used in the original Glynn et al. (1997) scenario, which results in a further decrease in the O_2 migration depth. Table 3-6 shows that for all of the additional cases considered, O_2 does

not migrate to depths of greater than 100 m, a significantly shallower depth than suggested by the calculations of Glynn et al. (1997).
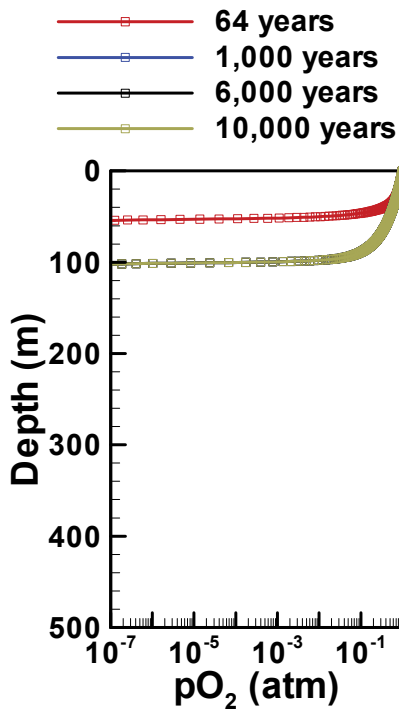
Figure 3-12: pO$_2$ distribution in the fracture with time and depth (model parameters similar to Glynn et al. 1997).
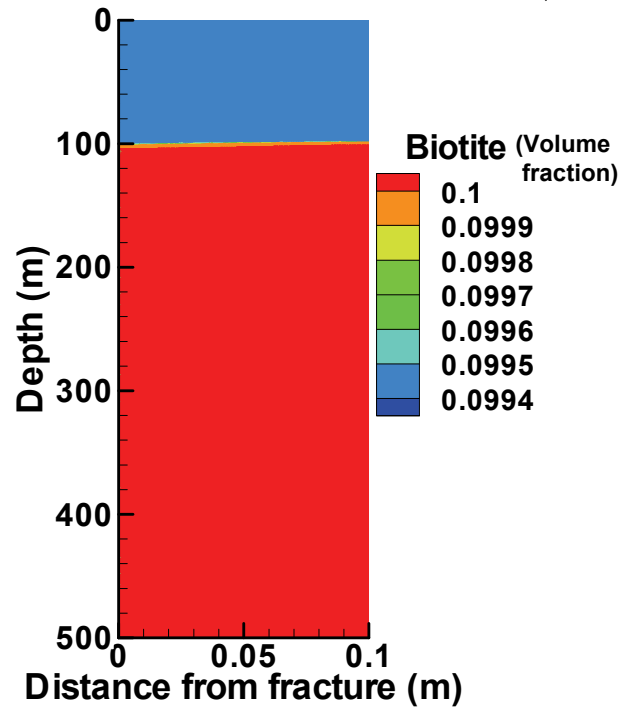
Figure 3-13: Biotite distribution after 10,000 years (model parameters similar to Glynn et al. 1997).

Table 3-6: Dissolved O$_2$ migration depths for scenario of Glynn et al. (1997) and for selected parameter variations. Depths are for a pO$_2$ concentration 10^{-5} atm.

Case	Description	O$_2$ migration depth (m)
1	Model parameters similar to Glynn et al. (1997) - D$_a$ from base case	100
2	As 1) but matrix width increased to the base case value of 3 m	23
3	As 2) but O$_2$ concentration in the recharge water is reduced to the base case value (0.5 atm, period of glacial melt water production)	14.8
4	As 3) but k$_{bio-matrix}$ (1.27×10^{-14} mol m^{-2} s^{-1}) is increased to the base case value (3.71×10^{-14} mol m^{-2} s^{-1})	8.7
5	As 4) but q$_f$ (7.8 m yr^{-1}) is increased to base case value (10 m yr^{-1}, glacial period)	11.1

4. STAGE II: SINGLE FRACTURE SCENARIO PARAMETER UNCERTAINTY

The review of model parameters presented in Appendix A shows that there is considerable uncertainty in choosing some of the parameter values required for reactive transport simulations. Uncertainty analysis can reveal which parameters most influence the model predictions and this information can also be used to better focus characterization of fractures and matrix rock during site selection and investigation. Uncertainty analysis methods can include:

  i) Monte Carlo,
  ii) sensitivity analysis, and
  iii) factorial analysis or design.

Monte Carlo analysis requires the definition of a probability density function (pdf) for all key parameters to be studied; however, such distributions are not available for key reactive transport parameters at the present time. Sensitivity analysis is more simplistic and less computationally demanding than Monte Carlo analysis, but may fail to capture the interrelationship between input parameters (Zheng and Bennett 2002). As an alternative to these two approaches, in Stage II we use a method based on factorial design of experiments which does not have the demands of Monte Carlo analysis, but yet allows for a systematic evaluation of the interplay between parameters and facilitates the identification of the parameters that most significantly affect system evolution.

Devore and Farnum (1999) provide an introduction to factorial design of experiments and the graphical methods, including effects plots and probability plots, that can be used for visually summarizing results and for determining the parameters (i.e. factors) that are most influential. Specifically, a two-level factorial analysis (denoted as 2^k, where k is the number of factors) is conducted which requires two values to be selected, a minimum and maximum, for all parameters considered in the analysis. The approach assumes that the factors are independent. Two sets of analyses are conducted; each having a different range between the minimum and maximum values. The first set of simulations focuses on the identification of the most important parameters, while the second set of simulations is performed to determine whether the selected parameter ranges influence which parameters are deemed to be the most important. An additional objective of the second set of simulations is to assess the influence of parameter uncertainty on the model results.

4.1. DESCRIPTION OF PARAMETER RANGES FOR THE UNCERTAINTY ANALYSIS

The single fracture-matrix scenario defined in the Stage I base case is used to determine the parameters of most importance. The analysis is conducted with respect to the following parameters:

1. apparent diffusion coefficient (D_a) of the rock matrix
2. matrix porosity (φ_m)
3. Darcy velocity in fracture (q_f) during the period of melt water production
4. fracture half aperture (δ)
5. pO_2 of the influent recharge melt water
6. chlorite abundance in the fracture ($f_{chlo\text{-}fracture}$)

7. biotite abundance in the matrix ($f_{bio-matrix}$)
8. pyrite abundance in the matrix ($f_{pyr-matrix}$)
9. chlorite reaction rate ($k_{chlo-fracture}$), and
10. biotite reaction rate ($k_{bio-matrix}$).

These parameters were selected based on the insight gained in the Stage I modelling. With 10 parameters, or factors, a 2^k factorial analysis requires 1024 parameter combinations (i.e. model simulations). To save computational time, the number of reactions considered is reduced to only include interactions between O_2, DOC, biotite, chlorite and pyrite. This reduction in the number of components and mineral phases does not affect the depth of migration of oxygenated water in the fracture and matrix to any significant degree because the omitted minerals and dissolved species have no effect on oxygen consumption. This was verified by conducting the base case simulation for the simplified reaction system.

Mineral volume fractions and reaction rates are only varied for the reduced zone below a depth of 100 m (see Figure 3-2). As was assumed for the base case, the volume fraction of chlorite in the matrix ($f_{chlo-matrix}$) and the volume fraction of biotite and pyrite in the fracture are assumed to be zero for all cases. The reaction rate constant for pyrite is not adjusted as its value is relatively large. Instead, the initial volume fraction of pyrite is varied which is considered more relevant for the problem being investigated.

Table 4-1: Minimum and maximum parameter values used for uncertainty analysis 1. The base case scenario values are shown for comparison.

Parameter	Case		
	Minimum	Base	Maximum
D_{eff} (m^2 s^{-1})	2.7×10^{-13}	5.4×10^{-13}	1.08×10^{-12}
D_a (m^2 s^{-1})	5.5×10^{-11}	1.1×10^{-10}	2.16×10^{-10}
φ_m	2.5×10^{-3}	5×10^{-3}	1×10^{-2}
q_f (m yr^{-1}) – glacial period	5	10	20
δ (m)	2.5×10^{-5}	5×10^{-5}	1×10^{-4}
pO_2 (atm) - glacial period	0.25	0.5	1.0
$f_{chlo-fracture}$	5×10^{-2}	1×10^{-1}	2×10^{-1}
$f_{bio-matrix}$	2.5×10^{-2}	5×10^{-2}	1×10^{-1}
$f_{pyr-matrix}$	5×10^{-7}	1×10^{-6}	2×10^{-6}
$k_{chlo-fracture}$ (mol chlo) /(L$_{water}$ sec)	5.5×10^{-13}	1.1×10^{-12}	2.2×10^{-12}
$k_{bio-matrix}$ normalised with respect to $f_{bio-matrix}$ (mol bio) /(L$_{bulk}$ sec)	1.85×10^{-14}	3.7×10^{-14}	7.4×10^{-14}

Analysis 1: For the first uncertainty analysis, the parameter values used in the base case were decreased and increased by a factor two to define the minimum and maximum parameter values, respectively. The complete set of parameters as well as D_{eff}, which is used to calculate D_a, are given in Table 4-1.

Analysis 2: Table 4-2 lists the minimum and maximum values employed for the second 2^k factorial analysis. In this analysis the maximum and minimum values are based, when possible, more closely on ranges reported in the literature. For example, based on the literature reviewed in Appendix A, D_{eff}, φ_m and $f_{bio-matrix}$ are considered to be reasonably well determined

and the ranges chosen are considered representative. Other parameters; however, have limited data and in most of these cases (e.g. q_f, δ, $k_{chlo-fracture}$, $k_{bio-matrix}$), order-of-magnitude changes from the base case value are used. For influent pO_2 concentration during the 10,000 year-period of glacial melt water production, the minimum is set to the present-day atmospheric concentration while the maximum is approximately five times the present-day value. Considering the projections of O_2 in glacial melt water reviewed in Appendix A, this range is appropriate; however, it must be noted that these projections remain unverified with field data. For pyrite and chlorite, the minimum values for initial volume fractions are selected to be zero.

Table 4-2: Minimum and maximum parameter values used for uncertainty analysis 2. The base case scenario values are shown for comparison.

Parameter	Case		
	Minimum	Base	Maximum
D_{eff} (m^2 s^{-1})	7.1×10^{-14}	5.4×10^{-13}	1.9×10^{-12}
D_a (m^2 s^{-1})	1.4×10^{-11}	1.1×10^{-10}	3.8×10^{-10}
φ_m	2×10^{-3}	5×10^{-3}	9.5×10^{-3}
q_f (m yr^{-1}) – glacial period	1	10	100
δ (m)	5×10^{-6}	5×10^{-5}	5×10^{-4}
pO_2 (atm) – glacial period	0.21	0.5	1.0
$f_{chlo-fracture}$	0	1×10^{-1}	3×10^{-1}
$f_{bio-matrix}$	2×10^{-2}	5×10^{-2}	1.3×10^{-1}
$f_{pyr-matrix}$	0	10^{-6}	10^{-5}
$k_{chlo-fracture}$ (mol chlo) (L$_{water}$ s)$^{-1}$	1.1×10^{-13}	1.1×10^{-12}	1.1×10^{-11}
$k_{bio-matrix}$ normalised with respect to $f_{bio-matrix}$ (mol bio) (L$_{bulk}$ s)$^{-1}$	3.7×10^{-15}	3.7×10^{-14}	3.7×10^{-13}

4.2. MODEL RESPONSE

To quantify the relative importance of the input parameters, it is necessary to select a suitable model response (result). The depth of dissolved oxygen migration in the fracture at a time of 12,000 years is chosen as the response because oxygen is a key indicator of redox conditions (e.g. Glynn et al. 1997) and, as we have demonstrated in Stage I, the penetration of oxygen correlates well with mineral alteration in the rock matrix adjacent to the fracture.

In defining the depth of O_2 migration a concentration criterion of 10^{-5} atm (~ 5×10^{-4} mg L^{-1}) is used. The basis for selecting this value is discussed in more detail in Appendix E. In addition, comparison of the depth of O_2 migration using concentrations as low as 10^{-8} atm shows that the O_2 penetration depth distribution does not vary significantly from that obtained when the pO_2 concentration criterion is 10^{-5} atm (Appendix E).

For simulations in which the dissolved O_2 concentration was above 10^{-5} atm at the lower limit of the domain, migration depths are extrapolated using:

$$\left(pO_2 \text{ penetration depth}\right)_{\text{extrapolated}} =$$

$$500 - \frac{500}{[pO_2]_{500\,m} - [pO_2]_{\text{recharge}}} * \left([pO_2]_{500\,m} - [10^{-5}\ atm]\right) \tag{16}$$

where $[pO_2]_{\text{recharge}}$ refers to the influent pO_2 boundary concentration, and $[pO_2]_{500\,m}$ is the pO_2 concentration at 500 m in the fracture after 12,000 years.

4.3.   RESULTS AND DISCUSSION

4.3.1.   Identification of important parameters

One of the recommended procedures for identifying the main factors influencing a response is to compute the main effects (i.e. those resulting from individual parameters) and the interaction effects resulting from combinations of parameters. The effects are then presented in a normal probability plot and a straight line is fit to the data; the effects that fall farthest from the straight line are the most important (Devore and Farnum 1999). Appendix F.1 describes how the effects were calculated in this study and how representative probability plots were constructed from the computed effects. As skewed distributions could be identified in the computed effects, transformation of the response values was also required. Details for the determination of appropriate transformations for the two factorial analyses are outlined in Appendix F.2.

Results from Analysis 1. The probability plot shown in Figure 4-1 indicates that the Darcy velocity in the fracture (q_f), fracture half aperture (δ), and reaction rate of biotite in the rock matrix ($k_{\text{bio-matrix}}$) are the most important parameters because the effects for these parameters lie the furthest from the straight line that represents no effect. The analysis in Appendix F.3 indicates that D_a, matrix porosity (φ_m), and pO_2 are also important, but to a lesser extent than q_f, δ and $k_{\text{bio-matrix}}$. The interactions between q_f and δ, q_f and $k_{\text{bio-matrix}}$, q_f and pO_2, and pO_2 and δ, are also found to be less significant, and it should be noted that all these parameter interactions contain q_f or δ. Better constraining q_f, δ and $k_{\text{bio-matrix}}$ would therefore provide the most benefit with respect to reducing uncertainty in future simulations.

Results from Analysis 2. The probability plot (Figure 4-2) for analysis 2 reveals that, consistent with analysis 1, the most important factors within the set of parameters investigated are the fracture velocity (q_f), the fracture half aperture (δ), and reaction rate of biotite in the rock matrix ($k_{\text{bio-matrix}}$). The apparent diffusion coefficient in the rock matrix (D_a) is shown to be less important. It appears that having a larger range for q_f, δ, and $k_{\text{bio-matrix}}$ in this analysis has resulted in a decrease in the importance of φ_m and pO_2.
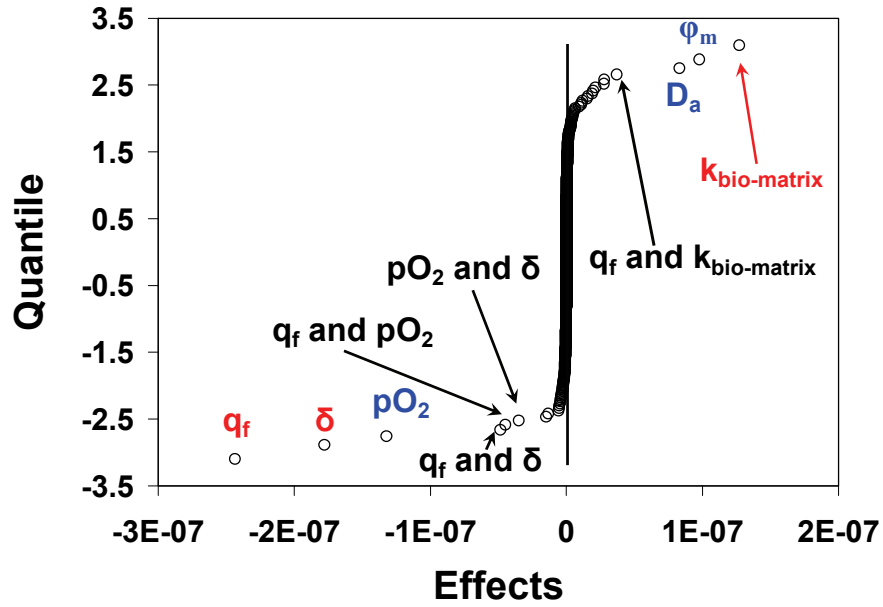
Figure 4-1: Probability plot of the effects for analysis 1 (see Table 4-1 for parameter ranges).
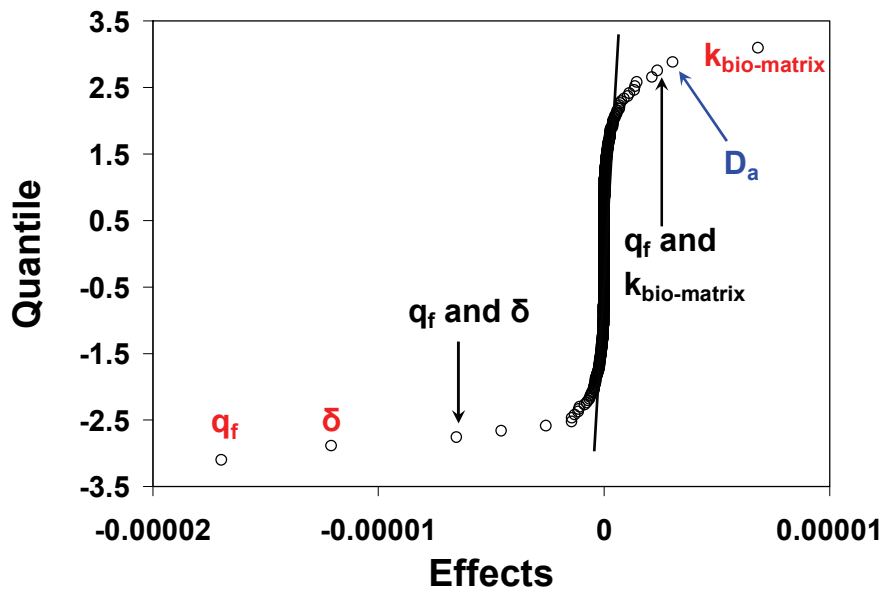
Figure 4-2: Probability plot of the effects for analysis 2 (see Table 4-2 for parameter ranges).

4.3.2. Statistics of oxygen penetration depth

Table 4-3 shows that the geometric means of the O_2 penetration depth distributions obtained from analyses 1 and 2 are very similar (ranging from 116.5 to 175.0 m). Larger variations can be noticed in the arithmetic mean values (range of 117.8 to 380.0 m) and the standard deviations because of the influence that a few high values have on these statistics.

Table 4-3: Geometric mean, arithmetic mean, and standard deviation of O_2 penetration depth (in m) for the data sets from analysis 1 and 2.

	Data set for analysis 1		Data set for analysis 2	
	2^{10} design	a) 2^6 design	2^{10} design	2^{10} design including extrapolated values
Geometric Mean	116.7	116.5	153.1	175.0
Arithmetic Mean	117.8	117.6	186.3	380.0
Standard deviation	18.2	17.9	138.4	919.6

a) an additional set of simulations was conducted that focused on the 6 most important parameters identified by the 2^{10} design.

5. STAGE III: SINGLE FRACTURE DUAL CONTINUUM MODEL

This stage of the study compares the results from a dual continuum model (DCM) to the discrete fracture model (DFM). As mentioned in Section 2.2, for a DCM the fracture and matrix are treated as two separate, but interacting continua: a mobile (fracture) region, and an immobile (matrix) region. They co-exist as illustrated in Figure 5-1. In contrast to the DFM, the DCM assumes that the mobile and immobile regions have the same domain size.
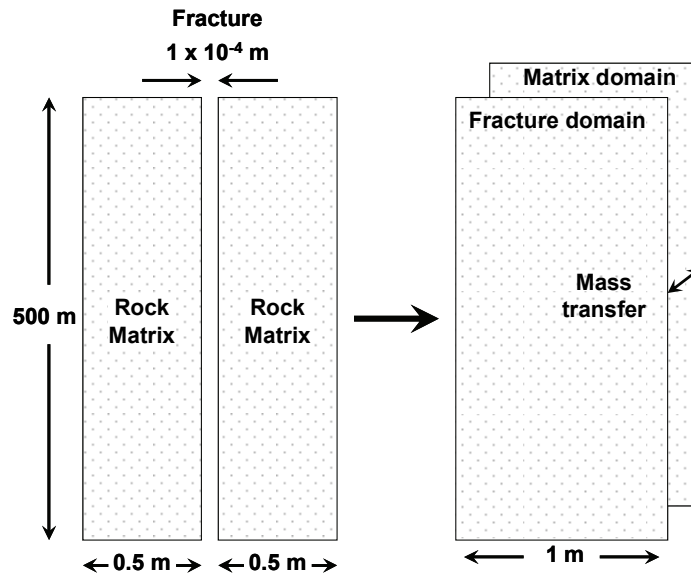
Figure 5-1: Schematic representation of a single fracture DFM (left) and DCM (right).

In MIN3P, a one-dimensional DFM simulation is performed by taking a 1 m-wide matrix block containing an open fracture with an aperture of 1×10^{-4} m. To parameterize the DCM, the mobile and immobile regions both need to have a width of 1 m and this requires scaling of all parameters that are affected by the fracture aperture, including fracture porosity, velocity, mineral volume fractions, and reaction rates. Scaling of the parameters is described in Appendix G, and the values of the scaled parameters are compared to those of the DFM in Table 5-1. Boundary conditions, initial conditions, and other relevant parameters are consistent with the Stage I base case.

Table 5-1: Values of the scaled parameters of the DCM compared to the parameters of the DFM.

Parameter	DCM	DFM
Matrix porosity (φ_m)	4.9995×10^{-3}	5×10^{-3}
Fracture porosity (φ_f)	1×10^{-4}	1
Fracture Darcy velocity (q_f) during interglacial period (m yr^{-1})	1×10^{-4}	1
Fracture Darcy velocity (q_f) during period of glacial melt water production (m yr^{-1})	1×10^{-3}	10
Biotite volume fraction ($f_{bio-matrix}$)	4.9995×10^{-2}	5×10^{-2}
Pyrite volume fraction ($f_{pyr-matrix}$)	9.999×10^{-7}	1×10^{-6}
Chlorite volume fraction ($f_{chlo-fracture}$)	1×10^{-5}	1×10^{-1}
Biotite reaction rate ($k_{bio-matrix}$, mol L^{-1} bulk s^{-1})	3.71×10^{-14}	3.71×10^{-14}
Pyrite reaction rate ($k_{pyr-matrix}$, mol L^{-1} bulk s^{-1})	1×10^{-12}	1×10^{-12}
Chlorite reaction rate ($k_{chlo-fracture}$, mol L^{-1} bulk s^{-1})	1.12×10^{-16}	1.12×10^{-12}

5.1. RESULTS AND DISCUSSION

Figure 5-2 and Figure 5-3 compare the oxygen profiles obtained using the DFM and the DCM with a mass transfer coefficient of 1.8×10^{-11} s^{-1}. Although a relatively good agreement is achieved between the two model formulations for the O_2 profiles, it should be noted that the DCM model was calibrated to the DFM results by trial-and-error adjustment of the mass transfer coefficient. That is, it is not possible to *a priori* determine an appropriate mass transfer coefficient for the DCM simulation. For example, if the quasi-steady model of diffusive mass exchange presented by Lichtner (2000) is used with the current fracture and matrix parameters, a mass transfer coefficient of 2.2×10^{-12} s^{-1} is obtained. This is one order of magnitude smaller than the value we obtained by calibration of the DCM to the DFM results. The geometrically-based mass transfer coefficient relies on an assumption that the concentrations in the matrix continuum equilibrate instantaneously at a given location. This is clearly not the case, as diffusion and reactions in the matrix result in relatively steep concentration gradients in the first 0.1 to 0.2 m of the matrix. As pointed out by Lichtner (2000), as the matrix block size is increased, the computed geometric mass transfer coefficient decreases, which would reduce the fracture-matrix interaction. This behavior is counter-intuitive and would not be predicted by a DFM.

This comparison suggests limited applicability of the standard DCM approach in sparsely fractured rock because the mass transfer coefficient will depend on the particular scenario being simulated (i.e. fracture aperture, velocity, etc.). To demonstrate this problem, the Darcy velocity for the current simulation has been increased by a factor of ten and the simulation rerun using both the DFM and DCM. All other parameters, including the mass transfer coefficient, remain unchanged. For this situation, the DCM results are no longer in good agreement with the results obtained using the DFM (Figure 5-4 and Figure 5-5). It thus appears that the lack of resolution of gradients in the matrix, which is represented by a single control volume in the DCM, leads to poorly defined mass transfer coefficients. The mass transfer coefficient therefore cannot be determined without first conducting a DFM simulation or, by having a field data set available for model calibration (e.g. Shapiro 2001).

Table 5-2: Results of DCM and DFM for base case simulation (1 m domain width).

Model approach	O_2 advance into reducing zone (m)	Mass reacted (mol)		
		biotite	pyrite	chlorite
DFM	10	11.14	0.05	0.16
DCM	10	10.12	0.12	0.17
DFM - no pyrite	10	11.85		0.17
DCM - no pyrite	10	11.84		0.17
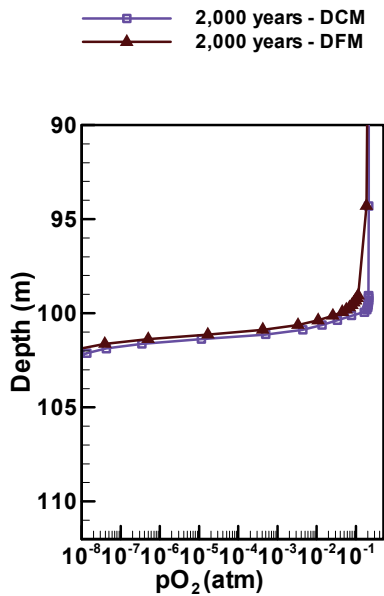
Figure 5-2: Dissolved oxygen profile at 2,000 years (end of interglacial period).
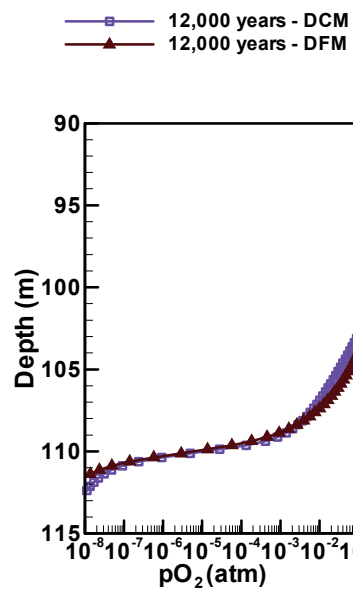
Figure 5-3: Dissolved oxygen profile at 12,000 years (end of melt water production period).
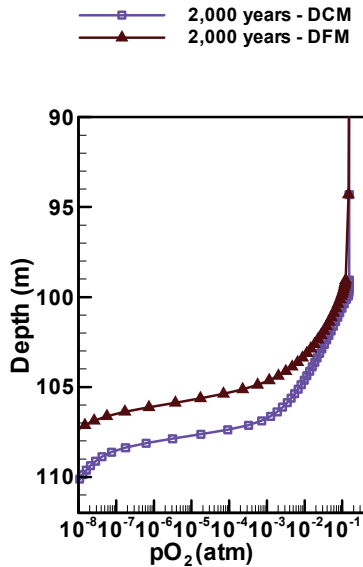
Figure 5-4: Dissolved oxygen profile at 2,000 years (end of interglacial period) for Darcy flux increased by one order of magnitude.
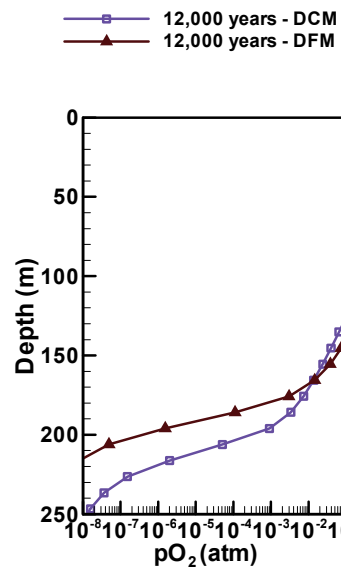
Figure 5-5: Dissolved oxygen profile at 12,000 years (end of melt water production period) for Darcy flux increased by one order of magnitude.

For the first set of simulations (i.e. Figure 5-2 and Figure 5-3) the mass of minerals reacted after 12,000 years is given in Table 5-2, where the largest differences are noted for the matrix minerals biotite and pyrite. A relatively large discrepancy occurs for pyrite because it is less abundant than biotite, but reacts more rapidly and becomes depleted in response to the ingress of oxygen. In the DFM, the depletion of pyrite is limited to the wedge shaped-alteration zone (Figure 3-9), but in the DCM pyrite depletion occurs throughout the matrix as long as O_2 is present in the adjacent fracture. Biotite does not become depleted in the matrix (Figure 3-8) and is therefore less sensitive to the lack of model resolution perpendicular to the fracture. For both modelling approaches, the simulations were repeated without pyrite and using a mass transfer coefficient of 1.8×10^{-11} s^{-1} for the DCM. In these simulations the mass of biotite reacted is almost identical for both models, which suggests that the DCM is better suited for simulations that include only a single redox buffering mineral phase with limited reactivity. However, the results of both DCM simulations show clearly that this method does not provide any information on the spatial extent of alteration in the matrix, which limits its use for comparison with field data. For the DCM, the simulation times were unexpectedly large, which is attributed to the relatively large mass transfer coefficient in comparison to the time scale of transport.

6. STAGE IV: SIMPLE FRACTURE NETWORKS

The single fracture scenarios used in Stages I through III provided an essential understanding of the basic processes controlling oxygen migration into fractured rock; however, networks of fractures will also exist in the Canadian Shield bedrock. In Stage IV, two-dimensional simulations are conducted to investigate the effect of spatial complexity on the movement of oxidizing groundwater for time scales on the order of thousands of years.

6.1. DESCRIPTION

Four arbitrary fracture network scenarios are investigated and these can be categorised as containing:

(i)   widely-spaced fractures (2 scenarios in total) and
(ii)   narrowly-spaced fractures (2 scenarios in total).

Spacing between the vertical fractures for the first pair of scenarios is approximately 3 m, while for the second pair it is approximately 0.2 m. A horizontal domain width of 100 m is chosen and all fractures are assigned an aperture of 1×10^{-4} m. Other than the increased domain width and the presence of multiple fractures, all other initial and boundary conditions are the same as used in the base case (Table 3-1, Table 3-2, Table 3-4, and Table 3-5). All simulations are conducted for a total simulation time of 12,000 years, which includes 10,000 years of glacial melt water production.
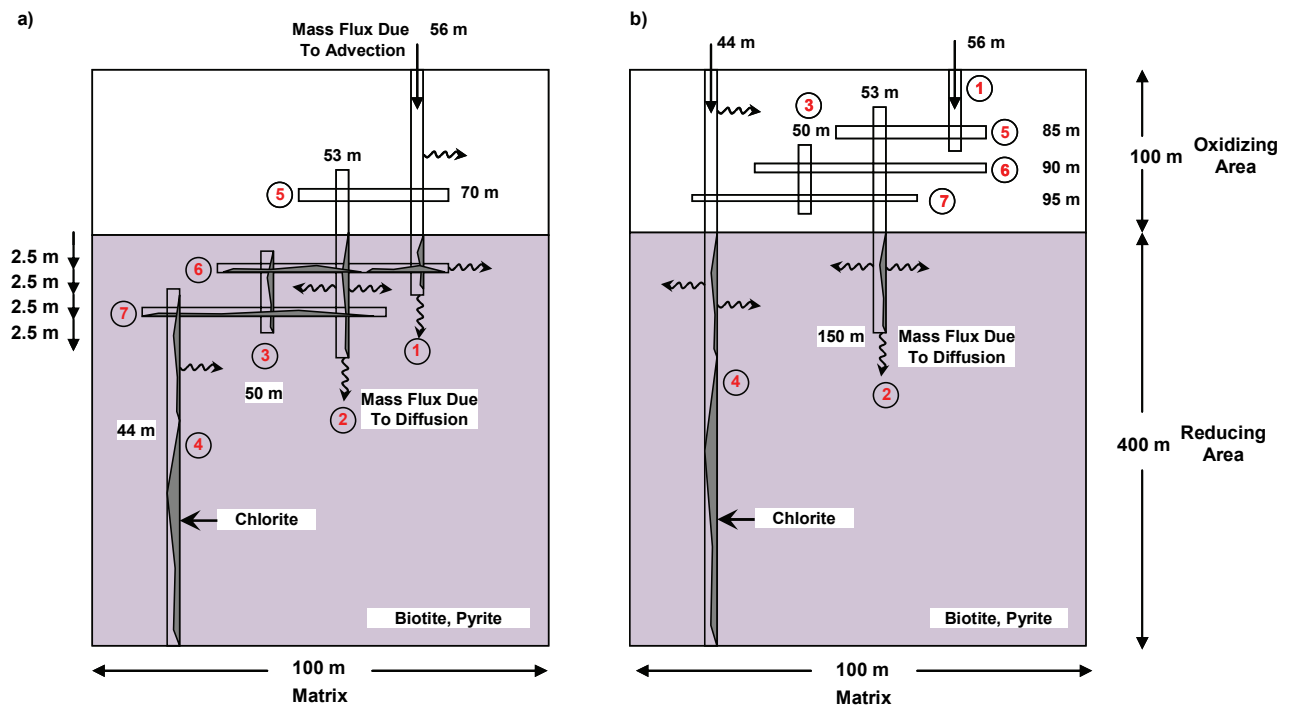
Figure 6-1: Configuration of fracture networks for a) Scenario 1, and b) Scenario 2.
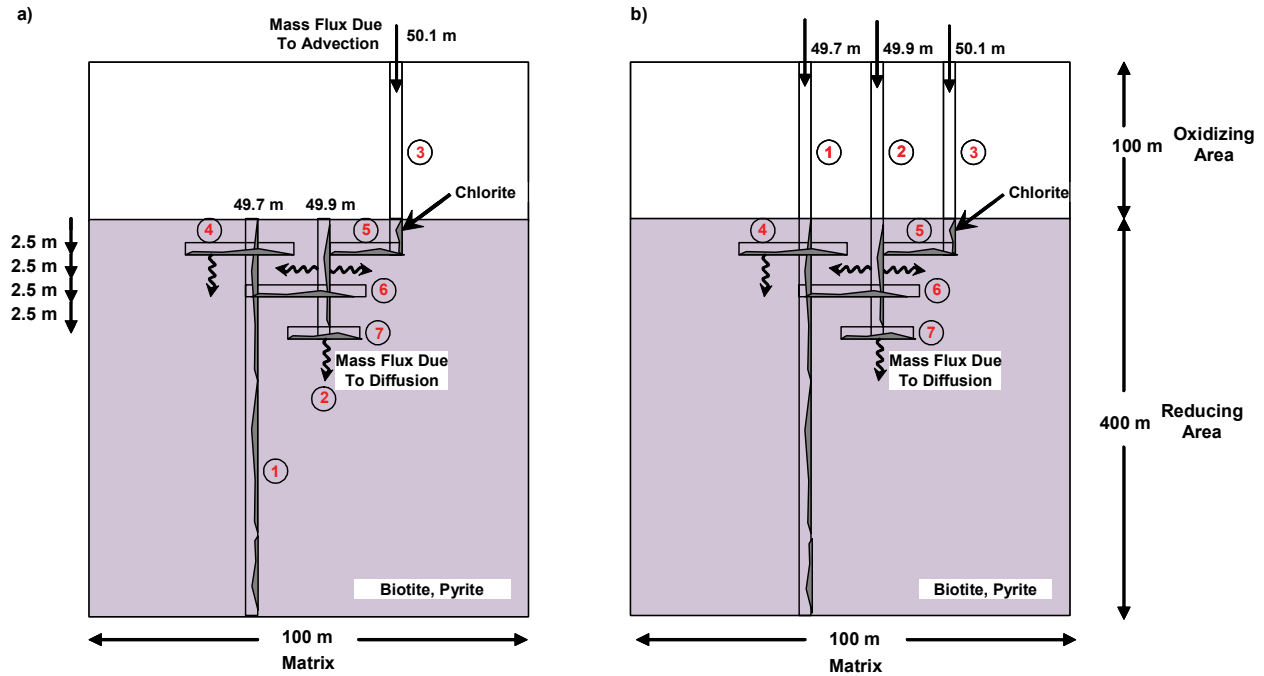
Figure 6-2: Configuration of fracture networks for a) Scenario 3, and b) Scenario 4.

Figure 6-1 shows the fracture arrangement for Scenarios 1 and 2. The main differences between these two scenarios is that Scenario 2 has more fractures located in the oxidizing zone (0 to 100 m), and one of the fractures (fracture 4) extends to the surface where it receives recharge. Thus the domain in Scenario 2 receives twice the water and dissolved oxygen influx as in Scenario 1.

The configuration of the networks for scenarios with narrowly-spaced fractures (Scenarios 3 and 4) is shown in Figure 6-2. The primary difference between these two is that Scenario 4 has three vertical fractures which extend to the surface and receive water influx. This effectively triples the total water flux into the domain when compared to Scenario 1 and 3.

6.2. RESULTS AND DISCUSSION

Because the reactive transport processes are the same as those considered in previous simulations, only illustrative results are presented for Scenarios 1 and 2. Figure 6-3 shows the pO_2 and biotite distributions for a subregion of the model domain at a time of 12,000 years for Scenario 1. In Scenario 1, the penetration of oxygen is restricted to the two vertical fractures (1 and 2) that traverse the oxidized and reducing zone. Oxygen consumption by mineral dissolution (e.g. biotite, Figure 6-3b) in and near these fractures and the connecting horizontal fracture (fracture 6) limit the oxygen migration depth to about 5 m into the reducing zone. No significant concentration of oxygen reaches the more deeply penetrating fracture 4 (refer to Figure 6-1a for fracture network).
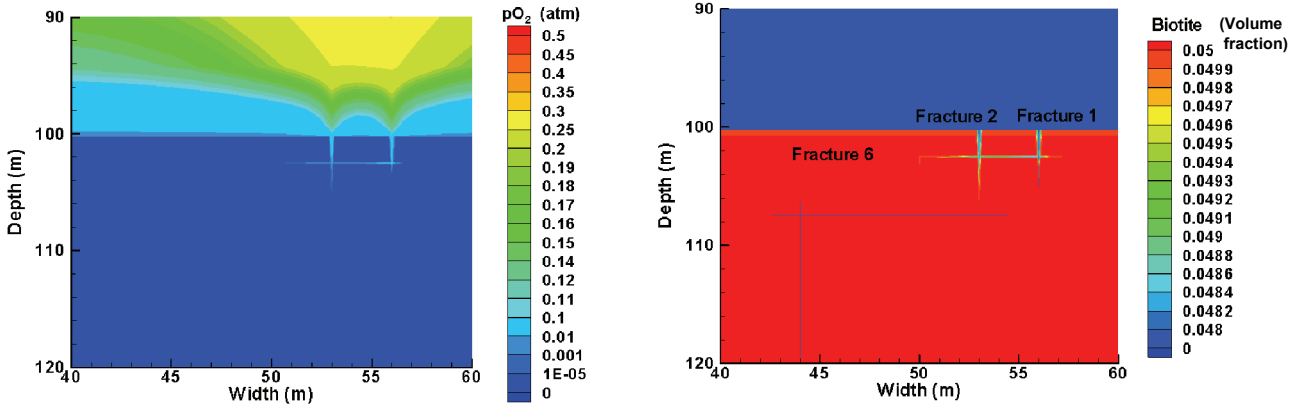
Figure 6-3: Results for Scenario 1 at a time of 12,000 years. a) pO_2 distribution, b) biotite distribution. Only a subregion of the model domain is shown.

In contrast to Scenario 1, the results for Scenario 2 (Figure 6-4) show dissolved O_2 migration to a depth of approximately 18 m into the reducing zone. This deeper migration is caused by the increased influx of water and dissolved oxygen and the particular fracture configuration considered. Fracture 4 effectively receives twice the recharge as in Scenario 1 because it is connected to fractures that truncate at relatively shallow depths.

Table 6-1 compares the maximum migration depth of dissolved O_2 for the four fracture network scenarios and the single fracture base case with a 50 m wide domain (as presented in Appendix D). In all cases, the maximum O_2 migration depth corresponds to the location of a vertical fracture. It can be seen from these results that the presence of a fracture network can either increase, or decrease, the migration depth relative to that of the single fracture base case. When a single fracture receives recharge water that subsequently flows through horizontal fractures that exist in a reducing environment (i.e. Scenarios 1 and 3) then this enhances the opportunity for oxygen depletion. If on the other hand, because of fracture truncation, a vertical fracture receives the recharge water from multiple fractures (Scenarios 2 and 4) then the depth of dissolved O_2 migration will be increased relative to a single fracture. In summary, O_2 advance in a fracture network depends upon the configuration of the fractures and the transport distance within the fracture network in the reducing zone.
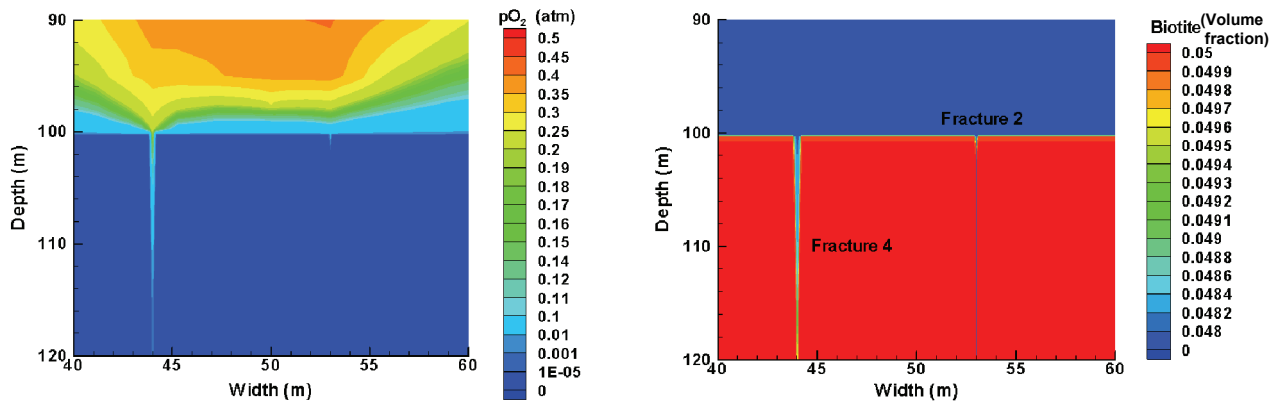
Figure 6-4: Results for Scenario 2 at a time of 12,000 years. a) pO_2 distribution, b) biotite distribution. Only a subregion of the model domain is shown.

Table 6-1: O_2 migration depth (based on pO_2 of 10^{-5} atm) for the base case and the four fracture network scenarios. The depths are in metres below the initial oxidizing-reducing interface depth of 100 m.

Vertical fracture	Base case	Fracture network scenario (m)			
		1	2	3	4
1	10.6	3.2	0	5.8	19.5
2	-	5.0	1.6	5.4	6.0
3	-	0	0	2.5 (end)	2.5 (end)
4	-	0	17.8	-	-

* end refers to the end of the respective fracture in the reducing zone.

7. STAGE V: EFFECT OF BOUNDARY CONDITIONS FOR SINGLE FRACTURE SCENARIOS

In the base case and Stage II analyses, recharge into the fracture and transport boundary conditions were assumed to be controlled by a 2,000 year interglacial period that was followed by a 10,000 year period of glacial melt water production (Figure 3-3). The durations of the interglacial period and the period of glacial melt water production were not varied and low recharge conditions, potentially resulting from permafrost periods coinciding with the onset of glaciation, were neglected. However, it is possible that the duration of glacial melt water production or limited recharge during times of permafrost may affect the depth of oxygen ingress, especially for cases where the depth was found to be significant (e.g. greater than 100 m into the reducing zone). Therefore in Stage V, the impact of a low recharge period and the duration of melt water production are investigated by conducting additional simulations for the base case parameters and four simulations selected from Stage II.

7.1. DESCRIPTION OF SIMULATIONS

After an initial interglacial period of 2,000 years, a 25,000 year period of permafrost is simulated, followed by a period of glacial melt water production ranging in duration from 1,000 to 10,000 years, yielding total simulation times ranging from 28,000 to 37,000 years (Figure 7-1). The period of permafrost is assumed to persist from the onset of the formation of an ice sheet until shortly after the glacial maximum, and its duration is based on results from a glaciation modelling realization that represents the longest continuous period of permafrost expected on the southern Canadian Shield (Peltier 2002). The range for the duration of melt water production is also based on the design base glacier scenario of Peltier (2002). Model output is provided at the end of the interglacial period, at the end of the permafrost period, and at the end of the period of melt water production.

The boundary conditions for flow and transport during the interglacial period and the period of glacial melt water production are identical to those applied in the base case and the respective Stage II simulations. During permafrost conditions, a Darcy velocity of 0 m yr^{-1} is used because shallow pore water is assumed to be frozen. A pO_2 value of 0.5 atm and a DOC value of 0 mg L^{-1} are assumed for permafrost conditions, which are identical to the base case values for the period of glacial melt water production (Figure 7-1).
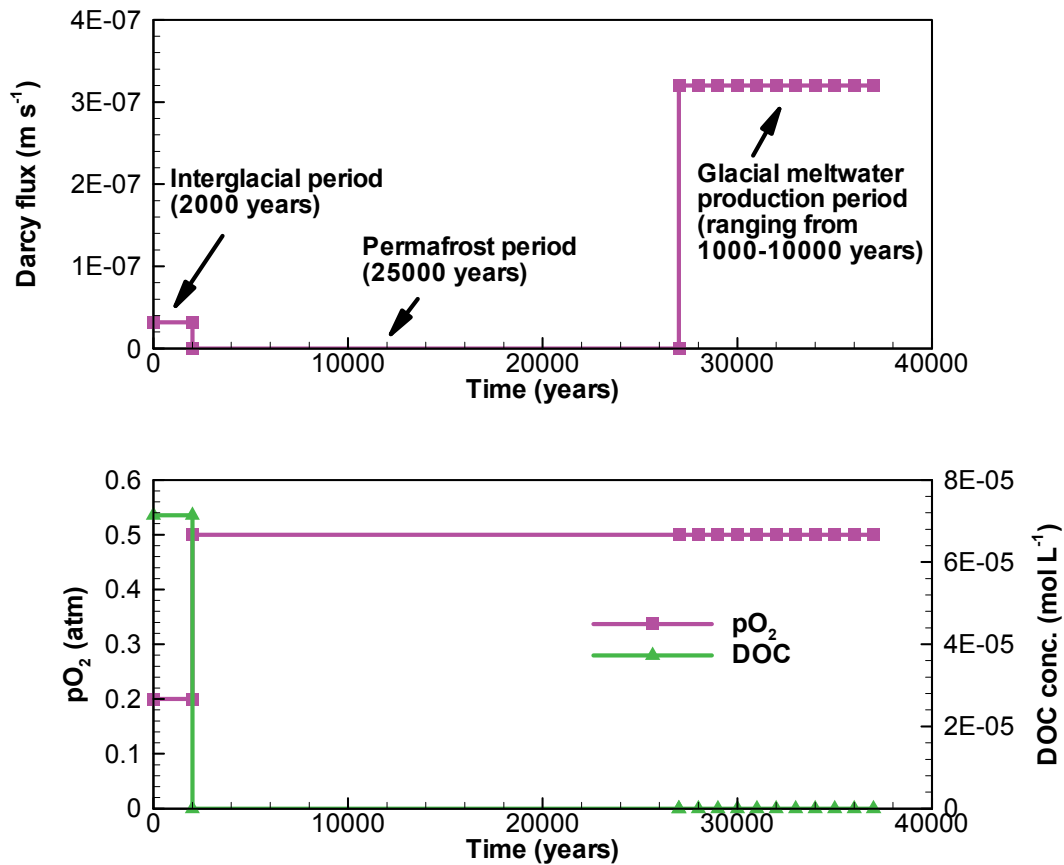
Figure 7-1: Simulation periods and flow and transport boundary conditions for the base case simulation including permafrost period.

These altered boundary conditions are applied to the Stage I base case and, to determine how these changed boundary conditions may affect O_2 transport for a variety of parameter combinations, several scenarios from the Stage II factorial analyses. In the factorial analyses, the simulations have been classified in "bins", which contain simulations that result in a specified range of O_2-penetration depths. Two scenarios from analysis 1 are selected; the first is a case in which the O_2 penetration depth is from the bin containing the maximum simulated penetration depth (220 m bin) and the second scenario is selected from the 160 m bin, which represents a penetration depth between the base case and the maximum case. Similarly, two scenarios from the data set of analysis 2 are chosen. To capture potential differences based on O_2 migration depth, two cases are randomly selected from the 300 and 600 m bins of O_2 penetration depth. Note that the value of the O_2 penetration depth from the 600 m bin is extrapolated as discussed in Section 4.2. Parameter values for the base case scenario and the four Stage II scenarios are listed in Table 7-1.

Table 7-1: Parameter values and O_2 penetration depths for the selected cases of Stage V.

	Data set for base case	Data sets from Stage II factorial analysis 1		Data sets from Stage II factorial analysis 2	
Bin for O_2 penetration (m)	100	160	220	300	600
D_a (m^2 s^{-1})	1.1×10^{-10}	5.40×10^{-11}	5.40×10^{-11}	1.40×10^{-11}	3.80×10^{-10}
φ_m	5.0×10^{-3}	1.00×10^{-2}	2.50×10^{-3}	2.20×10^{-3}	9.50×10^{-3}
q_f (m s^{-1}) – glacial period	3.17×10^{-7}	6.34×10^{-7}	6.34×10^{-7}	3.17×10^{-6}	3.17×10^{-6}
δ (m)	5×10^{-5}	1.00×10^{-4}	1.00×10^{-4}	5.00×10^{-4}	5.00×10^{-4}
pO_2 (atm) - glacial period	5.0×10^{-1}	1.00×10^{0}	1.00×10^{0}	2.10×10^{-1}	1.00×10^{0}
$f_{chlo\text{-}fracture}$	1×10^{-1}	2.00×10^{-1}	5.00×10^{-2}	3.00×10^{-1}	3.00×10^{-1}
$f_{bio\text{-}matrix}$	5.0×10^{-2}	2.50×10^{-2}	2.50×10^{-2}	1.30×10^{-1}	2.00×10^{-2}
$f_{pyr\text{-}matrix}$	1.0×10^{-6}	5.00×10^{-7}	5.00×10^{-7}	0	1.00×10^{-5}
$k_{chlo\text{-}fracture}$ (mol chlo) $/(L_{water}$ sec)	1.1×10^{-12}	2.25×10^{-12}	2.25×10^{-12}	1.12×10^{-13}	1.12×10^{-13}
$k_{bio\text{-}matrix}$ normalised with respect to $f_{bio\text{-}matrix}$ (mol bio) $/(L_{bulk}$ sec)	3.7×10^{-14}	1.85×10^{-14}	1.85×10^{-14}	3.71×10^{-13}	3.71×10^{-15}
O_2 penetration depth (after 2,000 years, end of interglacial period) (m)	102.1	102.5	103.1	102.9	103.7
O_2 penetration depth (after 3,000 years, i.e. 1,000 years after start of permafrost period) (m)	100.5	100.5	100.5	100.5	101.4
O_2 penetration depth (after 27,000 years, end of permafrost period) (m)	100.5	100.5	100.5	100.5	101.0
O_2 penetration depth (after 37,000 years) (m)	111.9	157.4	216.9	329.4	500 (626.8[1])

[1] extraploated value

7.2. RESULTS AND DISCUSSION

Table 7-1 presents the O_2 penetration depth in the fracture at four times during the simulations. Regardless of the parameter combinations, all cases show similar O_2 ingress at the end of the 2,000 year interglacial period. In addition, all cases exhibit a slight regression of the O_2 penetration depth at the onset of permafrost conditions. Due to the no-flow boundary condition imposed during permafrost, the depth of O_2 migration does not change significantly over the remainder of the permafrost period (Table 7-1).

The results from these selected simulations also suggest that the effect of the duration of melt water production is minimal within the range investigated (i.e. 1,000 to 10,000 years) (Figure 7-2). In most cases, a quasi-steady state condition is approached within 1,000 to 2,000 years. The results for the bin 300 simulation show this behaviour most clearly. A quasi-steady state condition is reached prior to 1,000 years and there is no further ingress after that time. The base case simulation and the examples from analysis 1 show a similar behaviour with a rapid initial response to melt water infiltration (penetration depth > 50% of maximum ingress after 1,000 years for all three cases). However, for the extreme case considered, in which the majority of the important parameters are at values that promote maximum O_2 migration (Table

7-1), quasi-steady state may not be achieved as rapidly and the migration rates of the O_2 front are more significant (e.g.: bin 160, bin 220 and bin 600 simulations in Figure 7-2). It does appear from these results, however, that the 10,000 year duration used in the base case and Stage II uncertainty analyses is conservative, and that if a shorter duration is used for the melt water production period this would have the effect of significantly reducing the O_2 migration depth only for those simulations with the greatest penetration depths.
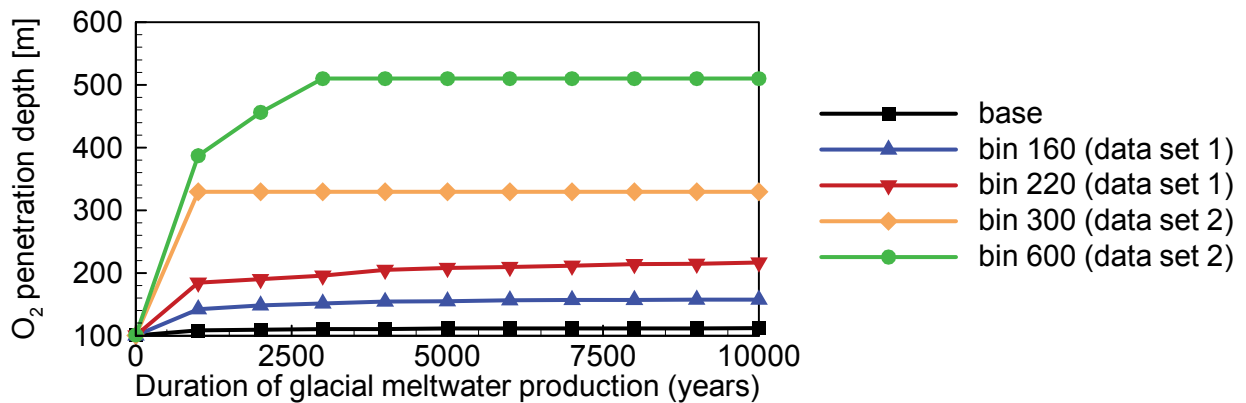

Figure 7-2: O_2-penetration depths as a function of the duration of glacial melt water production for the single fracture base case scenario and examples from 160 m and 220 m bins (Stage II, analysis 1), and 300 m and 600 m bins (Stage II, analysis 2).

8. STAGE VI: FRACTURE ZONE SCENARIOS

With the exception of Stage IV simulations, all previous scenarios assumed that groundwater flow occurs through a single discrete fracture. These discrete fractures contain only small volumes of chlorite, while the main redox buffer capacity is present in the adjacent matrix rock in the form of biotite and disseminated pyrite. Although this case is highly relevant, considering that widely-spaced discrete fractures occur in Canadian Shield rocks (McMurry and Ejeckam 2002, Gascoyne 2004), fracture zones consisting of intensely fractured rock are also present (Everitt and Read 1989, Stevenson et al. 1996, Davison et al. 1994, Chan and Stanchell 2004, Vilks et al. 2004). For example, three different domains of fracturing: intensely fractured rock or fracture zones (FZ), moderately fractured rock (MFR), and sparsely fractured rock (SFR) have been identified in both granitic and gneissic terrains at the WRA (URL and WL sites) (Stevenson et al. 1996).

In Stage VI, redox stability in fracture zones is investigated. These simulations are conducted using parameters comparable to those used in the base case single fracture scenario; however, it is assumed that the fracture zone is composed of a series of parallel vertical fractures. The number of fractures, fracture apertures, fracture spacing and fracture zone porosity are constrained by available field data (Everitt and Read 1989, Forst et al., 1995a and b, Stevenson et al. 1996).

The results for the FZ simulations are compared to those obtained for the single fracture base case and the results obtained by Glynn et al. (1997). In addition, an uncertainty analysis is conducted to determine the most important parameters controlling redox stability for the FZ scenario. To conduct the uncertainly analysis the FZ is represented as an equivalent porous medium (EPM) because this provides a more consistent basis for investigating variations of the FZ properties, while providing results that are essentially identical to those of the DFM approach.

8.1. DESCRIPTION OF THE FRACTURE ZONE (FZ) SCENARIOS

8.1.1. Parameters for comparison to single fracture base case

The fracture zone (FZ) simulations are based on the same parameter set as the single fracture (SF) case with the exception that the width of the fracture zone and the number of fractures within the fracture zone also need to be defined. A fracture zone half width of 0.25 m is simulated containing 49 fractures with an aperture of 1×10^{-4} m and one half fracture at the boundary (i.e. one fracture of aperture 5×10^{-5} m). This fracture zone width (i.e. 0.5 m considering symmetry) falls within the fracture zone range reported by Stevenson et al. (1996) and produces a fracture zone porosity of approximately 0.025, which is consistent with the fracture zone porosity range of 0.02 to 0.042 determined by Forst et al. (1995a, b). The key parameter values for the base case FZ scenarios are summarized in Table 8-1 in comparison to parameters of the SF scenario.

Table 8-1: Key parameter values for the single fracture base case and the fracture zone simulations.

Parameter	Single fracture	FZ1	FZ2
Fracture zone (FZ) width (m)	-	0.50	0.50
Number of fractures	1	99	99
Fracture aperture (m)	1×10^{-4}	1×10^{-4}	1×10^{-4}
Fracture Darcy velocity (m s^{-1})	3.2×10^{-8} (interglacial), 3.2×10^{-7} (glacial)	3.2×10^{-10} (interglacial), 3.2×10^{-9} (glacial)	1.6×10^{-8} (interglacial), 1.6×10^{-7} (glacial)
Matrix porosity	5×10^{-3}	5×10^{-3}	5×10^{-3}
Initial biotite volume fraction in matrix	5×10^{-2}	5×10^{-2}	5×10^{-2}
Initial pyrite volume fraction in matrix	1×10^{-6}	1×10^{-6}	1×10^{-6}
Initial chlorite volume fraction ($f_{chlo\text{-}fracture}$)	1×10^{-1}	1×10^{-1}	1×10^{-1}

Using the same parameter values as for the Stage I scenario has two important implications for the FZ simulations, a) the initial mass of chlorite in the domain will be increased by a factor equal to the number of fractures in the FZ, and b) oxygen mass loading will vary with the number of fractures. Because the dissolved O_2 boundary concentration is kept the same in the single fracture and FZ simulations, the Darcy flux in each individual fracture in the FZ is modified from that of the single fracture base case so that the oxygen mass flux to the FZ can be related to that of the single fracture. For example, in simulation FZ1 the Darcy flux in each fracture is reduced to maintain the same total O_2 mass loading as is simulated in the single fracture case. This modification results in significant reductions in the velocities (by a factor of approximately 100) in each fracture of the FZ. For the FZ2 simulation, the Darcy flux in each fracture is only reduced by a factor of 2 compared to the single fracture case which, because of the larger number of fractures in the FZ, has the effect of increasing the O_2 flux into the fracture zone by a factor of approximately 50 when compared to the single fracture case. This approach is considered to provide a conservative estimate for O_2 mass loading. Applying the same influx per fracture as for the single fracture scenario was considered unrealistic because it is unlikely that a fracture zone, extending to a depth of 500 m, would be connected to a fracture zone network with comparable permeability that would support flow of such magnitude to a discharge point.

8.1.2. Discretization

Base case simulations for FZ1 and FZ2 are conducted using the discrete fracture method (DFM). The total simulation domain is 50 m wide including the 0.25 m wide fracture zone and extends to a depth of 500 m. The discretization in horizontal direction contains 223 cells. The fracture spacing in the fracture zone is 5×10^{-3} m (5 mm), which is discretized into two cells between each set of fractures. The unfractured matrix is further discretized into 75 cells with a discretization interval that is fine near the fracture zone (0.03 m), and progressively coarsens away from the fracture zone to a maximum value of 3 m. In the vertical direction, a total of 378 cells are used with grid refinements near the ground surface and at the interface between oxidized and reducing zones. The total number of cells for this simulation is 84,294.

8.2. COMPARISON OF THE FRACTURE ZONE AND SINGLE FRACTURE SIMULATION RESULTS

For the FZ1 simulation, dissolved O_2 migration is limited to a depth of 1.4 m into the reducing zone (total depth of 101.4 m) after a simulation time of 12,000 years (results not shown). This compares with a depth of migration of approximately 12 m for the Stage I single fracture base case. The increased reduction potential in the fractures because of the increased availability of chlorite, the reduced Darcy velocity in each fracture of the FZ, and the increased fracture surface area facilitating diffusion into the matrix are considered the main factors causing the decreased O_2 migration compared to the single fracture result.

Conversely for the FZ2 simulation, as shown in Figure 8-1, the maximum depth of O_2 advance after 12,000 years is increased to 69 m below the initial oxidizing/reducing interface. This is the case despite a reduction of the Darcy velocity in the individual fractures by a factor of 2 in comparison to the single fracture scenario. This behaviour can be explained by complete oxygen penetration into the thin matrix slices within the fracture zone, which reduces the O_2-loss by matrix diffusion from individual fractures compared to a single fracture with a wide adjacent slice of matrix, therefore promoting greater vertical migration. Figure 8-2 confirms that matrix diffusion results in a relatively uniform distribution of O_2 within the FZ, while the diffusional migration distance into the adjacent rock matrix is approximately 25 cm. It also has to be emphasized that the increased vertical migration is obtained with an O_2 mass loading that is 50 times larger than the single fracture base case. The dissolution of biotite and pyrite within the matrix adjacent to the FZ corresponds well with the O_2 distribution as was demonstrated previously for the single fracture simulations (see Section 3.2). Similar to the single fracture results, a quasi-steady state distribution of O_2 is obtained, although this occurs about 2,000 years earlier than was observed in the single fracture scenario. After this condition is reached, the rate of O_2-front migration is less than 0.2 mm/yr (Figure 8-1).

Figure 8-3 and Figure 8-4 display chlorite and biotite distributions in the half fracture located at the symmetry boundary and in the adjacent rock matrix, respectively, for the FZ2 simulation. The consumption of chlorite and biotite are consistent with the single fracture results in that chlorite is only completely removed in the upper few metres of the fracture (compare Figure 3-8) and there is negligible consumption of biotite in the matrix (compare Figure 3-9). Pyrite in the matrix is completely dissolved to a depth of 67.4 m in the FZ2 scenario (results not shown).
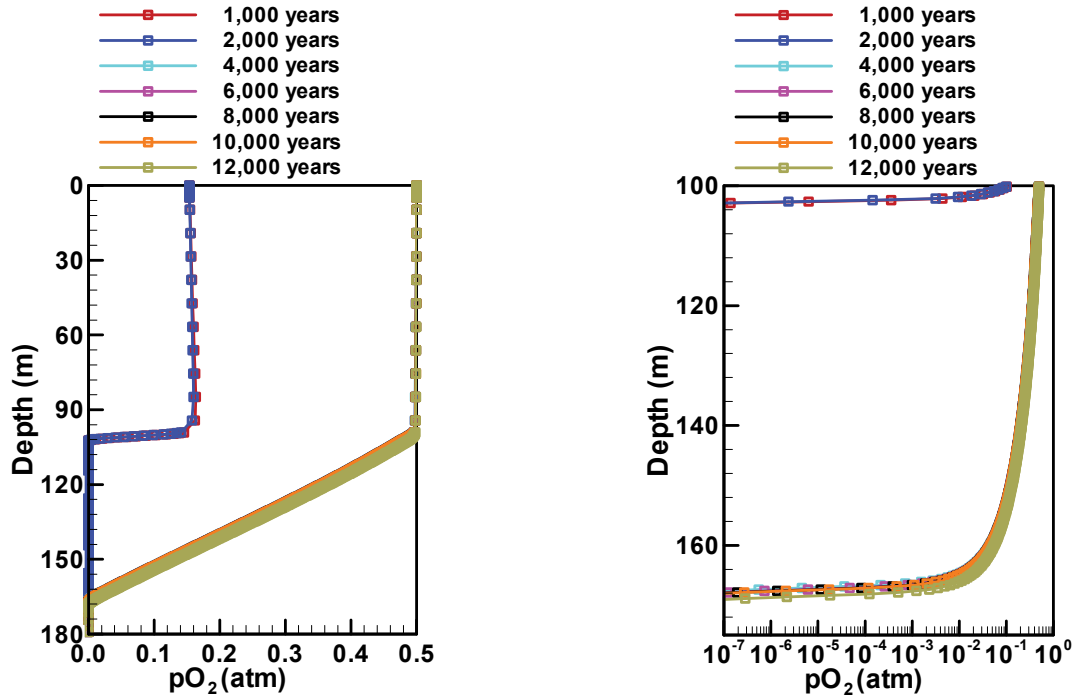
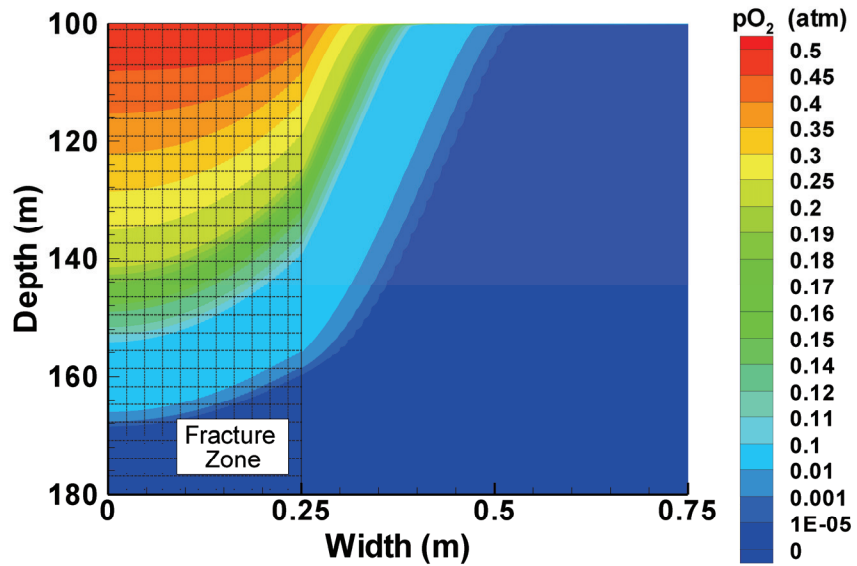Figure 8-1: pO₂ distribution in the first fracture of the fracture zone for simulation FZ2.

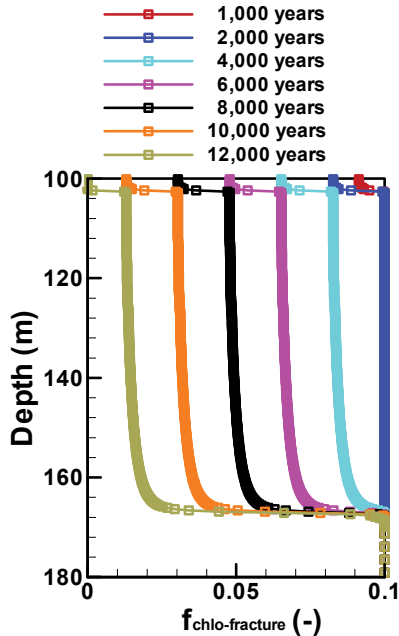Figure 8-2: pO₂ distribution at 12,000 years for the FZ2 scenario.

Figure 8-3: Chlorite distribution in the first fracture of the FZ for simulation FZ2.
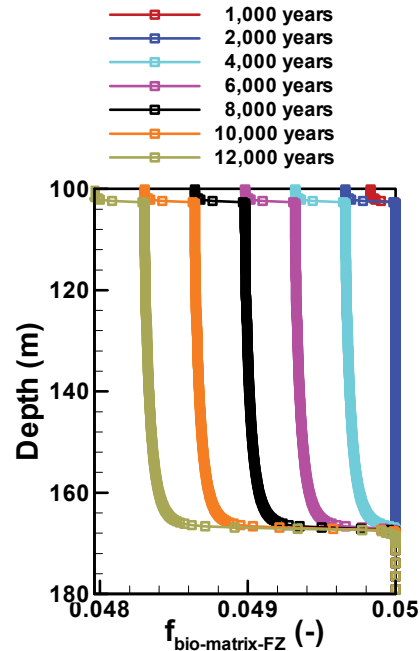
Figure 8-4: Biotite distribution in the first column of the matrix within the FZ for simulation FZ2.

8.3. COMPARISON WITH FINDINGS OF GLYNN ET AL. (1997)

Similar to the single fracture simulations, we compare the fracture zone simulations to the matrix skin-reaction model by Glynn et al. (1997). These simulations are also conducted using the discrete fracture method (DFM). Two different scenarios are considered:

- FZ-G-1: a 0.1 m wide half fracture zone, consistent with the domain dimensions used by Glynn et al. (1997), diffusion into the unfractured rock matrix adjacent to the fracture zone is excluded.
- FZ-G-2: a 0.25 m wide half fracture zone with an adjacent 49.75 m wide unfractured matrix, consistent with the domain of the FZ scenarios investigated in section 8.2.

The model parameters for fracture aperture, matrix porosity, apparent diffusion coefficient, influent dissolved O_2 concentration, biotite reaction rate, and biotite volume fraction are consistent with those of Glynn et al. (1997) (see also section 3.3). The fracture spacing in the fracture zone was selected to reproduce the effective fracture zone porosity used in the FZ-simulations as reported in Table 8-1.

The resulting simulation domain for scenario FZ-G-1 contains 7 fractures with an aperture of 2×10^{-4} m and a half-fracture at the symmetry boundary (Figure 8-5), yielding a fracture spacing of 1.4×10^{-2} m. Similar to scenario FZ-2, the simulation was conducted with an increased O_2-mass loading (by a factor of 7.5) and a reduced Darcy velocity in the individual fractures (by a factor of 2: $q_f = 1.24 \times 10^{-7}$ m s^{-1}). The simulation results for this scenario indicate deep O_2 penetration (Figure 8-6, Table 8-2, Cases 1 and 2). However, these simulations have a

restricted domain width of 0.1 m that does not consider diffusion of O_2 into the unfractured adjacent matrix, as was observed in the previous fracture zone simulations (section 8.2). To investigate this effect further, scenario FZ-G-2 is considered, which assumes the same fracture zone width as in the previous FZ-scenarios (including 18 fractures and one half fracture) and a wider unfractured matrix rock (Figure 8-7). Due to the wider fracture zone width, the mass loading is increased even more significantly (by a factor of 18.5) over the simulations by Glynn et al. (1997); however, O_2-penetration is restricted to a depth of 250 m (Figure 8-8, Table 8-2, Case 3). Even if the Darcy velocity in individual fractures is increased to the value used by Glynn et al. (1997), which corresponds to an increase in O_2-mass loading by a factor of 37, O_2 penetration does not reach the bottom boundary of the domain (Table 8-2, Case 4). These results highlight the importance of matrix diffusion.

Similar to the comparisons for the single fracture simulations, several key parameters are sequentially varied from the values discussed above to those used in the Stage I base case and the FZ-simulations (section 3 and section 8.2). For example, the oxygen concentration during the period of glacial melt water production has been reduced from that used in the original Glynn et al. (1997) scenario (Table 8-2, Case 5). Other simulations investigate the adjustment of the biotite reaction rate (Case 6), and the Darcy velocities in the individual fractures to base case values of the FZ scenario FZ-2 (Case 7) and the single fracture case (Case 8), respectively. For all scenarios that were based on simulation FZ-G-2, O_2 does not reach a depth of 500 m, despite the significantly increased O_2-mass loadings.

Figure 8-5: Configuration of FZ-simulation for comparison with Glynn et al. (1997) – Scenario FZ-G-1

Figure 8-6: Results of FZ-simulation for comparison with Glynn et al. (1997) – Scenario FZ-G-1. Two-dimensional pO_2 results are for a time of 10,000 years.
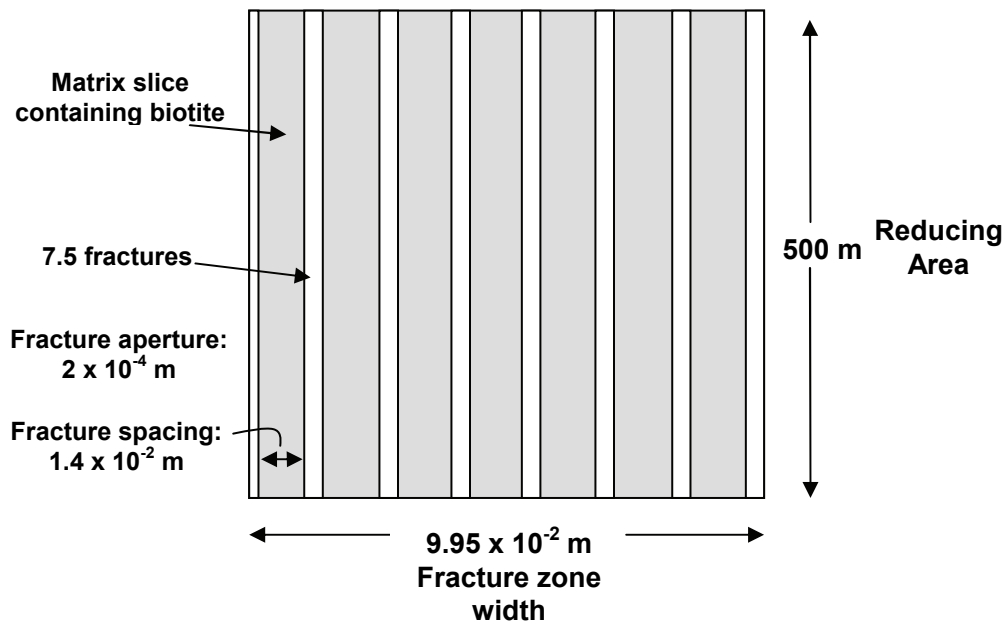

Figure 8-7: Configuration of FZ-simulation for comparison with Glynn et al. (1997) – Scenario FZ-G-2.
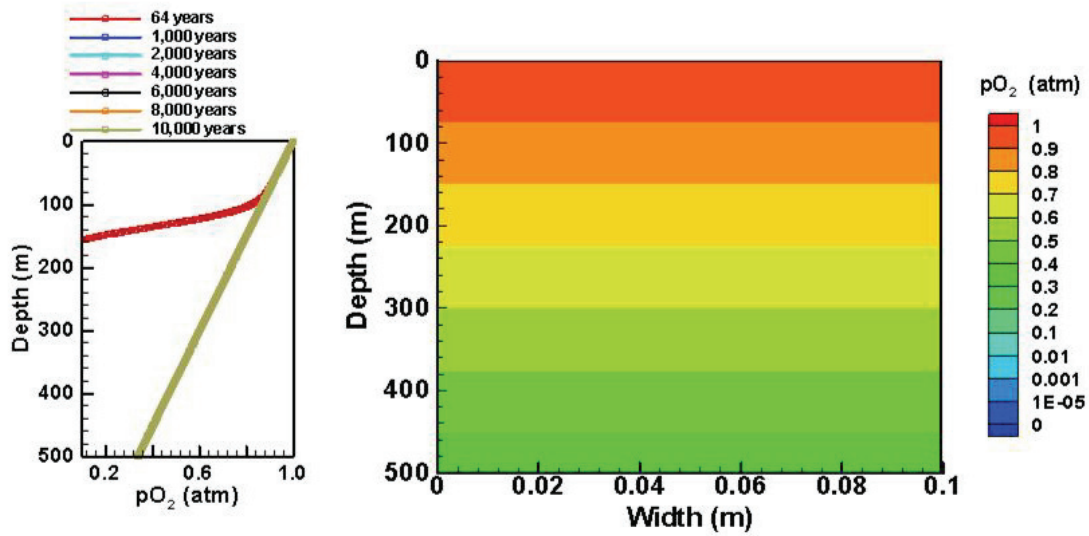
Figure 8-8: Results of FZ-simulation for comparison with Glynn et al. (1997) – Scenario FZ-G-2. Two-dimensional pO_2 results are for a time of 10,000 years.
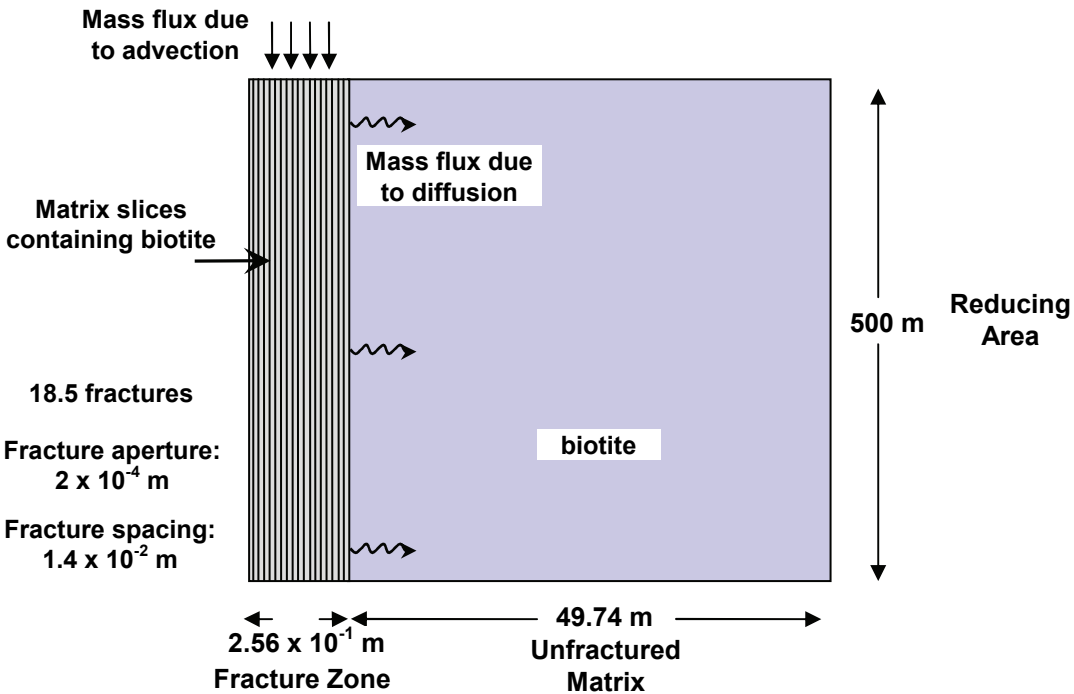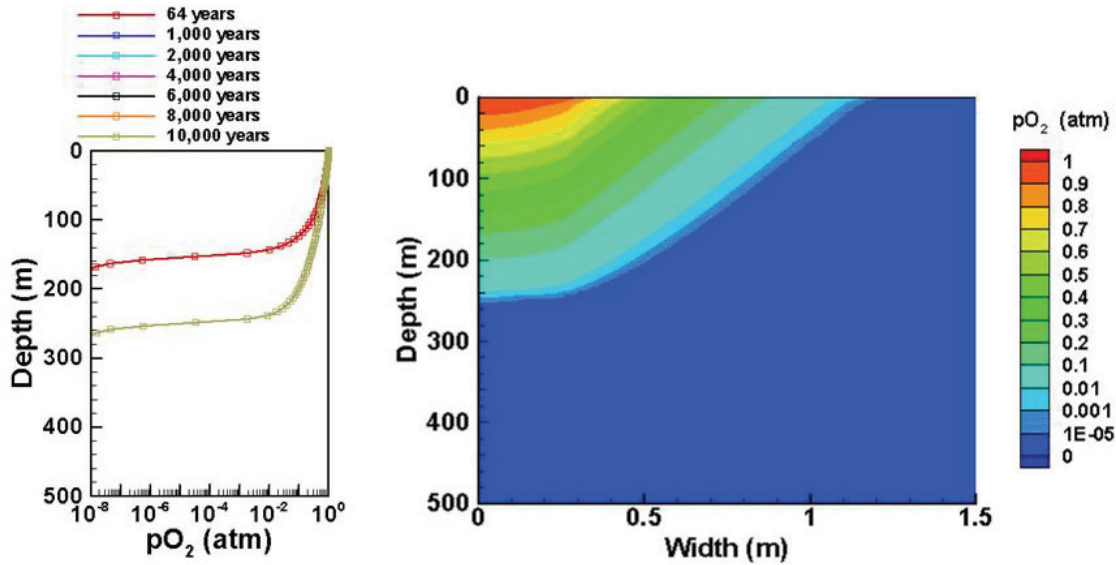
Table 8-2: Dissolved O_2 migration depths for Glynn-type FZ simulation and for selected parameter variations. Depths are for a pO_2 concentration 10^{-5} atm.

Case	Description	O_2 migration depth (m)
1	Scenario FZ-G-1	> 500
2	As 1) but with a Darcy velocity in the individual fractures increased to 2.48×10^{-7} m s^{-1} (Glynn et al. 1997)	> 500
3	Scenario FZ-G-2	250
4	As 3) but with a Darcy velocity in the individual fractures increased to 2.48×10^{-7} m s^{-1} (Glynn et al. 1997)	493
5	As 3) but O_2 concentration in recharge water reduced to 0.5 atm	158
6	As 5) but biotite reaction rate increased to the 3.7×10^{-14} mol m^{-2} s^{-1}	74
7	As 6) but with a Darcy velocity in the individual fractures increased to 1.6×10^{-7} m s^{-1} (FZ scenario FZ-2)	95
8	As 6) but with a Darcy velocity in the individual fractures increased to 3.2×10^{-7} m s^{-1} (single fracture base case)	186

8.4. FRACTURE ZONE PARAMETER UNCERTAINITY

Factorial analysis is used to identify the most important parameters for the FZ scenario. For this analysis, the fracture zone scenario FZ-2 with increased mass loading is used as the base case. Only O_2, DOC, biotite, chlorite and pyrite are simulated. To further increase computational efficiency, an equivalent porous medium (EPM) approach is used. It should be noted that only the fracture zone is treated as an EPM; matrix diffusion into the unfractured rock matrix adjacent to the FZ is explicitly considered. The applicability of this approach in comparison to the full DFM is evaluated in Appendix H.1. It is shown that the EPM provides

adequate accuracy for a range of representative test cases at a fraction of the computational cost.

8.4.1. Description of parameter ranges for the uncertainty analysis

The following set of parameters was selected for the uncertainty analysis:

1. apparent diffusion coefficient (D_a) of the rock matrix and fracture zone
2. matrix porosity (φ_m)
3. Darcy velocity in the individual fractures (q_f) during the period of melt water production
4. fracture zone half width (half FZ width)
5. pO_2 of the influent recharge melt water
6. chlorite abundance in the individual fractures ($f_{chlo-fracture}$)
7. biotite abundance in the matrix ($f_{bio-matrix}$)
8. pyrite abundance in the matrix ($f_{pyr-matrix}$)
9. chlorite reaction rate in the individual fractures ($k_{chlo-fracture}$), and
10. biotite reaction rate in the matrix ($k_{bio-matrix}$).

This parameter set is similar to that of the single fracture case; however, the fracture zone half width has been substituted for the fracture half aperture. As was done previously, mineral volume fractions and reaction rates are only varied for the reduced zone below a depth of 100 m. For the uncertainty analysis, the parameter values were decreased and increased by a factor two, to define the minimum and maximum parameter values, respectively. The complete set of parameters as well as D_{eff}, which is used to calculate D_a, is given in Table 8-3.

Table 8-3: Minimum and maximum parameter values used for the uncertainty analysis for the FZ scenario. The base case values for FZ scenario FZ-2 are shown for comparison.

Parameter	Case		
	Minimum	Base	Maximum
D_{eff} (m^2 s^{-1})	2.7×10^{-13}	5.4×10^{-13}	1.08×10^{-12}
D_a (m^2 s^{-1})	5.4×10^{-11}	1.08×10^{-10}	2.16×10^{-10}
Φ_{matrix}	2.5×10^{-3}	5.0×10^{-3}	1.0×10^{-2}
q_f (m s^{-1}) – period of glacial meltwater production	8.0×10^{-8}	1.6×10^{-7}	3.2×10^{-7}
FZ width (m)	0.125	0.25	0.5
pO_2 (atm) - period of glacial meltwater production	0.25	0.50	1.0
$f_{chlo-fracture}$	0.05	0.1	0.2
$f_{bio-matrix}$	0.025	0.5	0.1
$f_{pyr-matrix}$	5.0×10^{-7}	1.0×10^{-6}	2.0×10^{-6}
$k_{chlo-fracture}$ (mol chlo) (L$_{water}$ s)$^{-1}$	5.5×10^{-13}	1.1×10^{-12}	2.2×10^{-12}
$k_{bio-matrix}$ normalised with respect to $f_{bio-matrix}$ (mol bio) (L$_{bulk}$ s)$^{-1}$	1.85×10^{-14}	3.7×10^{-14}	7.4×10^{-14}

Table 8-4 provides an example of the dependent EPM FZ-parameters for the base case values. For the factorial analysis simulations, these parameters are dynamically updated based on the primary uncertainty parameters provided in Table 8-3. The number of fractures and fracture aperture are kept constant at 49.5 and 10^{-4} m, respectively. The scaling relationships between

the EPM-FZ-parameters and the discrete fracture and matrix parameters are described in Appendix H.2.

Table 8-4: Values of the scaled EPM parameters for the FZ-2 base case.

EPM-FZ Parameters	Value
ϕ_{FZ}	2.47×10^{-2}
q_{FZ} (m yr^{-1}) – glacial period	0.1
φ_{bio-FZ}	4.9×10^{-2}
k_{bio-FZ} normalised with respect to	3.63×10^{-14}
φ_{bio-FZ} (mol bio) $(L_{bulk}\ s)^{-1}$	
φ_{pyr-FZ}	9.8×10^{-7}
$k_{pyr-FZ}[O_2]^{0.5}$ normalised with respect to φ_{pyr-FZ} (mol pyr) $(L_{bulk}\ s)^{-1}$	9.83×10^{-13}
$\varphi_{chlo-FZ}$	1.98×10^{-3}
$k_{chlo-FZ}$ normalised with respect to	2.18×10^{-14}
$\varphi_{chlo-FZ}$ (mol chlo) $(L_{bulk}\ s)^{-1}$	

As was the case for the factorial analyses of the SF-system, the maximum depth of dissolved oxygen migration in the fracture zone at a time of 12,000 years is chosen as the response and a concentration criterion of 10^{-5} atm ($\sim 5 \times 10^{-4}$ mg L^{-1}) is used.

8.4.2. Results and discussion

The probability plot shown in Figure 8-9 and the analysis in Appendix I indicate that the Darcy velocity in the individual fractures (q_f), the oxygen concentration in the infiltrating melt water (pO_2), and the reaction rate of biotite ($k_{bio-matrix}$) are the most important parameters.

Parameters of lesser importance include the abundance and reactivity of chlorite ($f_{chlo-frature}$, $k_{chlo-fracture}$), the combined effect of $f_{chlo-fracture}$ and $k_{chlo-fracture}$, and the fracture zone width (FZ-width)   It is interesting to note that the Darcy velocity in the fractures and the biotite reaction rate consistently are identified as two of the most important parameters in both the FZ and single fracture scenarios (e.g. Figure 4-2, Figure 8-9). However for the FZ scenario, the oxygen content in the melt water and the chlorite volume fraction and reactivity have increased in importance, at the expense of the apparent diffusion coefficient (Figure 4-2, Figure 8-9). Considering the large number of fractures within a fracture zone, it is not surprising that chlorite volume fraction and reactivity have increased in importance. Chlorite content appears to be somewhat more important than the chlorite reaction rate (Figure 8-9, Appendix I).
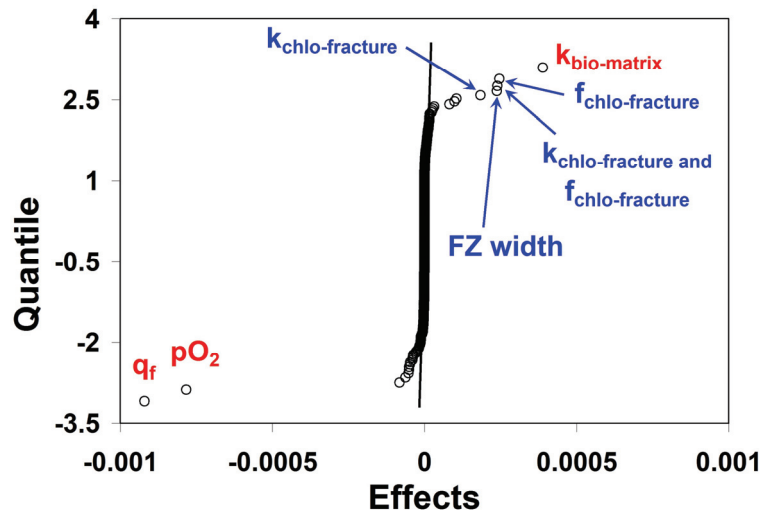
Figure 8-9: Probability plot of the effects for the FZ scenario (see Table 8-3 for parameter ranges).

8.4.3. Statistics of oxygen penetration depth

The geometric mean of the O_2 penetration depths for the FZ factorial analyses is 189.7 m, while the arithmetic mean is 210.9 m (standard deviation of 104 m). The means of the penetration depths are thus larger than for the comparable single fracture analysis (analysis 1, Table 4-3); however, this is expected given the significantly increased O_2-mass loading that is applied for the FZ simulations.

9. SUMMARY AND CONCLUSIONS

This study has investigated multicomponent reactive transport in sparsely fractured crystalline rock, with a particular focus on dissolved O_2 migration and attenuation during fracture-matrix interaction. For this work it is *a priori* assumed that a single fracture, fracture zone, or simplified fracture network, extends from the ground surface to a depth of 500 m and that groundwater flow in the fracture(s) is predominately vertical. This assumption is conservative because, as discussed in Section 1, several hydrogeological factors may preclude the circulation of near-surface groundwater beyond depths of several hundred metres. Furthermore, to simulate periods of glaciation, a recharge melt water composition was selected that has an elevated pO_2 of 0.5 atm and no dissolved organic carbon.

Based on a review of the literature, a set of parameter values considered representative of the Canadian Shield was established for use in the a single-fracture base case developed to explore the processes that attenuate dissolved oxygen ingress. In the base case, fracture velocities were 3.2×10^{-8} m/s and 3.2×10^{-7} m/s during the interglacial and glacial periods, respectively. The results for the single fracture base case demonstrate that the depth of migration of dissolved O_2 into a previously reducing fracture-matrix system is limited to less than 15 m below the assumed zone of oxygenated groundwater during a 10,000 year period of melt water recharge with elevated pO_2. The migration of dissolved O_2 in the fracture essentially achieves quasi-steady state after 8,000 years because of the combined effects of matrix diffusion and reaction with reduced iron minerals, especially biotite, in the rock matrix. The small amount of pyrite that is assumed to be initially present in the matrix is rapidly depleted and has little influence on the penetration of dissolved O_2. Furthermore, the results indicate that over the duration of the simulations, a wedge-shaped alteration zone, with a thickness on the order of 10 cm, develops adjacent to the fracture as oxygen ingresses into the rock matrix. This alteration zone could be a useful long-term record of oxygen migration; however, no experimental or field analogues of matrix alteration currently exist for crystalline rocks of the Canadian Shield. Such evidence would have to be collected adjacent to a fracture, or fracture zone, that is known to be hydraulically active and has received oxygenated water recharge. Cavé et al. 2006 used analytical Transmission Electron Microscopy to identify evidence of oxidative weathering in drill core samples taken adjacent to vertical fractures (assumed to be the main groundwater recharge pathways at depths between 7 and 240 m below surface at the Whiteshell Research Area). However, for the fractures examined in their study, no zone of oxidative alteration was observed adjacent to the fracture.

Scenarios are also developed for a fracture zone that contains multiple parallel fractures. These scenarios include i) a case with the same O_2-mass loading as the single fracture case, which because of the multiple fractures is achieved by having decreased fracture velocities, and ii) a scenario that has significantly increased O_2-mass loading. The results for scenario i) show a much lower O_2-penetration depth when compared to the single fracture case. This is due to the abundance of fractures which results in higher accessibility to reduced mineral phases. However, for scenario ii) with a higher O_2-mass loading, penetration depths are deeper than for the single fracture scenario. Nevertheless, the results of the fracture zone simulations indicate a maximum ingress of approximately 70 m into the reducing zone below the assumed zone of oxygenated groundwater. These simulations therefore explicitly demonstrate the importance of knowing the magnitude of the flow velocities within the fracture zones, as these velocities will have a significant impact on the O_2-penetration depth. The velocities assigned for fracture zone

scenario FZ2 are considered conservative in the sense they are relatively high and are assumed invariant with depth; although work by Sykes et al. (2003) suggests that groundwater flow should decrease with depth because of reduced bulk permeability and the presence of saline pore water. Furthermore, a continuous high permeability flow path would be required between recharge and discharge locations to sustain such deep-seated flow, which is considered unlikely in granitic media of the Canadian Shield.

Although the results obtained in the single-fracture and fracture zone base cases, which have used the best available information for model parameterization, suggest O_2 migration under glacial conditions will be limited, previous scoping calculations by others have suggested otherwise. For example, Glynn et al. (1997) used a simplified fracture/matrix-skin model that indicated dissolved O_2 could migrate to depths exceeding 500 m in fractured crystalline rock. The current conceptual models for the single fracture-matrix system and fracture zone are also compared to the scenario of Glynn et al. (1997). Using a parameter set derived from Glynn et al. (1997), the current models typically suggest significantly shallower oxygen penetration depths than predicted by Glynn et al. (1997). For the single fracture model, a maximum O_2-penetration depth of 100 m into the reducing zone is obtained. The O_2 penetration depths for the fracture zone model are larger, but O_2 advance is significantly slower and penetration depth is less than 500 m, despite specifying a much higher O_2-mass loading than used by Glynn et al. (1997). It is noteworthy that O_2 only reaches 500 m for cases where diffusion into the adjacent unfractured rock matrix is neglected by specifying a narrow width of the fracture zone (0.1 m), consistent with the dimensions assumed by Glynn et al. (1997). This finding highlights the importance of matrix diffusion on O_2-ingress.

The differences between the current results and those obtained by Glynn et al. (1997) are attributed to the different underlying conceptual models. The matrix-skin-reaction model of Glynn et al. (1997) deals with O_2 transport in a simplified manner because it assumes that a) dissolved oxygen is initially present throughout the 500 m deep fracture-matrix-skin domain, and b) any O_2 consumed by biotite dissolution in the matrix is instantaneously replaced. Consequently, the main differences between the approach of Glynn et al. (1997) and that used here are that in the present model O_2 is initially absent from the domain, O_2-containing recharge water enters the fracture matrix system through the fracture only, and O_2 can only enter into the rock matrix by diffusive transport from the fracture. If matrix diffusion does dominate the transfer of dissolved O_2 to regions containing reduced minerals, which will likely be the case for open fractures in relatively unaltered rock, then the present mechanistic model should more closely represent the key processes during recharge of O_2-bearing glacial waters in fractured crystalline rock.

To determine the most important parameters controlling the advance of O_2, uncertainty analyses are carried out for the single fracture and fracture zone scenarios using 2^k factorial analyses. This analysis method requires maximum and minimum values for all parameters considered, and for the single fracture case two analyses are conducted using different parameter ranges (maximum and minimum values differ from the base case values by a factor of 2; and maximum and minimum values differ based on reported ranges in field data and accounting for parameter uncertainty). Independent of the parameter ranges, the most influential factors dominating O_2 ingress are identified as fracture flow velocity, fracture aperture and the dissolution rate of biotite in the rock matrix. For the fracture zone scenario, maximum and minimum values are defined by a departure from the base case values by a factor of 2. This analysis reveals that the most influential parameters are fracture flow velocity, pO_2 concentration in the melt water, the dissolution rate of biotite, and to a lesser degree the

abundance and reactivity of chlorite, and the fracture zone width. These results demonstrate that overall, the flow velocities in the fracture and the reactivity of biotite in the matrix will likely provide major controls on O_2 ingress. Further constraining these parameters will therefore significantly increase confidence in simulation results. These parameters are, however, two of the more difficult to accurately determine because i) the fracture velocity will be spatially variable and controlled by fracture aperture, fracture network interconnectivity, and large-scale flow systems dynamics, and ii) the biotite reaction rate in unfractured crystalline rock is poorly defined because of uncertainties in accessible reactive surface area and temporal changes in mineral surface reactivity. The integration of reactive transport simulations with flow simulations in fracture networks (which was beyond the scope of the present work) may be a useful, but computationally demanding, approach to deal with the uncertainty in fracture flow velocity, while detailed investigations of matrix mineral alteration adjacent to fractures may lead to better constraints on biotite reactivity.

When a DCM approach is used to simulate oxygenated water migration and attenuation in a single-fracture/matrix scenario, it is found that O_2-profiles can be produced that compare well to those predicted by a DFM. However, for sparsely fractured rock, it does not appear possible to *a priori* determine appropriate values for the DCM mass transfer coefficient, and differences in the consumption and distribution of matrix mineral phases (e.g. biotite, pyrite) highlight that the current formulations for DCM applied in this study are limited in their capability to resolve the spatial and temporal evolution of mineral alteration.

In addition, simulations are conducted for a series of simplified 2D-fracture matrix systems to test the extensibility of the DFM approach to multi-dimensional reactive transport systems and to illustrate the potential effect of fracture networks on the ingress of O_2. The results suggest that simulations are feasible for simple fracture networks with a relatively simple geochemical reaction system; however, for large-scale 3D fracture networks on the scale of 100s of metres, a more computationally feasible approach will be needed. The results also show that O_2 penetration is affected by the configuration of the fracture network and may be slightly deeper, or shallower, than for the single fracture case.

The effect of recharge boundary conditions during glaciation events is also investigated. To accomplish this, the base case for the single fracture scenario is modified to include a 25,000 year long period of permafrost followed by a period of melt water production which varies in duration from 1000 to 10000 years. Zero recharge is specified during the permafrost period because of the assumption of frozen ground conditions. Simulations are carried out for a number of cases from the single fracture scenerios (Stages I and II) and the results suggest that the occurrence of permafrost has no effect on the maximum depth of O_2 ingress. Furthermore, the effect of the duration of glacial melt water production is limited within the range of 1,000 to 10,000 years. This range is consistent with the expected duration of warm-based ice sheets as simulated by Peltier (2002) and thus it is concluded that the use of 10,000 years for the duration of melt water production in this study is conservative (i.e. promotes O_2 ingress). Dissolved oxygen profiles approach a quasi-steady state condition about 1,000 to 4,000 years after the start of melt water production. After achieving the quasi-steady state, the rate of advancement is less than 1 mm/yr in most cases. However, for extreme cases, in which the majority of the important parameters are at values that promote maximum O_2 migration, the rate of front migration may be more significant.

REFERENCES

Abry, D.R.M., R.G.F. Abry, K.V. Ticknor, and T.T. Vandergraaf. 1982. Procedure to determine sorption coefficients of radionuclides on rock coupons under static conditions. Atomic Energy of Canada Limited Technical Record TR-189. Pinewa, Canada.

Alonso, U., T. Missana, A. Patelli, V. Rigato and P. Rivas. 2003. Study of the contaminant transport into granite microfractures using nuclear ion beam techniques. J. Contaminant Hydrology. 61(1-4): 95-105.

Amos, R.T., K.U. Mayer, D.W. Blowes, and C.J. Ptacek. 2004. Reactive transport modeling of column experiments for the remediation of acid mine drainage. Environmental Science & Technology. 38: 3131-3138.

Andersson, P., E. Gustafsson and O. Olsson. 1989. Investigations of flow distribution in a fractured zone at the Stripa mine, using the radar method, results and interpretation. SKB (Swedish Nuclear Fuel and Waste Management Company), Stockholm, TR 89-33.

Appelo, C. A. J., and D. Postma. 2005. Geochemistry, Groundwater and Pollution, 2nd Edition. A. A. Balkema, Leiden, The Netherlands.

Bahr, J. M., and J. Rubin. 1987. Direct comparison of kinetic and local equilibrium formulations for solute transport affected by surface reactions. Water Resour. Res. 23: 438–452.

Bradbury, M.H. and A. Green. 1985. Measurement of important parameters determining aqueous phase diffusion rates through crystalline rock matrices. J. Hydrology. 82: 39-55.

Cavé L. C. and T. A. Al. 2006. Paleohydrogeology – Analytical TEM investigation of mineral weathering in the Whiteshell Research Area. Ontario Power Generation Report No. 06819-REP-01200-10156-R00.

Chan, T., and F.W. Stanchell. 2004. Decovalex III BMT3 (the glaciation bench mark test) final research team report. Ontario Power Generation, Nuclear Waste Management, Report No: 06819-REP-01300-10091-R00.

Cheng, L. 2005. Dual porosity reactive transport modelling, Ph.D.-thesis, Univ Sheffield, U.K.

Choi, J.W., and D.W. Oscarson. 1996. Diffusive transport through compacted Na- and Ca-bentonite. J. Contaminant Hydrology. 22:189-202.

Davison, C.C., T. Chan, and A. Brown. 1994. The disposal of Canada's nuclear fuel waste: The geosphere model for postclosure assessment. Atomic Energy of Canada Limited (AECL) Research, AECL-10719.

Devore, J.L., and N.R. Farnum. 1999. Applied Statistics for Engineers and Scientists. Duxbury Press, an imprint of Brooks/Cole Publishing Company.

Everitt, R. A. and R.S. Read. 1989. Geology of the 240 level of the underground research laboratory. Volume 1 - General Geology. Atomic Energy of Canada Limited. Technical Report TR-491-1.

Everitt, R.A., A. Brown, R. Ejeckam, R. Sikorsky, and D. Woodcock. 1998. Litho-structural layering within the Archean Lac du Bonnet Batholith, at AECL's Underground Research Laboratory, Southeastern Manitoba. Journal of Structural Geology. 20(9/10):1291-1304.

Everitt, R.A. 2001. The influence of rock fabric on excavation damage in the Lac Du Bonnet Granite. Ph.D. thesis, University of Manitoba, Winnipeg, Manitoba.

Everitt, R.A. 2004. Personal communication.

Frost, L.H., C.C. Davison and N.W. Scheier. 1995a. Two-well radioactive tracer experiment in a major fracture zone in granite. Atomic Energy of Canada Limited Technical Record TR-671.

Frost, L.H., C.C. Davison and N.W. Scheier. 1995b. Transport properties in highly fractured rock experiment - Phase 1 tracer tests in fracture zone 2. Atomic Energy of Canada Limited Technical Record TR-672. COG-95-85.

Gascoyne, M. 1986. SCSB – A standard Canadian Shield brine. Atomic Energy of Canada Limited Technical Record TR-403. Pinawa, Canada.

Gascoyne, M. 2000. Hydrogeochemistry of the Whiteshell Research Area. Ontario Power Generation Report No. 06819-REP-01200-10033 R00.

Gascoyne, M. 2004. Hydrogeochemistry, groundwater ages and sources of salts in a granitic batholith on the Canadian Shield, southeastern Manitoba. Applied Geochemistry. 19: 519–560.

Glynn, P.D., C.I. Voss, and A.M. Provost. 1997. Deep penetration of oxygenated meltwaters from warm based ice sheets into the Fennoscandian Shield, In: Use of Hydrogeochemical Information in testing Groundwater Flow Models, Workshop Proceedings. Borgholm. Sweden. pp.201-241.

Guimerà J., L. Duro, S. Jordana, and J. Bruno. 1999. Effects of ice melting and redox front migration in fractured rocks of low permeability. Svensk Kärnbränslehantering AB. Report no. TR-99-19.

Knapp, R. B. 1989. Spatial and temporal scales of local equilibrium in dynamic fluid-rock systems. Geochim. Cosmochim. Acta. 53: 1955–1964.

Lensing, H.J., M. Vogt, and B. Herrling. 1994. Modeling of biologically mediated redox processes in the subsurface, J. Hydrology, 159: 125-143.

Lichtner, P. C. 1985. Continuum model for simultaneous chemical reactions and mass transport in hydrothermal systems. Geochim. Cosmochim. Acta. 49: 779–800.

Lichtner, P. C. 1993. Scaling properties of time-space kinetic mass transport equations and the local equilibrium limit. Am. J. Sci. 293: 257–296.

Lichtner, P. C. 2000. Critique of dual continuum formulations of multicomponent reactive transport in fractured porous media. In: Dynamics in Fractured Rock, Eds.: B. Faybishenko, P.A. Witherspoon, and S.M. Benson, Geophysical Monograph 122, American Geophysical Union. Washington, DC.

MacQuarrie, K.T.M., and K.U. Mayer. 2004. Reactive transport modeling in fractured rock: State of the science review. Ontario Power Generation, Nuclear Waste Management, Report No: 06819-REP-01200-10117-R00.

Malmström, M., S. Banwart, J. Lewenhagen, L. Duro, and J. Bruno. 1996. The dissolution of biotite and chlorite at $25^{o}C$ in the near-neutral pH region. J. Contaminant Hydrology. 21: 201-213.

Malmström, M., and S. Banwart. 1997. Biotite dissolution at $25^{O}C$: The pH dependence of dissolution rate and stoichiometry. Geochimica Cosmochimica Acta, 61(14): 2779-2799.

Mayer, K. U., S. G. Benner, E. O. Frind, S. F. Thornton, and D. L. Lerner, 2001. Reactive transport modeling of processes controlling the distribution and natural attenuation of phenolic compounds in a deep sandstone aquifer, *J. Contam. Hydrol.*, 53:341-368.

Mayer, K. U., E. O. Frind, and D. W. Blowes, 2002. Multicomponent reactive transport modeling in variably saturated porous media using a generalized formulation for kinetically controlled reactions, Water Resour. Res. 38, 1174, doi: 10:1029/2001WR000862.

Mayer, K.U., S. G. Benner, and D. W. Blowes, 2006. Process-based reactive transport modeling of a permeable reactive barrier for the treatment of mine drainage, J. Contam. Hydrol., in press, available on-line March 22, 2006

McMurry, J. 2000. Evaluating effects of deep recharge by a low-salinity, oxidizing groundwater: a geochemical modelling case study. Ontario Power Generation Report No. 06819-REP-01300-10007 R00.

McMurry, J. 2004. Reference water compositions for a deep geologic repository in the Canadian Shield. Ontario Power Generation, Nuclear Waste Management, Report No.: 06819-REP-01200-10135-R01.

McMurry, J., and R.B. Ejeckam. 2002. Paleohydrogeological study of fracture mineralogy in the Whiteshell Research Area. Ontario Power Generation Report No. 06819-REP-01200-10082-R00.

Murphy, S. F., S. L. Brantley, A. E. Blum, A. F. White and H. Dong. 1998. Chemical weathering in a tropical watershed, Luquillo Mountains, Puerto Rico: II. Rate and mechanism of biotite weathering. Geochimica et Cosmochimica Acta. 62(2): 227-243.

Neretnieks, I., T. Eriksen, and P. Tähtinen. 1982. Tracer movement in a single fissure in granitic rock: Some experimental results and their interpretation. Water Resources Research. 18(4): 849-858.

Nirex (United Kingdom Nirex Limited). 1997. Nirex 97: An assessment of the post-closure performance of a deep waste repository at Sellafield. United Kingdom Nirex Limited, Science Report S/97/012.

NWMO 2005. Choosing a way forward: The future management of Canada's used nuclear fuel. Nuclear Waste Management Organization. Toronto, Canada. www.nwmo.ca

Ohlsson, Y., and I. Neretnieks. 1995. Literature survey of matrix diffusion theory and of experiments and data including natural analogues. SKB Technical Report, 95-12.

Oscarson, D.W., and H.B. Hume. 1994. Diffusion of 14C in dense saturated bentonite under steady-state conditions. Transport in Porous Media. 14, 73-84.

Park, S.S., and P.R. Jaffe. 1996. Development of a sediment redox potential model for the assessment of postdepositional metal mobility. Ecological Modelling. 91, 169-181.

Peltier, W. R. 2002. A design basis glacier scenario, Ontario Power Generation Report No: 06819-REP-01200-10069-R00.

Pitkänen, P., S. Partamies, and A. Luukkonen. 2004. Hydrogeochemical interpretation of baseline groundwater conditions at the Olkiluoto site. POSIVA Report No. 2003-07. http://www.posiva.fi/raportit/Posiva_2003-07.pdf.

Puigdomenech, I., J-P. Ambrosi, L. Eisenlohr, J-E. Lartigue, S. A. Banwart, K. Bateman, A.E. Milodowski, J.M. West, L. Griffault, E. Gustafsson, K. Hama, H. Yoshida, S. Kotelnikova, K. Pedersen, V. Michaud, L. Trotignon, J. Rivas Perez, and E-L Tullborg. 2001a. O_2 depletion in granitic media – the REX project. Svensk Kärnbränslehantering AB. Report no. TR-01-05.

Puigdomenech, I. (ed), I. Gurban, M. Laaksoharju, A. Luukkonen, J. Lofman, P. Pitkanen, I. Rhen, P. Ruotsalainen, J. Smellie, M. Snellman, U. Svensson, E-L. Tullborg, B. Wallin, U. Vuorinen, P. Wikberg. 2001b. Hydrochemical stability of groundwaters surrounding a spent nuclear fuel repository in a 100,000 year perspective. Posiva Report No. 2001-06.

Samson, S.D., K.L. Nagy, and W.B. Cotton. 2005. Transient and quasi-steady-state dissolution of biotite at 22–25°C in high pH, sodium, nitrate, and aluminate solutions. Geochimica et Cosmochimica Acta. 69(2): 399–413.

Schild, M., S. Siegesmund, A. Vollbrecht and M. Mazurek. 2001. Characterization of granite matrix porosity and pore-space geometry by *in situ* and laboratory methods. Geophysical J. International. 146: 111-125.

Sevougian, S. D., R. S. Schechter, and L. W. Lake. 1993. Effect of partial local equilibrium on the propagation of precipitation/dissolution waves, Ind. Eng. Chem. Res. 32: 2281–2304.

Shapiro, A.M., 2001. Effective matrix diffusion in kilometre-scale transport in fractured crystalline rock. Water Resour. Res. 37:507-522.

SKB (Swedish Nuclear Fuel and Waste Management Company). 1999. Deep repository for spent nuclear fuel. SR 97 - Post-closure safety. Main report - Volume 1, Volume 2, and Summary. Swedish Nuclear Fuel and Waste Management Company (KBS), Technical Report SKB TR-99-06.

SKI (Swedish Nuclear Power Inspectorate) 1996. SKI SITE-94: Deep repository performance assessment project. SKI Report 96:36 (2 Volumes).

Steefel, C. I., D. J. DePaolo, and P. C. Lichtner. 2005. Reactive transport modelling: An essential tool and a new research approach for the earth sciences. Earth and Planetary Sci. Let., 240: 539-558.

Steefel, C. I., and A. C. Lasaga. 1994. A coupled model for transport of multiple chemical species and kinetic precipitation/dissolution reactions with application to reactive flow in single phase hydrothermal systems. Am. J. Sci. 294: 529–592.

Steefel, C. I., and P. C. Lichtner. 1998a. Multicomponent reactive transport in discrete fractures: I. Controls on reaction front geometry. J. Hydrology. 209:186-199.

Steefel, C. I., and P. C. Lichtner. 1998b. Multicomponent reactive transport in discrete fractures: II. Infiltration of hyperalkaline groundwater at Maqarin, Jordan, a natural analogue site. J. Hydrology. 209: 200-224.

Steefel, C. I., and K.T.B. MacQuarrie. 1996. Approaches to modeling of reactive transport in porous media, in Reactive Transport in Porous Media, Rev. Mineral. 34: 83–129.

Stevenson, D.R., Brown, A., Davison, C.C., Gascoyne, M., McGregor, R.G., Ophuri, D.U., Scheier, N.W., Stanchell, F., Thorne, G.A. and Tomsons, D.K. 1996. A Revised Conceptual Hydrogeologic Model of a Crystalline Rock Environment, Whiteshell Research Area, Southeastern Manitoba, Canada. Atomic Energy of Canada Limited, Report AECL-11331, COG-95-271.

Sykes, J.F., S.D. Normani, and E.A. Sudicky. 2003. Regional scale groundwater flow in a Canadian Shield setting. Ontario Power Generation, Nuclear Waste Management, Report No: 06819-REP-01200-10114-R00.

Vieno, T. and H. Nordman. 1999. Safety assessment of spent fuel disposal in Hästholmen, Kivetty, Olkiluoto and Romuvaara (TILA-99). Helsinki, Posiva Report, POSIVA-99-07.

Vilks, P., N.H. Miller, and F.W. Stanchell. 2004. Phase II in-situ diffusion experiment. Ontario Power Generation, Nuclear Waste Management, Report No: 06819-REP-01200-10128-R00.

White, A.F., and S.L. Brantley. 2003. The effect of time on the weathering of silicate minerals: why do weathering rates differ in the laboratory and field? Chemical Geology. 202: 479-506.

White, A.F., and M.L. Peterson. 1990. Role of reactive-surface area characterization in geochemical kinetic models, in Chemical Modeling of Aqueous Systems II, edited by

D.C. Melchior, and R.L. Bassett, Chapter 35: 461-475. Washington, D.C., American Chemical Society.

Williamson, M.A., and J. D. Rimstidt. 1994. The kinetics and electrochemical rate-determining step of aqueous pyrite oxidation, Geochim. Cosmochim. Acta. 58: 5443-5454.

Yeh, G. T., and V.S. Tripathi. 1989. A critical evaluation of recent developments in hydrogeochemical transport models of reactive multichemical components. Water Resour. Res. 25: 93–108.

Zheng, C. and G.D. Bennett. 2002. Applied Contaminant Transport Modeling, Second Edition. John Wiley & Sons, New York.

APPENDIX A   LITERATURE REVIEW OF KEY MODEL PARAMETERS

CONTENTS

LIST OF TABLES

The simulation of reactive transport in sparsely fractured granitic bedrock typical of the Canadian Shield requires the specification of processes and parameters which characterize present day and future conditions. Based on previous research (e.g., Glynn et al. 1997, Steefel and Lichtner 1998a, MacQuarrie and Mayer 2004) the following parameters and processes are considered of primary importance for simulating reactive transport through a single fracture in granitic bedrock:

1. Fracture aperture (2δ)
2. Darcy velocity (q_f) in fracture
3. Fracture longitudinal dispersivity
4. Porosity (φ_m) and permeability of rock matrix
5. Effective diffusion coefficient (D_{eff}) of rock matrix
6. Transport boundary conditions
7. Mineral abundance in fracture and matrix, and
8. Biogeochemical reactions and rates.

A literature review was performed to identify appropriate parameter values and reactions to be used in the base case scenario (Stage I) and uncertainty analysis (Stage II). The following subsections summarize the results of the literature review. When available, parameter values specific to the Canadian Shield are considered; however, for parameters with insufficient site-specific data other literature was consulted.

A.1 FRACTURE APERTURE

Fracture aperture is an important parameter because it influences fracture permeability, or for a given Darcy velocity, mass loading through the fracture. In other words, the ratio of fracture volume/fracture surface area is primarily related to fracture aperture. For a specified Darcy velocity, the larger the fracture aperture, the higher the mass loading per fracture surface area.

Brush (2001, 2003) summarized mean aperture data from 11 sources and reported a range from 4.7×10^{-5} to 1.0×10^{-3} m. This range, however, encompasses a wide variety of artificial and natural fractures in several rock types. Brush (2003) derived a fracture aperture range of 0 to 1×10^{-2} m, with a mean value of 2.5×10^{-3} m, by imaging a 1 m x 1 m x 0.7 m quarried block of granite taken from a large subvertical fracture (Room 209 fracture) located at the 240 m level within the Underground Research Laboratory (URL) in Manitoba. However, the two fracture surfaces were separated and mapped individually and it is possible that effective stress conditions in the field may result in different fracture apertures. Other data for Canadian Shield rocks include those of Yang and Edwards (2000), who computed a fracture aperture of 1.1×10^{-6} m ($=2\delta$) based on fracture zone permeabilities for the Whiteshell Research Area as reported by Davison et al. (1994).

A representative mean fracture aperture of 3.6×10^{-4} m is reported by Hakami and Larsson (1996) for granite from south-eastern Sweden. When investigating the penetration of oxygenated melt waters into fractured crystalline rocks, Glynn et al. (1997) assumed fracture apertures of similar magnitude (1×10^{-4} and 2×10^{-4} m) to those of Hakami and Larsson (1996). Puigdomenech et al. (2001a) used an average fracture aperture approximately one order of magnitude larger (1×10^{-3} m) in their model for oxygen depletion in fractured granite.

For the base case simulation conducted in Stage I, a fracture aperture of 1×10^{-4} m is selected. This value is intermediate, in order of magnitude, to values estimated for Canadian Shield rocks

and is reasonably consistent with the assumed values used in previous investigations of oxygen ingress into crystalline rocks.

A.2 DARCY VELOCITY IN FRACTURE

The Darcy velocity in a fracture depends on the fracture aperture and the hydraulic gradients in the flow system. In this work we do not compute large-scale groundwater flow conditions during interglacial and glacial periods, but rather explicitly assign fracture velocities based on the work of other researchers.

According to a regional-scale groundwater flow study in a Canadian Shield setting, Sykes et al. (2003) computed velocity ranges of 8×10^{-15} to 8×10^{-7} m s^{-1}; however, they did not consider individual fractures in their numerical simulations. Chan and Stanchell (2004) simulated groundwater velocities in fracture zones and rock matrix during glacial loading. The fracture zones down to depths of 400 m were assigned a thickness of 20 m and a permeability of 10^{-13} m^2. With an assumed fracture zone porosity of 0.05, Chan and Stanchell (2004) simulated fracture zone velocities of 3×10^{-7} to 5×10^{-7} m s^{-1} during periods of ice loading, which were several orders of magnitude larger than flow rates during interglacial periods. Chan and Stanchell (2004) attributed these increased velocities to the consolidation effect caused by the load of the ice sheets. These simulations, however, did not consider the possible influence of density contrasts in fluids which are known to exist in the deep Canadian Shield groundwaters (Sykes et al. 2003).

Based on the work of Geier (1996), Glynn et al. (1997) propose that a downward fracture velocity of 1.6×10^{-7} m s^{-1} is not uncommon in fractured crystalline rocks, even under present-day interglacial conditions. In addition, the work of Ittner et al. (1991) suggests that a vertical velocity of 2×10^{-6} m s^{-1} may be representative of present-day flow regimes in fractured crystalline rocks of northern Sweden.

The base case scenario Darcy velocity is chosen to be 3.2×10^{-8} m s^{-1} (i.e. 1 m yr^{-1}) during the interglacial period, and ten times larger (3.2×10^{-7} m s^{-1}) during the glacial melt water production period. These values capture the general range of velocities estimated by Chan and Stanchell (2004).

A.3 LONGITUDINAL DISPERSIVITY

Fracture velocity will vary spatially because fractures do not have smooth walls, vary in aperture, and contain fracture filling minerals. By considering a longitudinal dispersivity in the solute transport equation, such variations in the fracture velocity can be accounted for (e.g., Woodbury 1997). Neretnieks et al. (1982) conducted a laboratory tracer test in a natural fracture in a granite core (diameter 0.2 m and length 0.3 m) obtained from the Stripa mine in Sweden. The longitudinal dispersivity obtained was 0.025 m, and much of the dispersion in solute breakthrough curves was attributed to channeling within the fracture plane. For the simulations conducted in this study, the longitudinal fracture dispersivity is selected as 0.1 m which, because of the relatively large transport distances, is somewhat increased from the value of 0.025 m determined by Neretnieks et al. (1982).

A.4 POROSITY AND PERMEABILITY OF ROCK MATRIX

The study by Vilks et al. (2004) provides detailed information on matrix porosity and matrix permeability at different depths at Atomic Energy of Canada's URL. For granite, Vilks et al. (2004) estimated an average rock matrix porosity of 2.3×10^{-3} (range of 2.05×10^{-3} to 2.79×10^{-3}). They also investigated the effect of fracture alteration on porosity (altered rock in fracture zone: 9.53×10^{-3}, 4.69×10^{-3}, unaltered grey granite: 3.54×10^{-3}, 3.23×10^{-3}, 2.88×10^{-3}, see Table 10, p. 25 in Vilks et al., 2004). A matrix porosity (φ_m) of 5×10^{-3}, which falls within the range determined by Vilks et al. (2004), is selected for the base case scenario.

Table A. 1 presents a comparison of matrix permeability values obtained from in-situ and laboratory testing of the URL rock. Yang and Edwards (2000) also provide bulk rock permeability values for three different layers (Table A. 2; layer 1: pink granite with well-developed vertical fractures, layer 2: transition from well-fractured pink granite to sparsely fractured grey granite, layer 3: sparsely-fractured grey granite). However, these values are of limited applicability for assigning matrix permeabilities because they are lumped values for the matrix and fractures. An isotropic permeability value of 1×10^{-19} m^2 is assumed for a (nearly) unaltered rock matrix in the base case.

Table A. 1: Comparison of matrix permeability values (Vilks et al. 2004, Table 37, p. 136)

URL Level (depth)	In-situ Hydraulic Testing (m^2)			Laboratory Hydraulic Testing (m^2)	
	Ramey Model	nSIGHTS minimum	nSIGHTS bulk rock	Hollow Core	HPRM (High Pressure Radioisotope Migration apparatus)
240 m	5×10^{-21} to 3×10^{-20}	1.1×10^{-20}	3.6×10^{-20}	2.4×10^{-18}	8×10^{-20} to 1×10^{-18}
300 m	1×10^{-21} to 1×10^{-20}	3.6×10^{-21}	5.7×10^{-20}	1.8×10^{-17}	4×10^{-19} to 3×10^{-17}
420 m	2×10^{-21} to 1×10^{-20}	1.8×10^{-21}	5.7×10^{-20}	8.4×10^{-18} to 1.3×10^{-17}	1×10^{-18} to 2×10^{-17}

Table A. 2: Bulk rock permeability values of the 3 layers used by Yang and Edwards (2000), derived from Davison et al. (1994)

Layer	Depth range (m)	Horizontal permeability (m^2)	Vertical permeability (m^2)
1	0 -150	1.0×10^{-15}	5.0×10^{-15}
2	150 – 300	1.0×10^{-17}	5.0×10^{-17}
3	300 – 1000	1.0×10^{-19}	1.0×10^{-19}

A.5 EFFECTIVE DIFFUSION COEFFICIENT OF ROCK MATRIX

Vilks et al. (2004) provide data for effective diffusion coefficients (D_{eff}) in Canadian Shield granite. Table A. 3 compares D_{eff} values from in-situ and laboratory testing for the bulk rock at different levels of the URL. Increased values of D_{eff} for samples from greater depth (Table A. 3) may illustrate the influence of alteration of the stress conditions as a result of in-situ stress relaxation and stresses triggered by drilling (Vilks et al. 2004).

Table A. 3: Comparison of D_{eff} values (Vilks et al. 2004, Tracer: Iodide, Table 36, p. 133)

URL Level (depth)	Laboratory D_{eff} values ($m^2 s^{-1}$)	*In-situ* D_{eff} values ($m^2 s^{-1}$)	
		Range	Geometric mean
240 m	$(3.4 \pm 0.8) \times 10^{-13}$	2.8×10^{-13} to 5.0×10^{-13}	3.7×10^{-13}
300 m	$(1.1 \pm 0.2) \times 10^{-12}$	7.1×10^{-14} to 2.8×10^{-13}	1.4×10^{-13}
420 m	$(1.6 \pm 0.1) \times 10^{-12}$	6.6×10^{-13} to 1.9×10^{-12}	1.1×10^{-12}

Vilks et al. (2004) used the tracer iodide to determine D_{eff} in Table A. 3. The magnitude of the diffusion coefficient for iodide in water is similar to that of dissolved oxygen in water and this can be shown by means of a correlation developed by Wilke and Chang (1955):

$$D_{i-H2O} = 7.4 \times 10^{-8} \frac{T(\psi_{H2O} M_{H2O})^{\frac{1}{2}}}{\mu \, v_{i_i}^{0.6}} \qquad (A.1)$$

where T is the absolute temperature [K], ψ_{H2O} is an "association" parameter for water (2.26, Reid et al. 1977), M_{H2O} is the molecular weight of water (18 g mol^{-1}), μ is the water viscosity [centipoises], and v_i is the molar volume of oxygen or iodide. According to Bird et al. (1960), the diffusion coefficient for iodide and oxygen in the water can be estimated by Eq. (A.1) with an accuracy of ± 10 % (see also Richard 2005), which introduces significantly less uncertainty than associated with the medium properties. Using a molar volume of 25.72 cm^3 g^{-1} mol^{-1} for iodide in Eq. A.1 and assuming a temperature of 20 ^{O}C (293.1 K), and a water viscosity of 1.002 centipoises at 20 ^{O}C (Weast 1969), a diffusion coefficient of 1.971 x 10^{-5} cm^2 s^{-1} is obtained. This compares to a diffusion coefficient for oxygen in water of 1.977 x 10^{-5} cm^2 s^{-1} when using a molar volume of oxygen of 25.6 cm^3 g^{-1} mol^{-1} (Welty et al. 1984).

Consistent with the range of effective diffusion coefficients given by Vilks et al. (2004), a rock matrix D_{eff} value of 5.4 x 10^{-13} m^2 s^{-1} (average of the geometric means: 3.7 x 10^{-13}, 1.4 x 10^{-13}, 1.1 x 10^{-12}, see Table A. 3) is chosen for all solutes.

A.6 TRANSPORT BOUNDARY CONDITIONS

The relevant transport boundary conditions for a reactive transport simulation focusing on interglacial recharge and glacial melt water ingress in a sparsely fractured medium are:

   i)   Dissolved oxygen concentration
   ii)   Dissolved organic carbon (DOC) concentration
   iii)   pH
   iv)   Partial pressure of carbon dioxide (pCO$_2$)
   v)   Cation and anion concentrations.

Oxygen concentration. According to Glynn et al. (1997) and Puigdomenech et al. (2001a), the concentration of dissolved oxygen in recharge water may reach up to 45 mg L^{-1} (1.4 mmol L^{-1}) during periods of glacial melt water production as a result of the elevated pressure below the melting ice. These projections are based on calculations of air content in glacial ice and pressures beneath ice sheets, and do not appear to have been verified to date. In comparison,

fresh water equilibrated with air at a temperature of 23^oC contains approximately 8.6 mg L^{-1} of dissolved O_2 (Benson and Krause 1980). For the base case simulation the dissolved O_2 concentration is assumed to be 8.6 mg L^{-1} during the interglacial period, and approximately 20 mg L^{-1} during the glacial melt water production period.

Dissolved organic carbon (DOC) concentration. During an interglacial period, the DOC concentration in recharge waters may be comparable to present-day DOC concentrations in surface water. Meybeck (1982) determined that natural DOC concentrations in river water were linked to climatic conditions. For example, the wet tropics had a median DOC concentration of 6 mg L^{-1}, while minimum values of less than 1 mg L^{-1} were found in rivers draining mountainous alpine environments (e.g. mountain rivers in the French Alps or New Zealand). Temperate zone rivers had a median concentration of 3 mg L^{-1} (Meybeck 1982). During glacial periods, as already suggested in Section 1, organic carbon in the recharging melt water may be very low because of removal of soil cover by glacial action. For the base case scenario, during the interglacial period a concentration of DOC of 7.14×10^{-5} mol L^{-1} (2.14 mg L^{-1}) is assumed in the recharge water, while DOC is assumed absent from the recharge water during the period of melt water production. These values are believed to be conservative in that little or no DOC is available for oxidation reactions.

pH. Based upon the measurements by Pitkänen et al. (2004), the pH of the melt water is expected to be similar to that of rainwater. A value of 5.8 has been selected for both the interglacial and glacial periods in the base case.

Partial pressure of carbon dioxide (pCO₂). According to Stauffer and Berner (1978), Neftel et al. (1982) and Oeschger and Stauffer (1986), the amount of CO_2 available in ice is not large. About 10 percent air by volume, with the prevailing atmospheric CO_2 concentration, is trapped in ice and retained during the transformation of snow to ice without melting. A total of about 10^{-6} mole CO_2/kg ice can be expected (approximately corresponding to 0.04 mg L^{-1} CO_2 in melt water, or a pCO_2 of $10^{-4.5}$ atm). Rainwater in equilibrium with the atmosphere has an order of magnitude higher pCO_2. Under certain circumstances, if melt water is in contact with atmospheric CO_2, it can attain a pCO_2 near atmospheric equilibrium ($10^{-3.5}$ atm; Kump and Alley 2004). For the base case scenario the pCO_2 of infiltrating water is set to $10^{-3.5}$ atm.

Cation and anion concentration. The concentrations of cations and anions in the recharge water will play a secondary role because reactions in the fracture and matrix will alter aqueous composition shortly after melt water infiltration. Low cation and anion concentrations are typically observed in precipitation in the form of water (Appelo and Postma 2005) or snow, which is the ultimate source of recharge during interglacial periods and periods of glacial melting. As a result, recharge water is typically undersaturated with respect to all minerals present in the fracture and matrix. For the base case, ion concentrations in infiltrating water were derived from a data set provided by Pitkänen et al. (2004) representing an estimated quaternary glacial water.

A.7 MINERAL ABUNDANCES

The reduction capacity of the repository host rock will depend on the presence of reduced species in solid and in dissolved form, and the occurrence of primary and secondary redox reactions that consume oxygen. As the focus of this study is redox stability, the minerals of most interest are those which have reduction capacity, including chlorite, biotite and pyrite.

Chlorite has been identified as an important Fe(II)-bearing mineral phase in fractures in the Canadian Shield (McMurry 2000), although there is uncertainty regarding the abundance of this mineral phase. Gascoyne (2005 pers. comm.) indicates that a range of volume fractions from 0 to 0.6 has been observed as fracture fillings. Very little chlorite has been found in bedrock (0.1 to 0.4%, Everitt et al. 1998, Everitt 2001, Everitt 2004). In the base simulations we assume volume fractions for chlorite in the fracture and matrix of 0.1 and 0, respectively.

The most abundant reducing mineral in the bedrock matrix is biotite with volume percentages of 1.8 to 13.2% (Everitt et al. 1998, Everitt 2001, Everitt 2004). This large range can be attributed to the distinct textural rock varieties in the Canadian Shield. The grey granite, for instance, which is classified as medium-grained and relatively homogeneous by Vilks et al. (2004), contains up to 10 % biotite and magnetite. According to Everitt et al. (1998) and Everitt (2001, 2004), the three distinct textural varieties of the Lac Du Bonnet granite, fine (FG), medium (MG) and coarse grained (CG) granites, have average volume percentages of 3.8, 6.9 and 10.4% biotite, respectively. An intermediate value for biotite volume fraction (5%) in the matrix of the reducing zone is used in the base case simulations.

Pyrite has been observed in minute amounts in the main phase granite and in significant amounts in some xenoliths. For the Lac du Bonnet granite, Kamineni et al. (1984) and Gascoyne (2004) report up to 0.1% pyrite and magnetite. However, at the 130 m Level at the URL, room-size xenoliths containing up to 30% pyrite have been found (Everitt et al. 1998, Everitt 2001, Everitt 2004). For comparison, at the Äspö site in Sweden, Tirén et al. (1996) and Glynn et al. (1997) report only relatively small amounts of pyrite in hydraulically conductive and connected fractures. To be somewhat conservative with regard to O_2 buffering, the base case simulations assume only a small volume fraction of 10^{-6} for pyrite in the matrix of the reducing zone.

Other minerals are present in the fractures and matrix; however, with the exception of quartz, these phases are neglected in the present simulations, and are therefore not discussed here. For quartz, a range of volume fractions from 2.3×10^{-1} to 3.4×10^{-1} has been observed in Canadian Shield rocks (Everitt et al. 1998, Everitt 2001, Everitt 2004). A value of 3×10^{-1} is therefore applied for all simulations.

A.8 GEOCHEMICAL REACTIONS AND RATES

Types of geochemical reactions. According to Guimerà et al. (1999), chlorite can be represented by a ferrous (daphnite, $Fe_5Al_2Si_3(OH)_8$) or a magnesian (clinochlore, $Mg_5Al_2Si_3(OH)_8$) end-member and biotite can be represented by the annite ($KFe_3AlSi_3O_{10}(OH)_2$) and phlogopite (Fe-Mg-biotite, e.g.: $KMg_2FeAlSi_3O_{10}(OH)_2$) end-members. Chlorite also exists in the form of a mixed Fe-Mg-chlorite phase ($Mg_2Fe_3Al_2Si_3O_{10}(OH)_8$, Malmström et al. 1995, McMurry 2000). The main focus of this work was on considering a representative Fe(II)-content within these mineral phases and the bulk rock. The composition of Fe-Mg-biotite and Fe-Mg-chlorite are based on mineralogical analyses of rock samples from the Canadian Shield (Kamineni et al. 1984, McMurry and Ejeckam 2002, Cavé and Al 2005). For these conditions, Fe-Mg-biotite and Fe-Mg-chlorite dissolution may be described as follows (Malmström et al. 1995, McMurry 2000):

Dissolution of Fe-Mg-biotite:

$$K(Mg_2Fe)(Si_3Al)(O_{10})(OH_2) + 10H^+ \rightarrow K^+ + 2Mg^{2+} + Fe^{2+} + 3H_4SiO_4 + Al^{3+} \qquad (A.2)$$

Dissolution of Fe-Mg-chlorite:

$$Mg_2Fe_3Al_2Si_3O_{10}(OH)_8 + 16H^+ \rightarrow 2Mg^{2+} + 3Fe^{2+} + 2Al^{3+} + 3H_4SiO_4 + 6H_2O \qquad (A.3)$$
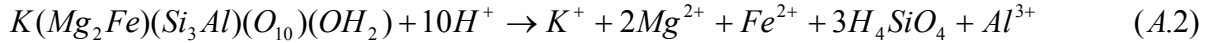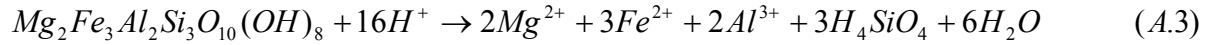
The ferrous iron produced from these reactions may rapidly form iron-oxyhydroxide precipitates. For example:

$$Fe^{2+} + \tfrac{1}{4}O_2 + \tfrac{5}{2}H_2O \rightarrow Fe(OH)_3(s) + 2H^+ \qquad (A.4)$$
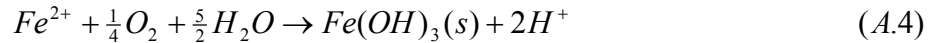
Ferrihydrite ($Fe(OH)_3$) eventually transforms to a more stable iron-oxyhydroxide which is usually goethite (FeOOH). Considering the long time scales considered for the performance of a waste repository, goethite is considered to be a more representative iron-oxyhydroxide phase.

Precipitation of goethite:

$$Fe^{2+} + \tfrac{1}{4}O_2 + \tfrac{3}{2}H_2O \rightarrow FeOOH + 2H^+ \qquad (A.5)$$
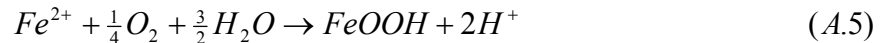
Alternatively, because the oxidation of aqueous Fe(II) in the presence of O_2 and the precipitation of Fe(III)-hydroxides is rapid in comparison to silicate dissolution, the dissolution of iron-containing aluminosilicate minerals, oxidation of Fe(II), and precipitation of iron-hydroxides may be expressed as an overall reaction:

Oxidative dissolution of Fe-Mg biotite:

$$K(Mg_2Fe)(Si_3Al)(O_{10})(OH_2) + \tfrac{1}{4}O_2 + 8H^+ + \tfrac{3}{2}H_2O$$
$$\rightarrow FeOOH + K^+ + 2Mg^{2+} + 3H_4SiO_4 + Al^{3+} \qquad (A.6)$$

Oxidative dissolution of Fe-Mg chlorite:

$$Mg_2Fe_3Al_2Si_3O_{10}(OH)_8 + \tfrac{3}{4}O_2 + 10H^+$$
$$\rightarrow 3FeOOH + 2Mg^{2+} + 2Al^{3+} + 3H_4SiO_4 + \tfrac{3}{2}H_2O \qquad (A.7)$$
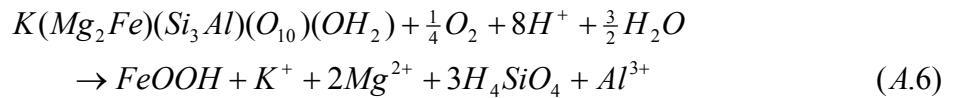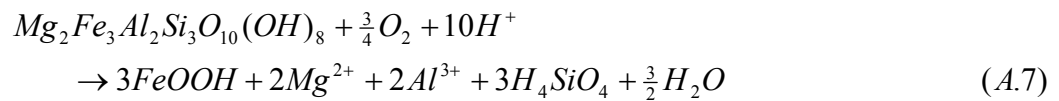
Products of aqueous aluminium and silicon may include $Al(OH)_3$(am), SiO_2(am) and gibbsite.

Precipitation of $Al(OH)_3$(am):
$$Al^{3+} + 3H_2O \rightarrow Al(OH)_3(am) + 3H^+ \qquad (A.8)$$

Precipitaton of SiO_2(am):
$$H_4SiO_4 \rightarrow SiO_2(am) + 2H_2O \qquad (A.9)$$
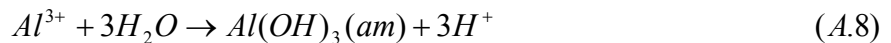
Precipitation of gibbsite:
$$Al^{3+} + 3H_2O \rightarrow Al(OH)_3(c) + 3H^+ \qquad (A.10)$$
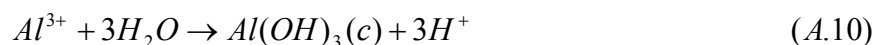
In these cases, Al(OH)$_3$(am), SiO$_2$(am) and gibbsite should be viewed as a surrogates for the complex assemblage of clay minerals that precipitate during the weathering process.

An additional O$_2$-consuming reaction is the dissolution of sulphide minerals such as pyrite (FeS$_2$):

$$FeS_2 + \tfrac{15}{4}O_2 + \tfrac{5}{2}H_2O \rightarrow FeOOH + 2SO_4^{2-} + 4H^+ \qquad (A.11)$$
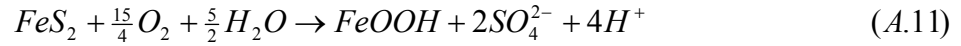
If pyrite oxidation is significant and calcium is present in solution, gypsum may precipitate from the pore water:

$$Ca^{2+} + SO_4^{2-} + 2H_2O \rightarrow CaSO_4 \cdot 2H_2O \qquad (A.12)$$
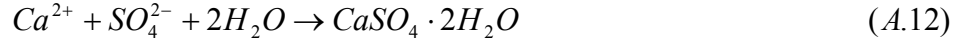
During interglacial periods, oxygenated recharge waters may also contain dissolved organic carbon that is leached from the soil horizon. Aerobic respiration of DOC (e.g. CH$_2$O) may lead to the consumption of dissolved oxygen and the production of CO$_2$:

$$CH_2O + O_2 \rightarrow CO_2 + H_2O \qquad (A.13)$$

Moreover, anaerobic degradation of CH$_2$O by Fe(III)-containing mineral phases and SO$_4$ may take place, which leads to additional consumption of organic carbon, if oxygen is depleted:

$$CH_2O + 4FeOOH + 8H^+ \rightarrow 4Fe^{2+} + CO_2 + 7H_2O \qquad (A.14)$$
$$CH_2O + \tfrac{1}{2}SO_4^{2-} + H^+ \rightarrow \tfrac{1}{2}H_2S + CO_2 + H_2O \qquad (A.15)$$
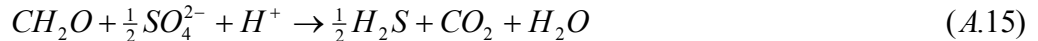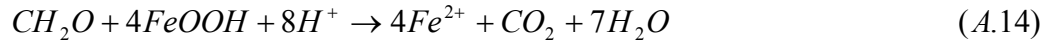
In contrast, the recharge water during periods of glacial ice cover may contain little or no organic carbon as discussed in Section 1.

Because the focus of the current modelling is the description of redox conditions, reactions for other mineral phases that may occur in fractured granitic rock, for example the weathering of plagioclase feldspars that may result in the formation of carbonate mineral phases (Gascoyne 2004), have not been included. This implies that the model results for selected parameters such as pH, should not be given great emphasis.

Rates of geochemical reactions. Several recent studies have investigated the dissolution kinetics of biotite in laboratory experiments and many of these studies are summarized and compared by White and Brantley (2003) and Samson et al. (2005). In these two studies, for differing weathering environments, pH, and grain sizes, a range of $10^{-16.5}$ to $10^{-10.7}$ mol m^{-2} s^{-1} has been reported for biotite dissolution. Most reported values in the literature for biotite fall in the range of 5.6 x 10^{-13} to 6.5 x 10^{-12} mol m^{-2} s^{-1} in the pH range of 5 to 14. The log rate of approximately -12.25 selected in the base case is close to the lower limit of the laboratory rates for *fresh* rock/mineral samples (Samson et al. 2005, Figure 10; White and Brantley 2003, Figure 9). Ganor et al. (2005) have shown that the dissolution rates for biotite from a bulk granite are comparable (within a factor of 2.5) to rates obtained from mineral-rich fractions separated from a granite sample. Relatively little information is available on the dissolution rates of chlorite; Mg-rich chlorite rates may be comparable to those for biotite, while Fe-rich chlorite may be 2 to 3 orders of magnitude faster (Murphy et al. 1998). For pyrite, a rate expression of r = $10^{-8.19}$ [O$_2$]$^{0.5}$[H$^+$]$^{-0.11}$ mol m^{-2} s^{-1} has been derived by Williamson and Rimstidt

(1994) through re-interpretation of a range of literature data. Appendix B.1 provides a brief discussion of laboratory versus field derived rates.

Mineral dissolution rates are typically normalised with respect to reactive mineral surface areas and expressed in units of mol m^{-2} mineral s^{-1}. Thus, to obtain an effective rate for a specific site, these must be multiplied by a representative surface area. White and Brantley (2003) give a range of 0.84 to 8.1 m^2 g^{-1} for the surface area of biotite as measured by gas absorption (i.e., by the Brunauer-Emmett-Teller (BET) methods, Brunauer et al. 1938). This range of surface areas was obtained from biotite samples with significant variations in grain size (ranging from 10 to 1200 μm). In comparison, the mineral grain size in granite can vary between 1 and 5 mm (Vilks et al. 2004). Malmström et al. (1996) have provided a surface area estimate of 10 m^2 L^{-1} for biotite in a fracture zone at Äspö.

The oxidation of natural DOC in the aqueous phase is commonly represented by Monod kinetic expressions (e.g. Lensing et al. 1994, Park and Jaffe 1996). Reaction rates for aerobic DOC degradation reported in the literature for aquifers and marine sediments are typically larger than 10^{-10} mol L^{-1} s^{-1} (e.g. Matsunaga et al. 1993, Mayer et al. 2001, Prommer and Stuyfzand 2005). A conservative value of 1.5 x 10^{-10} mol L^{-1} s^{-1} was assumed for the present simulations.

A.9 REFERENCES

Appelo, C. A. J., and D. Postma. 2005. Geochemistry, Groundwater and Pollution, 2nd Edition. A. A. Balkema, Leiden, The Netherlands.

Benson, B.B., and D. Krause. 1980. The concentration and isotopic fractionation of gases dissolved in freshwater in equilibrium with the atmosphere, 1. Oxygen. Limnol. Oceanogr. 25: 662-671.

Bird, R.B., W.E. Stewart, and E.N. Lightfoot. 1960. Transport Phenomena. John Wiley & Sons. NY. 780 pp.

Brunauer, S., P.H. Emmett and E. Teller. 1938. Adsorption of gases in multimolecular layers. J. Am. Chem. Soc. 60: 309-319.

Brush, D.J. 2001. Three-dimensional fluid flow and solute transport in rough-walled fractures. Ph.D. thesis, University of Waterloo, Waterloo, Ontario.

Brush, D.J. 2003. Quarried block experiment: Numerical simulations of flow and transport experiments in a natural fracture. Ontario Power Generation, Nuclear Waste Management, Report No: 06819-REP-01300-10075-R00.

Cavé, L.C. and T.A. Al. 2005. Paleohydrogeology - development of analytical TEM methods for paleoredox investigations. Ontario Power Generation, Report No. 06819-REP-01300-10099-R00.

Chan, T., and F.W. Stanchell. 2004. Decovalex III BMT3 (the glaciation bench mark test) final research team report. Ontario Power Generation, Nuclear Waste Management, Report No: 06819-REP-01300-10091-R00.

Davison, C.C., T. Chan, and A. Brown. 1994. The disposal of Canada's nuclear fuel waste: The geosphere model for postclosure assessment. Atomic Energy of Canada Limited (AECL) Research, AECL-10719.

Everitt, R.A., A. Brown, R. Ejeckam, R. Sikorsky, and D. Woodcock. 1998. Litho-structural layering within the Archean Lac du Bonnet Batholith, at AECL's Underground Research Laboratory, Southeastern Manitoba. Journal of Structural Geology. 20(9/10): 1291-1304.

Everitt, R.A. 2001. The influence of rock fabric on excavation damage in the Lac Du Bonnet Granite. Ph.D. thesis, University of Manitoba, Winnipeg, Manitoba.

Everitt, R.A. 2004. Personal communication.

Ganor, J., E. Roueff, Y. Erel and J.D. Blum. 2005. The dissolution kinetics of a granite and its minerals—Implications for comparison between laboratory and field dissolution rates. Geochimica et Cosmochimica Acta. 69(3): 607-621.

Gascoyne, M. 2004. Hydrogeochemistry, groundwater ages and sources of salts in a granitic batholith on the Canadian Shield, southeastern Manitoba. Applied Geochemistry. 19: 519–560.

Gascoyne, M. 2005. Personal communication.

Geier, J., 1996. Discrete-feature modelling of the Äspö site: 3. Predictions of hydrogeological parameters for performance assessment. Swedish Nuclear Power Inspectorate, SKI Report 96: 7, 211 p.

Glynn, P.D., C.I. Voss, and A.M. Provost. 1997. Deep penetration of oxygenated meltwaters from warm based ice sheets into the Fennoscandian Shield, In: Use of Hydrogeochemical Information in Testing Groundwater Flow Models, Workshop Proceedings. Borgholm. Sweden. pp. 201-241.

Guimerà J., L. Duro, S. Jordana, and J. Bruno. 1999. Effects of ice melting and redox front migration in fractured rocks of low permeability. Svensk Kärnbränslehantering AB. Report no. TR-99-19.

Hakami, E., and E. Larsson. 1996. Aperture measurement and flow experiments on a single natural fracture. Int. J. Rock Mech. Min. Sci. & Geomech. Abstr. 33(4): 395-404.

Ittner, T., E. Gustafsson, and R. Nordqvist. 1991. Radionuclide content in surface and groundwater transformed into breakthrough curves. A Chernobyl fallout study in a forested area in Northern Sweden: SKB Technical Report 91-28, 16 p.

Kamineni, D.C., J.J.B. Dugal, and R.B. Ejeckam. 1984. Geochemical investigations of granitic core samples from boreholes at the Underground Research Laboratory site near Lac du Bonnet, Manitoba. Atomic Energy of Canada Limited Technical Record, TR-221.

Kump, L.R., and R.B. Alley, 1994. Global chemical weathering on glacial time scales. Chapter 3 in Studies in Geophysics - Material Fluxes on the Surface of the Earth, Board on Earth Sciences and Resources, Commission on Geosciences, Environment, and Resources (CGER), National Research Council, National Academy Press, Washington, D.C., http://darwin.nap.edu/books/0309047455/html/46.html.

Lensing, H.J., M. Vogt, and B. Herrling. 1994. Modeling of biologically mediated redox processes in the subsurface. J. Hydrology. 159: 125-143.

MacQuarrie, K.T.B., and K.U. Mayer. 2003. Reactive transport modelling in fractured rock: State-of-science review. Ontario Power Generation, Nuclear Waste Management, Report No: 06819-REP-01200-10117-R00.

Malmström, M., S. Banwart, L. Duro, P. Wersin, and J. Bruno. 1995. Biotite and chlorite weathering at 25°C. Swedish Nuclear Fuel and Waste Management Company Technical Report, SKB-TR-95-01.

Malmström, M., S. Banwart, J. Lewenhagen, L. Duro, and J. Bruno. 1996. The dissolution of biotite and chlorite at 25°C in the near-neutral pH region. Journal of Contaminant Hydrology. 21: 201-213.

Matsunaga, T., G. Karametaxas, H.R. Von Gunten, and P.C. Lichtner. 1993. Redox chemistry of iron and manganese minerals in river-recharged aquifers: A model interpretation of a column experiment. Geochimica et Cosmochimica Acta. 57: 1691-1704.

Mayer, K.U., D.W. Blowes, and E.O. Frind. 2001. Reactive transport modeling of an in situ reactive barrier for the treatment of hexavalent chromium and trichloroethylene in groundwater. Water Resources Research. 37(12): 3091-3103.

McMurry, J. 2000. Evaluating effects of deep recharge by a low-salinity, oxidizing groundwater: a geochemical modelling case study. Ontario Power Generation Report No. 06819-REP-01300-10007 R00.

McMurry, J., and R.B. Ejeckam. 2002. Paleohydrogeological study of fracture mineralogy in the Whiteshell Research Area. Ontario Power Generation Report No. 06819-REP-01200-10082-R00.

Meybeck, M. 1982. Carbon, nitrogen and phosphorus transport by world rivers. American Journal of Science. 282: 401-450.

Murphy, S. F., S. L. Brantley, A. E. Blum, A. F. White and H. Dong. 1998. Chemical weathering in a tropical watershed, Luquillo Mountains, Puerto Rico: II. Rate and mechanism of biotite weathering. Geochimica et Cosmochimica Acta. 62(2): 227-243.

Neftel, A., H. Oeschger, J. Schwander, B. Stauffer, and R. Zumbrunn. 1982. Ice core sample measurements give atmospheric CO_2 content during the last 40,000 yr. Nature. 295: 220-223.

Neretnieks, I., T. Eriksen, and P. Tähtinen. 1982. Tracer movement in a single fissure in granitic rock: Some experimental results and their interpretation. Water Resources Research. 18(4): 849-858.

Oeschger, H., and B. Stauffer. 1986. Review of the history of atmospheric CO_2 recorded in ice cores, in The Changing Carbon Cycle: A Global Analysis, J.R. Trabalka and D.E. Reichle, eds., Springer-Verlag, New York, pp. 89-108.

Park, S.S. and P.R. Jaffe. 1996. Development of a sediment redox potential model for the assessment of postdepositional metal mobility. Ecological Modelling. 91: 169-181.

Pitkänen, P., S. Partamies, and A. Luukkonen. 2004. Hydrogeochemical interpretation of baseline groundwater conditions at the Olkiluoto site. POSIVA Report No. 2003-07. http://www.posiva.fi/raportit/Posiva_2003-07.pdf.

Prommer, H., and P.J. Stuyfzand. 2005. Identification of temperature-dependent water quality changes during a deep well injection experiment in a pyritic aquifer. Environmental Science & Technology. 39: 200-2209.

Puigdomenech, I., J-P. Ambrosi, L. Eisenlohr, J-E. Lartigue, S. A. Banwart, K. Bateman, A.E. Milodowski, J.M. West, L. Griffault, E. Gustafsson, K. Hama, H. Yoshida, S. Kotelnikova, K. Pedersen, V. Michaud, L. Trotignon, J. Rivas Perez, and E-L Tullborg. 2001a. O_2 depletion in granitic media – the REX project. Svensk Kärnbränslehantering AB. Report no. TR-01-05.

Reid, R.C., J.M. Praunsnitz, and T.K. Sherwood. 1977. The Properties of Gases and Liquids, Third Edition. McGraw-Hill. NY. p. 578.

Richard, T. 2005. Calculating the oxygen diffusion coefficient in water. http://compost.css.cornell.edu/oxygen/oxygen.diff.water.html#txt4, Dept. of Ag. and Biological Engineering, Pennsylvania State University.

Samson, S.D., K.L. Nagy, and W.B. Cotton. 2005. Transient and quasi-steady-state dissolution of biotite at 22–25°C in high pH, sodium, nitrate, and aluminate solutions. Geochimica et Cosmochimica Acta. 69(2): 399– 413.

Stauffer, B., and W. Berner. 1978. CO_2 in natural ice. Journal of Glaciology. 21: 291-299 (with discussion, p. 300).

Steefel, C.I., and P.C. Lichtner. 1998a. Multicomponent reactive transport in discrete fractures: I. Controls on reaction front geometry. J. Hydrology. 209:186-199.

Sykes, J.F., S.D. Normani, and E.A. Sudicky. 2003. Regional scale groundwater flow in a Canadian Shield setting. Ontario Power Generation, Nuclear Waste Management, Report No: 06819-REP-01200-10114-R00.

Tirén, S., M. Beckholmen, C. Voss, and P. Askling. 1996. Development of a geological and structural model of Äspö, southeastern Sweden (SITE-94), SKI Report 96:16, Swedish Nuclear Power Inspectorate, Stockholm.

Vilks, P., N.H. Miller, and F.W. Stanchell. 2004. Phase II in-situ diffusion experiment. Ontario Power Generation, Nuclear Waste Management, Report No: 06819-REP-01200-10128-R00.

Weast, R.C. (ed.) 1969. CRC Handbook of Chemistry and Physics, 50th Edition. p F-36.

Welty, J.R., C.E. Wicks, and R.E. Wilson. 1984. Fundamentals of Momentum, Heat, and Mass Transfer, Third Edition. John Wiley & Sons, NY. 803 pp.

White, A.F., and S.L. Brantley. 2003. The effect of time on the weathering of silicate minerals: why do weathering rates differ in the laboratory and field? Chemical Geology. 202: 479-506.

Wilke, C.R., and P. Chang. 1955. Correlation of diffusion coefficients in dilute solutions. AIChE Journal. 1(2): 264-270.

Williamson, M.A., and J. D. Rimstidt, 1994. The kinetics and electrochemical rate-determining step of aqueous pyrite oxidation, Geochim. Cosmochim. Acta. 58: 5443-5454.

Woodbury, A. 1997. A probabilistic fracture transport model: Application to contaminant transport in a fractured clay deposit. Can. Geotechnical J. 34: 784-798.

Yang, J., and R.N. Edwards. 2000. Predicted groundwater circulation in fractured and unfractured anisotropic porous media driven by nuclear fuel waste heat generation. Can. J. Earth Sci. 37: 1301-1308.

APPENDIX B   DERIVATION OF MINERAL REACTION RATES

CONTENTS

This appendix supplies additional information on laboratory-derived reaction rates and mineral reactive surface areas, as well as additional information on calculation of the effective biotite reaction rate in the rock matrix.

B.1 LABORATORY RATES AND MINERAL REACTIVE SURFACE AREA

Laboratory-derived rates. According to White and Brantley (2003), laboratory-derived rates are commonly two to four orders of magnitude faster than field-derived rates. Generally, reaction rates depend on intrinsic and extrinsic weathering properties. Intrinsic weathering properties include surface area and grain size while extrinsic weathering properties include the effects of specific species (such as: H^+, Al, background electrolytes, and organic acids), type of limitation (surface or transport limited), hydrologic heterogeneity, i.e., inhomogeneities in estimated flow paths (presence of macropores, cracks, etc.), errors in estimation of appropriate field parameters, temperature differences, and biological factors (Murphy et al. 1998, White and Brantley 2003). Time also plays an important role in the determination of reaction rates. Rates obtained from a laboratory experiment are determined fairly quickly (on the order of days) while rates from the field can reflect time scales over thousands of years (White and Brantley 2003).

The overall biotite reaction rate may be further decreased by the build-up of vermiculite, which results from the incongruent dissolution of biotite. According to Samson et al. (2005), "conversion of biotite to vermiculite is a rapid and general occurrence during weathering"; their observations confirmed that the presence of vermiculite decreased the overall dissolution rate of biotite. Therefore, Samson et al. (2005) argue that the use of rates for pure unaltered biotite would represent surficial weathering conditions and may not be useful for reactive-transport modelling of natural processes.

Mineral reactive surface area. The accessible reactive surface area in natural porous media is difficult to estimate (Steefel and Lichtner 1998b, White and Brantley 2003). Surface area is controlled by many factors such as surface roughness, structural defects and dislocations, surface leached layers (coatings), secondary mineral precipitates and sorbed organic compounds (White and Brantley 2003). A literature survey of surface area data from numerous studies, including laboratory and long-term field weathering investigations can be found in Tables 4 to 7 in White and Brantley (2003) for plagioclase, K-feldspar, hornblende and biotite, respectively. Many of these values for surface area are obtained via the Brunauer-Emmett-Teller (BET) methods (Brunauer et al. 1938). BET measurements are usually two orders of magnitude higher than those measured with geometric methods (White and Peterson 1990). Murphy et al. (1998) argue that this is probably due to surface roughness related to etch pits (Banfield and Eggleton 1988), surface steps (Swoboda-Colberg and Drever 1993), and interlayer surface area (Kalinowski and Schweda 1996).

Relatively few attempts have been made to assess the *in situ* microporous matrix of granitic rocks. Schild et al. (2001) conducted an *in situ* experiment at the Grimsel Test Site (Central Swiss Alps) in which an acrylic resin doped with fluorescent agents was injected into the granitic matrix adjacent to a shear zone. The objective of the experiment was to determine the interconnected matrix porosity and microfracture distribution. The results of this experiment demonstrated that even though the rock had a very low interconnected porosity (0.4 to 0.5% by volume), interconnected networks of microfractures were accessible to fluids and occurred throughout the rock volume. Also, microfractures were observed to occur within, and connect, all important mineral groups groups (i.e. biotite, quartz, and K-feldspars). These results and images of fluorescene in the microfracture network of a granite sample presented by Alonso et

al. (2003), suggest that mineral surfaces contained within granite matrix rocks are hydrologically accessible to pore fluids.

B.2 BIOTITE REACTION RATES

Base case. The intrinsic reaction rate selected for biotite (5.6×10^{-13} mol m^{-2} s^{-1}) falls near the lower limit (approximately -12.25 for log rate) for the pH range of 5 to 9 in Figure 10 in Samson et al. (2005). For the conversion of the BET surface (m^2 g^{-1}) to m^2 L^{-1} bulk, a specific gravity for silicate phases of 2.65 g cm^{-3}, and a matrix porosity (φ_m) of 5×10^{-3} are employed (i.e., 1 m^2 g^{-1} x 2.65 g cm^{-3} x 1000 cm^3 L^{-1} x (1-φ_m) = 2637 m^2 L^{-1} bulk). If the resulting BET surface area of 2637 m^2 L^{-1} bulk is divided by 2,000 and multiplied by a biotite volume fraction of 5.0×10^{-2}, a value of 0.066 m^2 L^{-1} bulk for reactive surface area for the base case is obtained. Multiplication of this value by the intrinsic rate for biotite of 5.6×10^{-13} mol m^{-2} s^{-1} yields an effective biotite rate of 3.7×10^{-14} mol biotite L^{-1} bulk s^{-1}.

An alternative approach for estimating the reactive surface area is to use information from microfracture studies in granitic rocks. Assuming parallel planar microfractures with a spacing of 0.2 mm, which appears to be a reasonable spacing based on hydrologically-accessible microfracture images presented by Schild et al. (2001) and Alonso et al. (2003), and an aperture of 1×10^{-6} m, we obtain a matrix porosity of 5×10^{-3}. This porosity is consistent with the matrix porosity values of Vilks et al. 2004. These microfracture parameters yield a microfracture surface area to bulk rock volume ratio of approximately 10,000 m^2/m^3. If it is assumed that the exposed surface area of an individual mineral can be approximated by the volume fraction of that mineral in the rock, then a reactive surface area for biotite in the rock matrix (due to microfractures) is computed to be 0.5 m^2 L^{-1} bulk. This value is about an order of magnitude larger than the value (0.066 m^2 L^{-1} bulk) obtained previously using the BET area and an inaccessibility factor of 2,000. Thus the base case value of 0.066 m^2 L^{-1} bulk appears to be conservative with respect to the process of oxygen consumption within the rock matrix.

Uncertainty analysis. The biotite reaction rates for the uncertainty analysis (Table 4-1 and Table 4-2) are normalised with respect to $f_{bio\text{-}matrix}$ to produce a factor of 2 difference (uncertainty analysis 1) and a one order of magnitude difference (uncertainty analysis 2) between the normalised minimum and maximum biotite rates and the base case value. This implies the same intrinsic reaction rate for biotite of 5.6×10^{-13} mol m^{-2} s^{-1} and the same BET surface area of 1 m^2 g^{-1} (= 2637 m^2 L^{-1} bulk), but reduction factors to field rates of 4,000 (20,000) and 1,000 (200) for the minimum and maximum value, respectively.

B.3 REFERENCES

Alonso, U., T. Missana, A. Patelli, V. Rigato and P. Rivas. 2003. Study of the contaminant transport into granite microfractures using nuclear ion beam techniques. J. Contaminant Hydrology. 61(1-4): 95-105.

Banfield, J.F., and R.A. Eggleton. 1988. Transmission electron microscope study of biotite weathering. Clays Clay Mineral. 36: 47-60.

Brunauer, S., P.H. Emmett, and E. Teller. 1938. Adsorption of gases in multimolecular layers. J. Am. Chem. Soc. 60: 309-319.

Kalinowski, B.E., and P. Schweda. 1996. Kinetics of muscovite, phlogopite, and biotite dissolution and alteration at pH 1-4, room temperature. Geochim. Cosmochim. Acta. 60: 367-387.

Murphy, S. F., S. L. Brantley, A. E. Blum, A. F. White, and H. Dong. 1998. Chemical weathering in a tropical watershed, Luquillo Mountains, Puerto Rico: II. Rate and mechanism of biotite weathering. Geochimica et Cosmochimica Acta. 62(2): 227-243.

Samson, S.D., K.L. Nagy, and W.B. Cotton. 2005. Transient and quasi-steady-state dissolution of biotite at 22–25°C in high pH, sodium, nitrate, and aluminate solutions. Geochimica et Cosmochimica Acta. 69(2): 399-413.

Schild, M., S. Siegesmund, A. Vollbrecht and M. Mazurek. 2001. Characterization of granite matrix porosity and pore-space geometry by *in situ* and laboratory methods. Geophysical J. International. 146: 111-125.

Steefel, C. I., and P. C. Lichtner. 1998b. Multicomponent reactive transport in discrete fractures: II. Infiltration of hyperalkaline groundwater at Maqarin, Jordan, a natural analogue site. J. Hydrology. 209: 200-224.

Swoboda-Colberg, N.G., and J.I. Drever. 1993. Mineral dissolution rates in plot-scale field and laboratory experiments. Chem. Geol. 105: 51-69.

Vilks, P., N.H. Miller, and F.W. Stanchell. 2004. Phase II in-situ diffusion experiment. Ontario Power Generation, Nuclear Waste Management, Report No: 06819-REP-01200-10128-R00.

White, A.F., and S.L. Brantley. 2003. The effect of time on the weathering of silicate minerals: why do weathering rates differ in the laboratory and field? Chemical Geology. 202: 479-506.

White, A.F., and M.L. Peterson. 1990. Role of reactive-surface area characterization in geochemical kinetic models, In Chemical Modeling of Aqueous Systems II, edited by D.C. Melchior, and R.L. Bassett, Chapter 35: 461-475. Washington, D.C., American Chemical Society.

APPENDIX C   ADDITIONAL RESULTS FROM THE STAGE I BASE CASE SIMULATION

CONTENTS

LIST OF FIGURES

C.1 DISTRIBUTION OF IRON-CONTAINING MINERAL PHASES

Figure C. 1: Biotite distribution in the first matrix column adjacent to the fracture.

Figure C. 2: Pyrite distribution in the first matrix column adjacent to the fracture.

Figure C. 3: Goethite distribution in the fracture.

C.2 SUPPLEMENTARY INFORMATION ON GEOCHEMICAL EVOLUTION

The pH range (6 to11, Figure C. 4) determined from the base case simulation is larger than field-observed conditions (pH range of 6.4 to 9.2; Gascoyne, 2004) and this may be a result of a) the changing boundary conditions, b) the exclusion of carbonate minerals which might buffer pH, and c) the incomplete description of silicate weathering reactions. A number of simulations including carbonate and additional silicate minerals was conducted to further investigate the pH results; however, these simulation results were not significantly different from the base case and the increase in model complexity was not warranted. It should be noted; however, that the current simulation results are consistent with previous geochemical mixing calculations involving melt water, groundwater, and water-rock interaction (pH range of 7.2 to 10.5, McMurry 2000).

The simulation results suggest that $Al(OH)_3$(am) dissolves to depths of less than 1 m in the fracture in response to equilibration with the recharge water, precipitates further down the fracture as pH increases, and then dissolves again at the base of the oxidized zone as pH increases further (85 to 100 m, Figure C. 5). Somewhat unexpectedly, there is no precipitation of $Al(OH)_3$(am) predicted due to the dissolution of chlorite and biotite in the reducing zone. However, this behaviour can be explained by the high simulated pH values in this zone (Figure C. 4). Despite the release of sulfate from pyrite oxidation, the solubility of gypsum is not reached (not shown) and therefore precipitation of this phase is not predicted. Because saturation with respect to SiO_2(am) is not reached (SI range of -2.0 to -0.3, Figure C. 6), this phase is also not predicted to precipitate in the fracture. Quartz dissolution in the matrix is insignificant (Figure C. 7) and although quartz is oversaturated in the matrix below a depth of 100 m (SI range of -0.75 to 1.0, Figure C. 8), precipitation of this phase is improbable at groundwater temperatures because of the complex atomic structure of quartz and lack of structural water molecules.
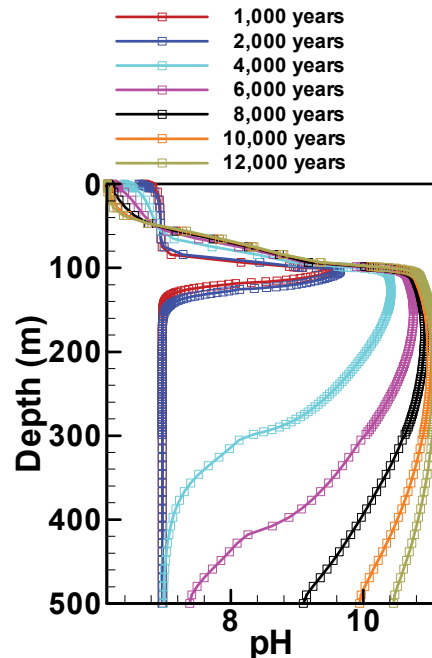
Figure C. 4: pH distribution in the fracture.
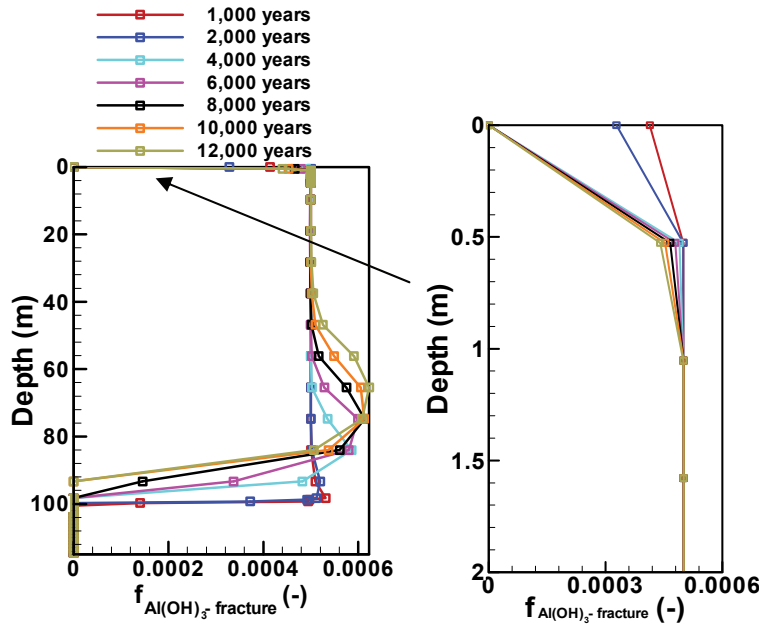
Figure C. 5: Al(OH)₃(am) distribution in the fracture. Right-hand figure shows an enlarged view of the upper 2 metres.
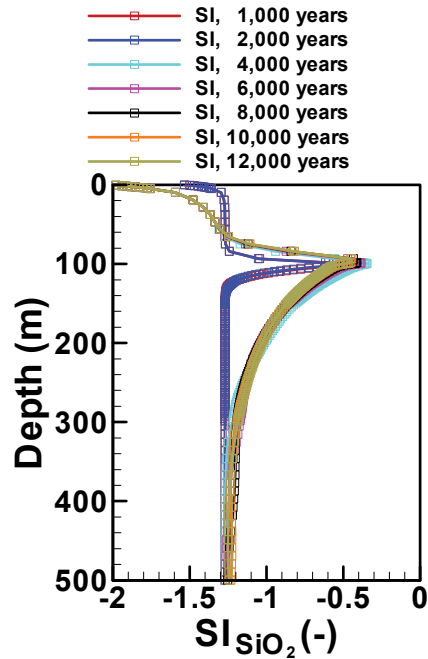
Figure C. 6: Saturation Index (SI) of SiO₂(am) in the fracture.
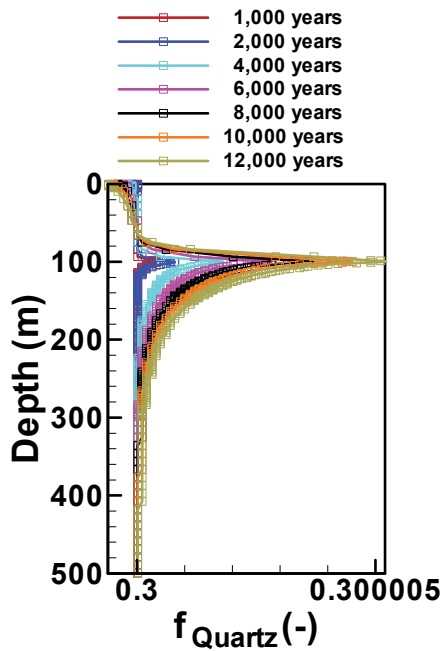
Figure C. 7: Quartz distribution in the first matrix column.
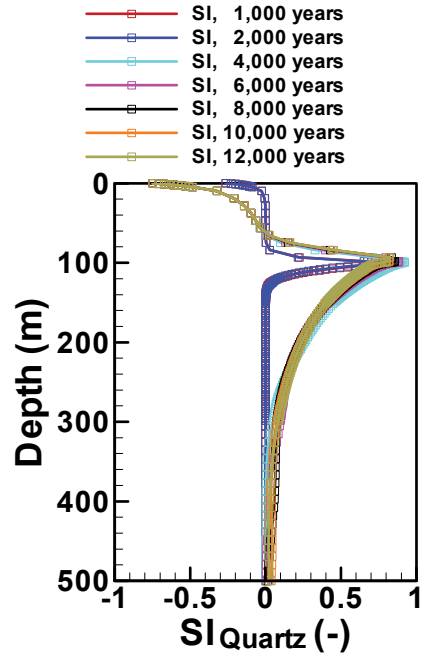
Figure C. 8: Saturation Index (SI) of quartz in the first matrix column.

C.3 REFERENCES

Gascoyne, M. 2004. Hydrogeochemistry, groundwater ages and sources of salts in a granitic batholith on the Canadian Shield, southeastern Manitoba. Applied Geochemistry. 19: 519-560.

McMurry, J. 2000. Evaluating effects of deep recharge by a low-salinity, oxidizing groundwater: a geochemical modelling case study. Ontario Power Generation Report No. 06819-REP-01300-10007 R00.

APPENDIX D   MODEL DOMAIN AND GRID DISCRETIZATION ISSUES

CONTENTS

LIST OF TABLES

LIST OF FIGURES

D.1 EFFECT OF MATRIX DOMAIN WIDTH

To examine whether the assumption of a 3 m wide matrix had a significant effect on the results for the base case, the simulation was repeated with a larger domain width of 50 m. Figure D. 1 indicates that there is diffusive loss of O_2 into the oxidised zone that extends beyond 3 m. Using a domain width of 50 m, O_2 penetrates approximately 9 m (in the vertical direction) into the reducing zone instead of approximately 12 m as found previously. Also, a slightly larger maximum alteration width is attained with a domain width of 50 m. The mass of biotite and chlorite dissolved decreases slightly for the simulation with a wider domain, while the mass of pyrite dissolved increases (Table D. 1).
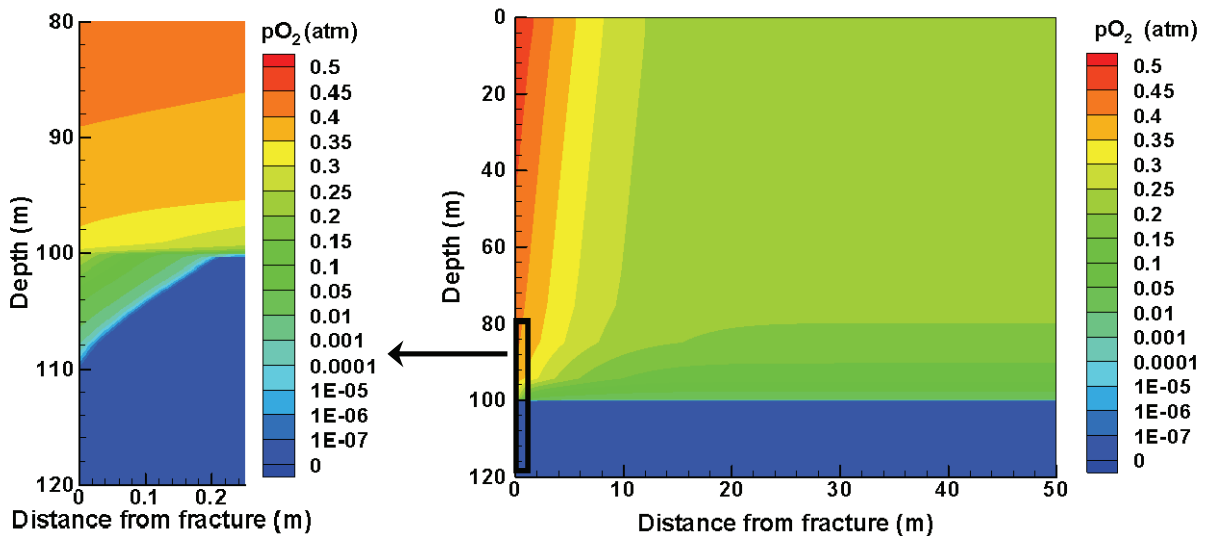
Figure D. 1: pO_2 distribution at 12,000 years (base case simulation with a domain width of 50 m).

Table D. 1: Comparison of selected results for rock matrix widths of 3 m and 50 m.

Result	Domain width	
	3 m	50 m
Approximate O_2 penetration depth into the reducing zone (m)	12	9
Max. matrix alteration width (cm)	18	20
Amount of biotite dissolved (mol)	9.352	8.600
Amount of pyrite dissolved (mol)	0.057	0.110
Amount of chlorite dissolved (mol)	0.175	0.140

D.2 EFFECT OF GRID DISCRETIZATION

The Stage I base case was also simulated for several alternative domain discretizations to explore the sensitivity of selected results. Simulations were first conducted with a simplified reaction system and a matrix width of (0.5 - 5 x 10^{-5}= 0.49995) m. The discretization of the matrix perpendicular to the fracture was varied for each simulation, encompassing a range from

1 to 1000 cells. In comparison, the base case matrix zone was subdivided into 25 cells (Section 3.1.4).
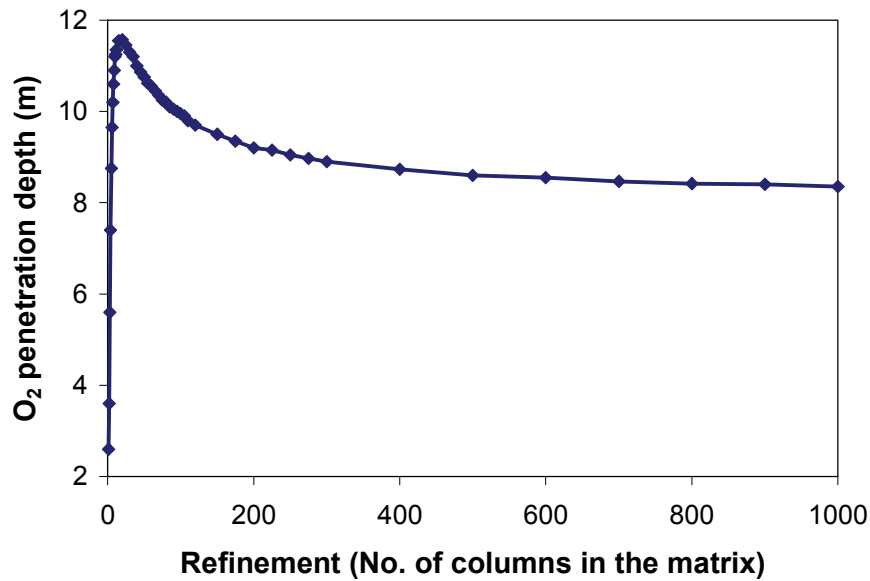
Figure D. 2: O_2 penetration depth as a function of grid refinement perpendicular to fracture.
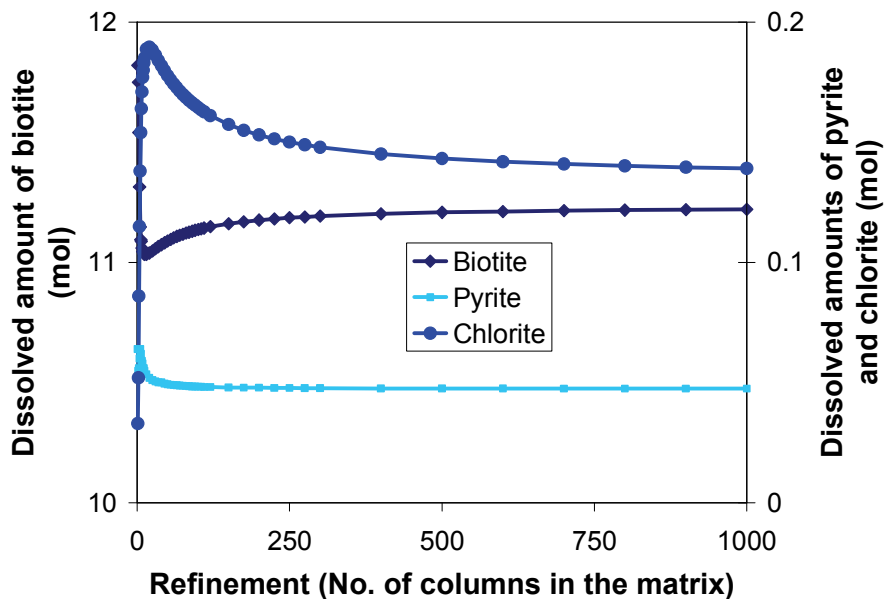
Figure D. 3: Mineral consumption as a function of grid refinement perpendicular to fracture.

From Figure D. 2, it can be seen that the O_2 penetration depth first increases with increasing grid refinement and subsequently decreases slightly. The consumption of reducing minerals

also varies slightly (Figure D. 3). Maximum O_2 penetration depths are on the order of 11.5 m for this scenario, which is consistent with the values calculated in the base case simulations. These results suggest that a coarse discretization may lead to numerical errors and an underprediction of O_2 penetration depth. The discretizations used in the current simulations appear to slightly overpredict O_2 penetration, assuming that further grid refinement leads to more accurate results.

Grid refinement in both the horizontal and vertical directions was also explored. To reduce computational times these simulations were conducted with a reduced domain of 120 m by 0.3 m, instead of 500 m by 3 m. This reduction in the domain size was found to have only a minor effect on penetration depth of O_2 (0.25 m deeper advance compared to the base case simulation with a domain of 500 m by 3 m).
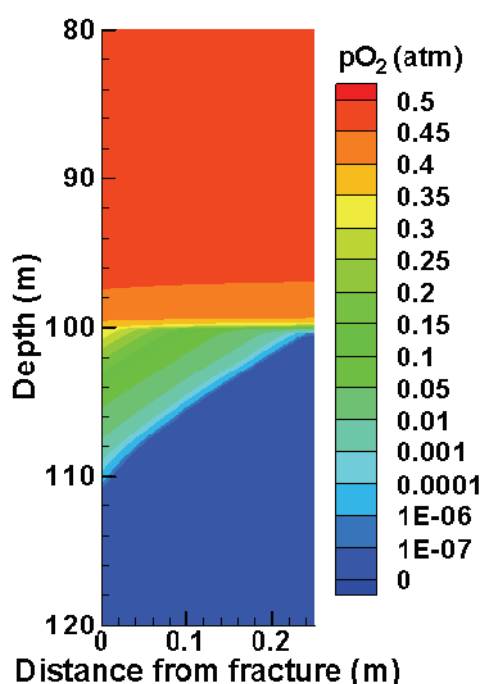
Figure D. 4: pO_2 distribution at 12,000 years (case v4h4).
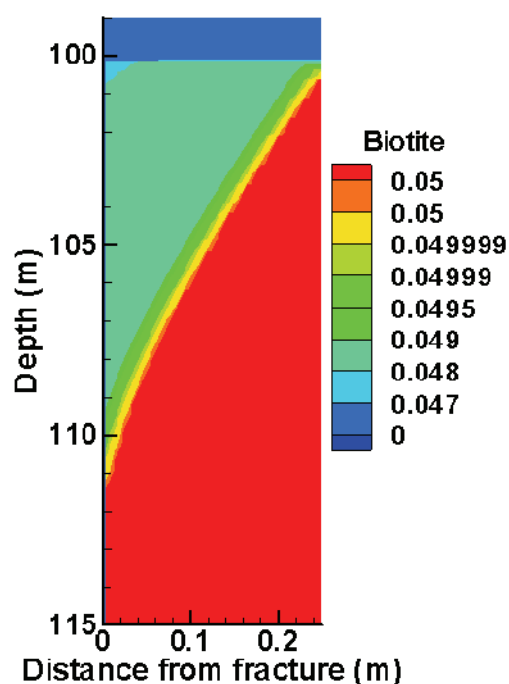
Figure D. 5: Biotite distribution at 12,000 years (case v4h4).

The results indicate that if the region where redox reactions predominately take place is discretized four times finer in the horizontal and vertical directions (case v4h4, 6588 control volumes) than shown in Figure 3-4, the edges of the wedge-shaped alteration zones of biotite and pyrite become smoother and more sharply defined (compare Figure D. 5 and Figure D. 6 to Figure 3-8 and Figure 3-9, respectively). This results in a slightly shallower pO_2 penetration depth of approximately 110 m. Further, it can be noticed that the wedge-shaped fronts do not appear as linear as previously depicted (compare Figure D. 4 to Figure 3-6).

Table D. 2 presents penetration depths for pO_2 (using a concentration of 10^{-5} atm) for various domain discretizations. For example, in case v2h2 the horizontal and vertical directions are

discretized two times finer, compared to the base case simulation, in the area where redox reactions take place. In contrast, for case v2h1, only the vertical direction is discretized two times finer compared to the base case simulation. For the various discretizations examined, a variation in pO_2 penetration depth of 1.75 m is obtained. This results in a maximum deviation of 17.5 % from the base case and is considered small compared to the uncertainty in many of the input parameters (see Stage II section). The coarser discretization used in the base case leads to deeper O_2 penetration than the simulations with the refined grids (Table D. 2), which suggests that results obtained using a coarser discretization can be considered conservative.
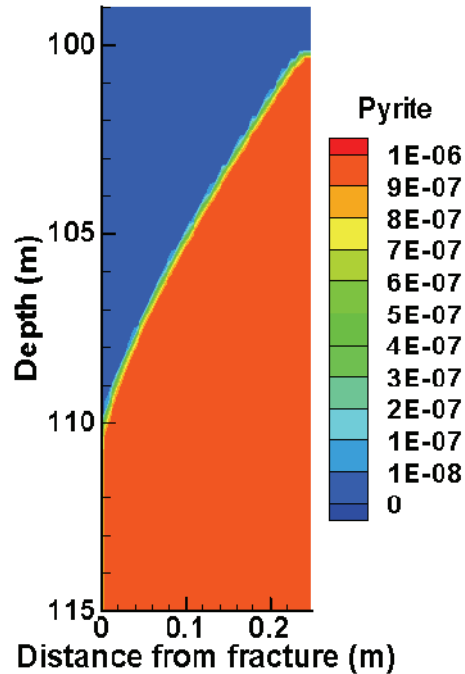
Figure D. 6: Pyrite distribution (volume fraction) at 12,000 years (case v4h4).

Table D. 2: Number of control volumes, pO_2 penetration depth, and dissolution depth of biotite for different discretizations of the base case (subdomain of 120 m by 0.3 m).

Case*	Number of control volumes	pO_2 penetration depth (m)	Dissolution depth of biotite (m)
base	704	111.75	111.75
v2h1	1024	111.50	111.75
v1h2	1302	111.50	111.75
v2h2	1984	111.00	111.00
v4h1	1664	111.50	111.50
v2h1.5	1536	111.10	111.50
v4h4	6588	110.00	110.00

*h and v refer to horizontal and vertical model domain, respectively; the numbers define how many times the region where redox reactions predominately take place is refined (see Section 3.2).

APPENDIX E   SELECTION OF pO_2 CONCENTRATION CRITERION

CONTENTS

LIST OF FIGURES

The depth of migration of dissolved oxygen in the fracture is chosen as the model response in this study. In determining an appropriate value of pO_2 for defining migration depth, several factors were considered, including:

- concentrations considered to be significant from a geochemical perspective,
- detection limit of analytical methods, and
- dissolution of the reducing minerals in the fracture (chlorite) and adjacent rock (biotite and pyrite) and subsequent precipitation of secondary minerals (e.g., goethite) during the simulations.

Gascoyne et al. (1996) suggest that concentrations of dissolved O_2 at vault depth in the Canadian Shield would be "significant" if concentrations exceeded 5 ppb ($pO_2 \sim 10^{-4}$ atm), but the expectation is that concentrations would not exceed 1 ppb. Measurements indicate less than 0.5 ppb dissolved O_2 (the limit of the analytical method) at a depth of 240 m at the URL site (Gascoyne et al. 1996).   From the perspective of microbially-mediated processes, conditions under which anaerobes can complete their life cycle without oxygen may be considered to occur when dissolved O_2 is less than 0.1% atmospheric saturation (or 0.2 uM) (Fenchel and Finlay 1995). Thus strictly anaerobic conditions would be expected at pO_2 concentrations less than $\sim 10^{-4}$ atm.

In this investigation, we have selected a pO_2 criterion of 10^{-5} atm, because it is smaller than the previously suggested significant concentrations, and is consistent with analytical detection limits. Also, for the base case simulation (Section 3), at depths where pO_2 reaches a concentration of 10^{-5} atm, no dissolution of chlorite and biotite and no precipitation of goethite are predicted. Thus 10^{-5} atm is suitable for defining the limit for alteration of the key minerals in the simulations.

To illustrate the influence of choosing alternative values for the pO_2 criterion on the depth of oxygen migration, the results from uncertainty analysis 1 (Section 4) are compared in Figure E. 1. It is seen that decreasing the concentration criterion for pO_2, to values that are 1 to 3 orders of magnitude lower than 10^{-5} atm, has only a limited effect on the distribution of predicted O_2 penetration depths. This is the case, because O_2-concentrations at this stage are effectively zero.
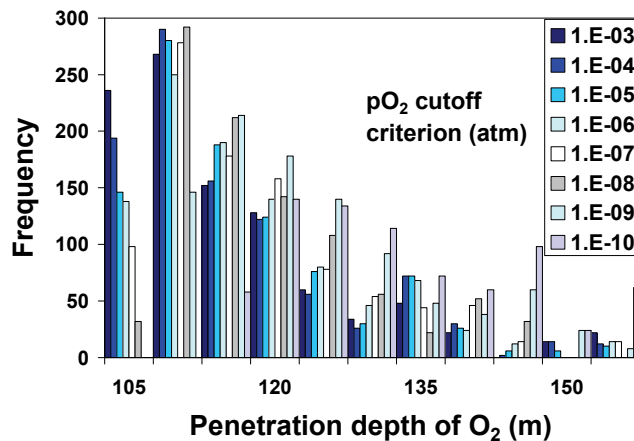
Figure E. 1: Comparison of pO_2 penetration depths for various pO_2 concentration criterions (uncertainty analysis 1).

E.1 REFERENCES

Fenchel, T., and B.J. Finlay 1995. Ecology and evolution in anoxic worlds. Oxford Series in Ecology and Evolution (edited by R.M. May and P.H. Harvey). Oxford University Press.

Gascoyne, M., J.D. Ross, and R.L. Watson, 1996. Hydrogeochemical and geochemical data for the alternative assessment case study for nuclear fuel waste disposal in Canada. AECL Technical Record TR-720, COG-95-543.

APPENDIX F   IDENTIFICATION OF MOST IMPORTANT PARAMETERS AND INTERACTIONS

CONTENTS

LIST OF FIGURES

As discussed in Section 4, factorial analysis can be applied to reveal the most important controlling parameters and parameter interactions. Probability, or effects, plots are often used for the visual determination of the most important parameters. In many cases, residual plots are used to further support the identification of important parameters and parameter interactions. This Appendix describes how the effects were calculated and how representative probability plots were constructed from the computed effects, including the procedure for finding the most appropriate transformations for the 2^k factorial analyses.

F.1 CALCULATION OF THE EFFECTS

The effects are calculated as follows: the minimum and maximum values in Table 4-1 and Table 4-2 are assigned values of -1 and +1, respectively. From these coded values, a design matrix of all possible combinations or interactions of the parameters is generated. For a 2^{10} design there are 1024 rows and 1023 columns within this design matrix and each row specifies a particular combination of parameter values to be used in a numerical simulation. Therefore, a total of 1024 simulations must be conducted for a 2^{10} factorial analysis.

Once a design matrix for the 2^{10} design is generated, the 1023 effects (i.e., 2^k-1, k = 10) can be computed by multiplying the 1024 coded values of each combination by the simulated O_2 migration depths, and dividing by 512. In essence, effects are differences between average response values for all cases at the high and low level. Specifically, a main effect of a factor is the average response value for all cases at the maximum parameter value minus the average response value for all cases at the minimum parameter value. A two-factor interaction effect can be viewed as the difference between the main effects of one factor computed at the two levels of the other factor divided by two (Devore and Farnum 1999).

When the effects are plotted against quantiles (i.e. a probability plot), the most important effects or parameters can be identified. Quantiles are computed from the cumulative frequencies (cf) of the 1024 cases as follows:

$$(\text{Quantile})_i = \text{NORMSINV}(cf_i / (n+1)) \qquad i = 1, 2, \ldots, 1024 \qquad (F.1)$$

where n is the total number of occurrences (1024), and NORMSINV refers to the inverse of the standard normal cumulative distribution. This distribution has a mean of zero and a standard deviation of one.

Uncertainty Analysis 1: Figure F. 1 shows the probability plot for Analysis 1, which is discussed in Section 4. In this figure, it can be seen that the fracture velocity (q_f) has the largest positive effect on the oxygen migration depth, while the biotite reaction rate ($k_{bio-matrix}$) has the largest negative effect.

Uncertainty Analysis 2: Figure F. 2 presents the probability plot of effects for Analysis 2, while Figure F. 3 shows only the effects for simulations in which the oxygen migration depth did not exceed 500 m.
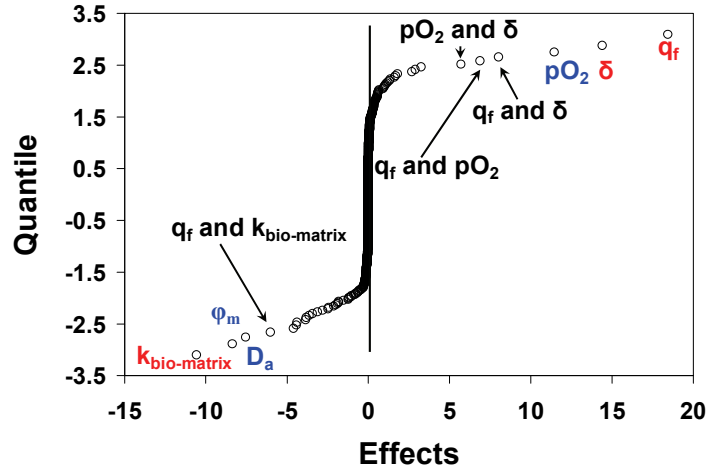
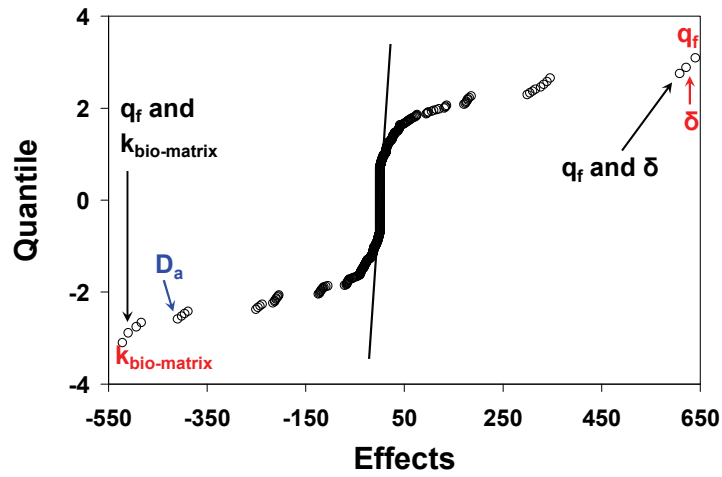**Figure F. 1: Probability plot of the effects (Analysis 1).**

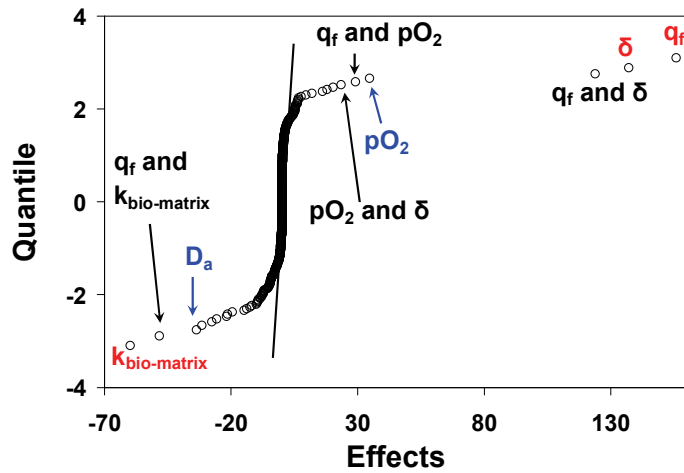**Figure F. 2: Probability plot of the effects for Analysis 2 (all results).**

Figure F. 3: Probability plot of the effects for Analysis 2 (excluding results extrapolated beyond 500m).

F.2 TRANSFORMATION

A prerequisite for the graphical examination of the most important factors is normality of the computed effects, which is typified by a well defined straight line in the effects plot. If a skewed distribution (e.g., one tail of the distribution is shorter than the other) is observed, non-normality may exist for the computed effects (Myers and Montgomery 2002). Often a transformation of the response values before calculation of the effects helps to correct the non-normality as well as inequality of variance or non-constant variance of the residuals (Montgomery 2001).
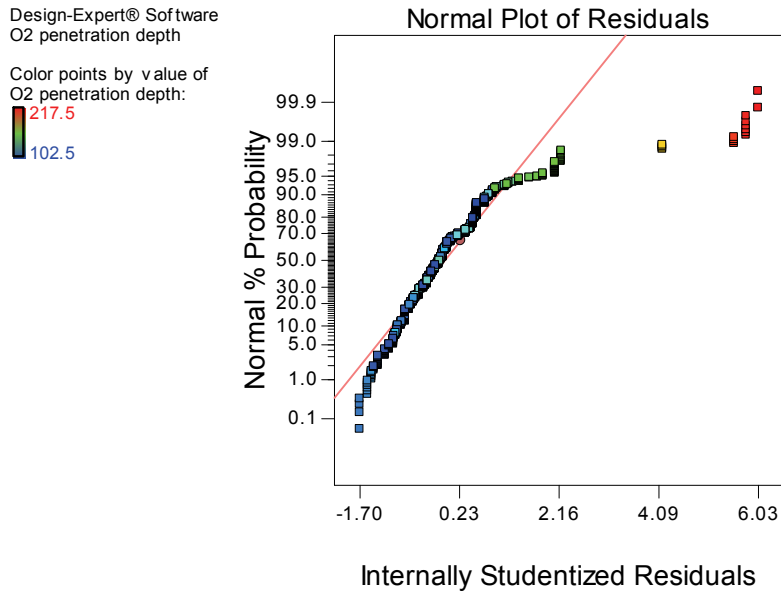
Figure F. 4: Residual plot for Analysis 1.
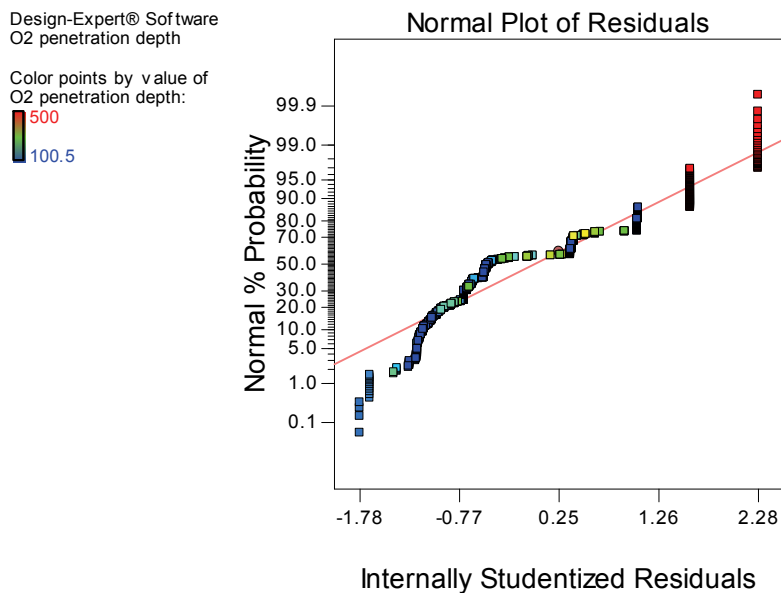
Figure F. 5: Residual plot for Analysis 2.

Figure F. 4 and Figure F. 5 show residual plots for the two uncertainty analyses; in these figures it can be noticed that numerous data points do not follow the straight line of the normal distribution. The most appropriate transformation for a particular set of effects can be found by means of a Box-Cox plot (Box and Cox 1964). In the Box-Cox procedure, a standard analysis of variance is performed for various values of lambda for the power family (y^{lambda}). The lambda values for different transformations are compared, and the value for which the error sum of squares or residual is at a minimum is suggested as the maximum likelihood estimate of lambda (Myers and Montgomery 2002). In other words, in a Box-Cox plot, the error sum of squares is plotted versus the different values of lambda used in the computation of the power family. For the generated relationship in such a plot, the minimum value of lambda within the confidence interval is the best value for lambda. Values of lambda near one indicate that no transformation is required.

Analysis 1. For the narrower range of values used in Analysis 1, the Box-Cox plot (Figure F. 6) suggests a lambda value that falls outside of the ± 3 range implemented in Design Expert®. However, both the effects and residuals fit a normal distribution much more closely with the use of a power transformation with a lambda of -3 than was the case with the untransformed data (compare. Figure F. 7 with Figure F. 4).

Analysis 2. The Box-Cox plot (Figure F. 8) for Analysis 2 suggests a lambda of -2.24, which indicates that a transformation of the form (pO$_2$ penetration depth)$^{-2.24}$ is the most appropriate. When extrapolated values for the cases where oxygen penetrates beyond 500 m are used in the computation of the effects, the Box-Cox plot suggests a slightly lower value of lambda of -1.69.
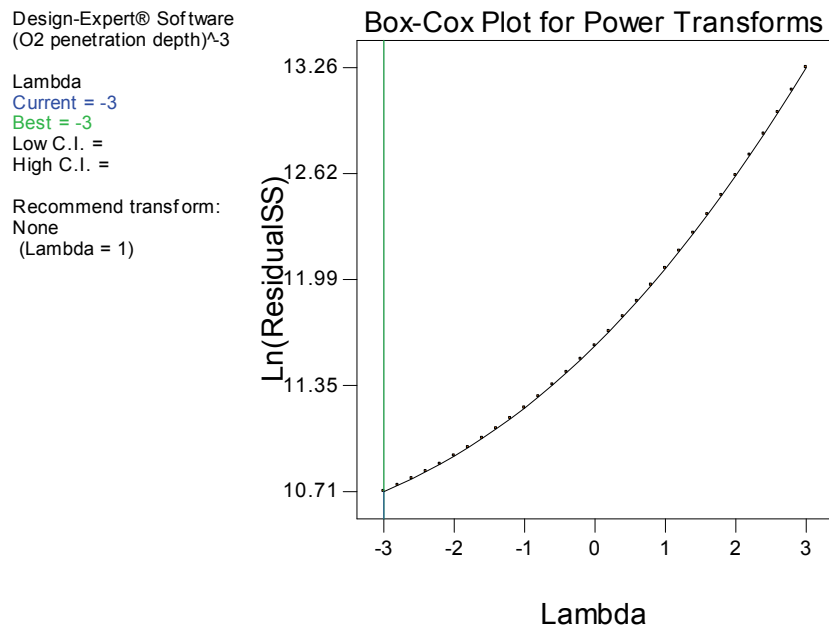
Figure F. 6: Box-Cox plot for Analysis 1.

Design-Expert® Software
(O2 penetration depth)^-3

Color points by value of
(O2 penetration depth)^-3:

9.28599E-007

9.71901E-008

Normal Plot of Residuals

Normal % Probability

99.9
99.0
95.0
90.0
80.0
70.0
50.0
30.0
20.0
10.0
5.0

1.0

0.1

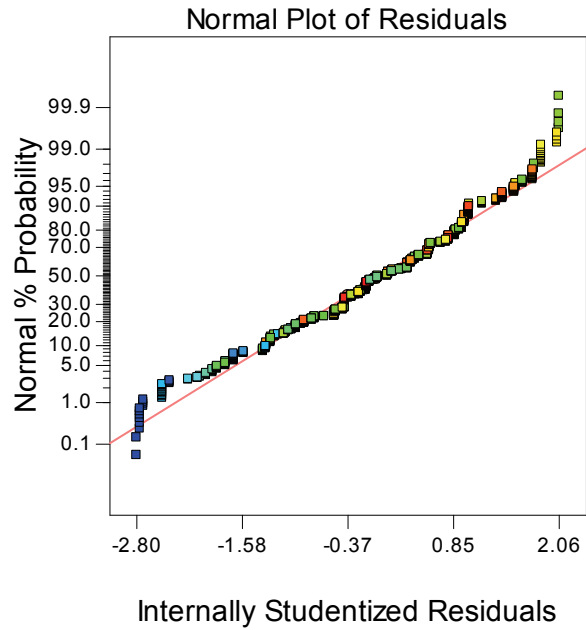-2.80   -1.58   -0.37   0.85   2.06

Internally Studentized Residuals

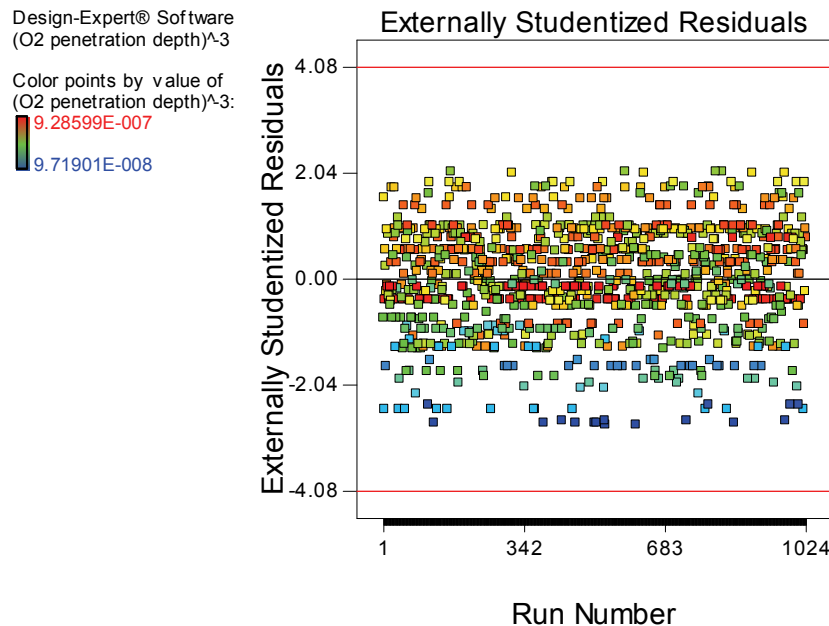**Figure F. 7: Residual plot for Analysis 1 with power transformation, lambda = -3.**

Design-Expert® Software
(O2 penetration depth)^-2.24

Lambda
Current = -2.24
Best = -2.24
Low C.I. = -2.4
High C.I. = -2.08

Recommend transform:
Power
 (Lambda = -2.24)

Box-Cox Plot for Power Transforms

Ln(ResidualSS)

19.09

17.75

16.40

15.06

13.72

-3   -2   -1   0   1   2   3

Lambda
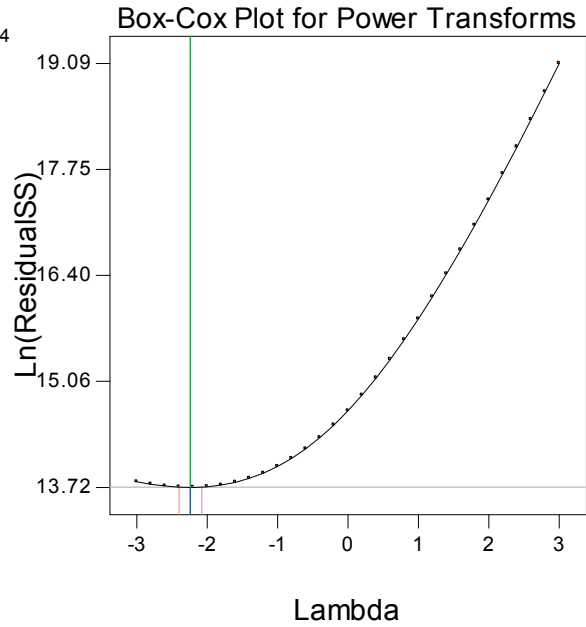
Figure F. 8: Box-Cox plot for Analysis 2.

F.3 IMPORTANT PARAMETERS AND PARAMETER INTERACTIONS

Analysis 1. For the factor of two range in parameter values considered in Analysis 1, the probability, and internally and externally studentized residual plots confirm that q_f, δ and $k_{bio-matrix}$ are the most important parameters. The residuals are linearly distributed in the internally studentized residual plot (Figure F. 7) and the externally studentized residuals remain in the control limits of ± 3 (i.e., maximum value: 2.06, minimum value: -2.81, Figure F. 9).

The probability plot (Figure 4-1) indicates that three additional parameters may be important; these are the apparent diffusion coefficient (D_a), porosity of the rock matrix ($φ_m$), and oxygen concentration in the recharge water during the period of glacial melt water production (pO_2). Figure F. 10 shows a residual plot when these parameters are selected in addition to q_f, δ and $k_{bio-matrix}$.   A S-shape can be noticed in this plot which indicates that the residuals do not follow a normal distribution. The externally studentized residual plot also demonstrates that some points are outside of the control limit of -3 (i.e., -3.2, Figure F. 11). Interestingly, if D_a, $φ_m$ and pO_2 are individually added, or only two of these are added, to the most important parameters (q_f, δ and $k_{bio-matrix}$), the studentized residuals remain within the control limits of ± 3 in the externally studentized residual plot. This finding indicates that D_a, $φ_m$ and pO_2 are important, but not as important as q_f, δ and $k_{bio-matrix}$.

With regard to parameter interactions, the best externally studentized residual plot (not shown) can be obtained when the following interactions are regarded as important: q_f and δ, q_f and pO_2, pO_2 and δ, q_f and $k_{bio-matrix}$. It should be noted that these parameters have already been individually identified as being important.

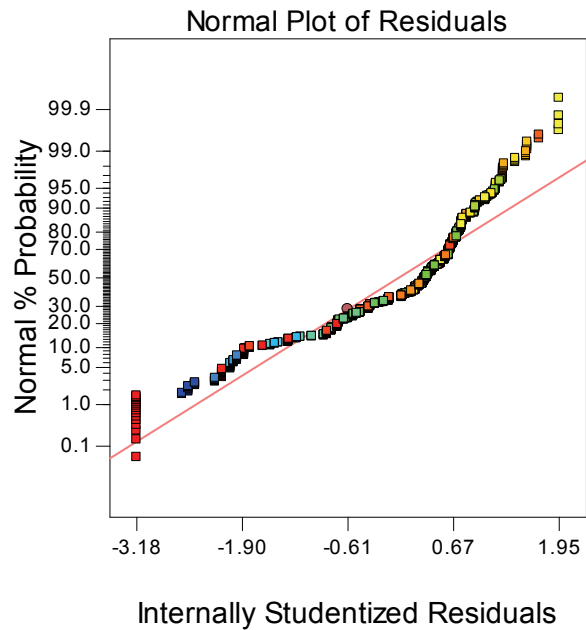**Figure F. 9: Externally Studentized Residuals for Analysis 1 with power transformation, lambda = -3.**

Figure F. 10: Residual plot for Analysis 1 with power transformation, lambda = -3 (D_a, φ_m and pO_2 included in regression model).
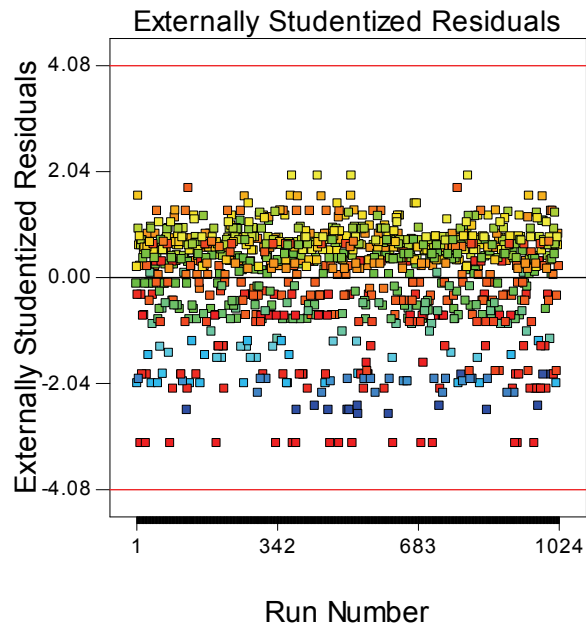

Figure F. 11: Externally Studentized Residuals for Analysis 1 with power transformation, lambda = -3 (D_a, φ_m and pO_2 included in regression model).

Analysis 2. For the wider range of values considered in Analysis 2, the resulting probability plot and externally studentized residual plot also indicate that fracture velocity during period of melt water production (q_f), fracture half-aperture (δ) and biotite reaction rate $k_{bio\text{-}matrix}$ may be the most important parameters. These parameters lie far from the straight line in the probability plot (Figure 4-2). When these parameters are included in the response model, the external residuals remain within the control limits of ± 3 (i.e., maximum value: 2.12, minimum value: -2.73, Figure F. 12). The internally studentized residual plot could be better but may be accepted as reasonable (Figure F. 13).

The probability plot suggests that there may be one more important parameter (apparent diffusion coefficient, D_a) and two important parameter interactions (q_f and $k_{bio\text{-}matrix}$, q_f and δ). If only D_a, or D_a and the interaction q_f and $k_{bio\text{-}matrix}$, are included in addition to the most important parameters (q_f, δ and $k_{bio\text{-}matrix}$), the residual plots are somewhat improved (Figure F. 14 and Figure F. 15) compared to Figure F. 13. For both cases the external residuals remain within the control limits of ± 3 (i.e., including D_a: maximum value: 2.34, minimum value: -2.55, including D_a, q_f and $k_{bio\text{-}matrix}$: maximum value: 2.19, minimum value: -2.85). Consideration of the interaction q_f and δ worsens the residual plot (results not shown), with some external residuals falling outside of the control limits of ± 3, e.g., maximum value: 2.48, minimum value: -4.23).

In summary, based on the analysis presented here, the parameters q_f, δ and $k_{bio\text{-}matrix}$ appear to be the most important ones. D_a and the interaction q_f and $k_{bio\text{-}matrix}$ also seem to be important.
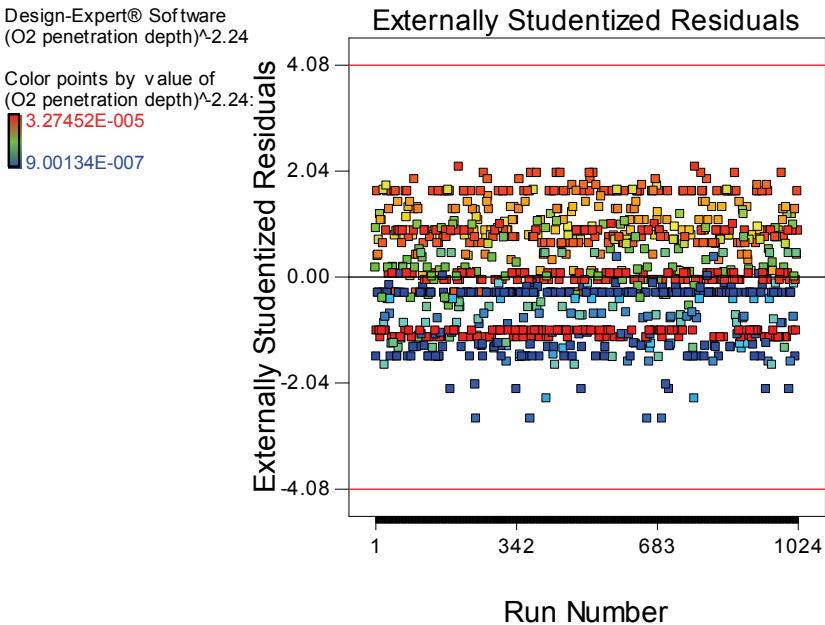

Figure F. 12: Externally Studentized Residuals for Analysis 2 and a power transformation, lambda = -2.24.

Design-Expert® Software
(O2 penetration depth)^-2.24
Std # 941 Run # 203
X: 2.112
Y: 99.85

Color points by value of
(O2 penetration depth)^-2.24:
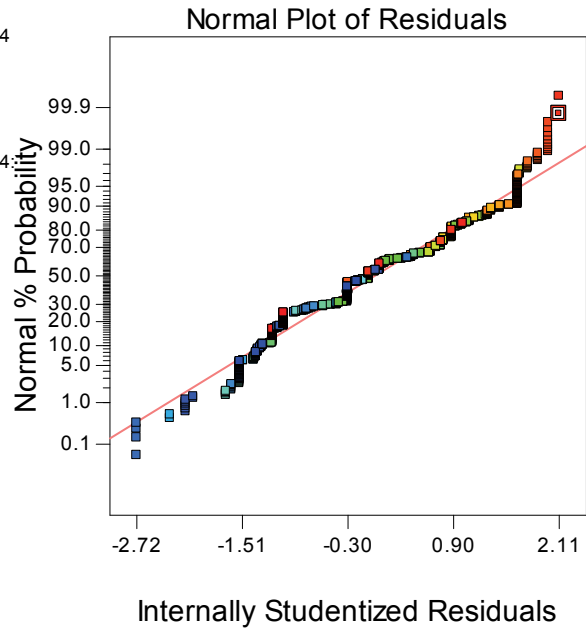3.27452E-005
9.00134E-007

Figure F. 13: Residual plot for Analysis 2 and a power transformation, lambda = -2.24.

Design-Expert® Software
(O2 penetration depth)^-2.24

Color points by value of
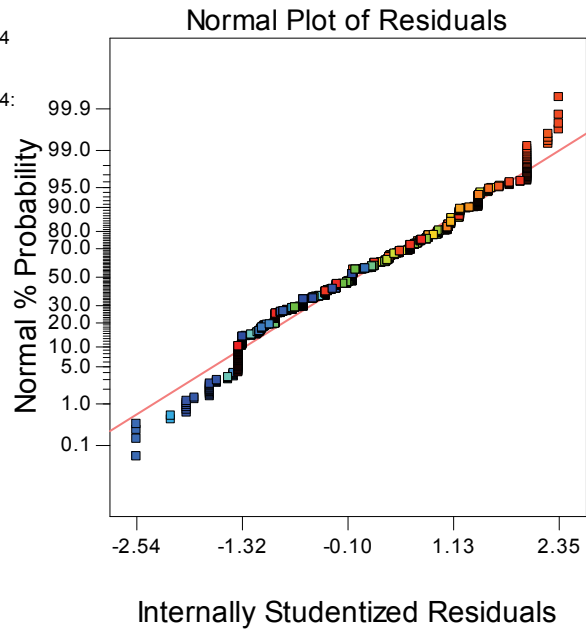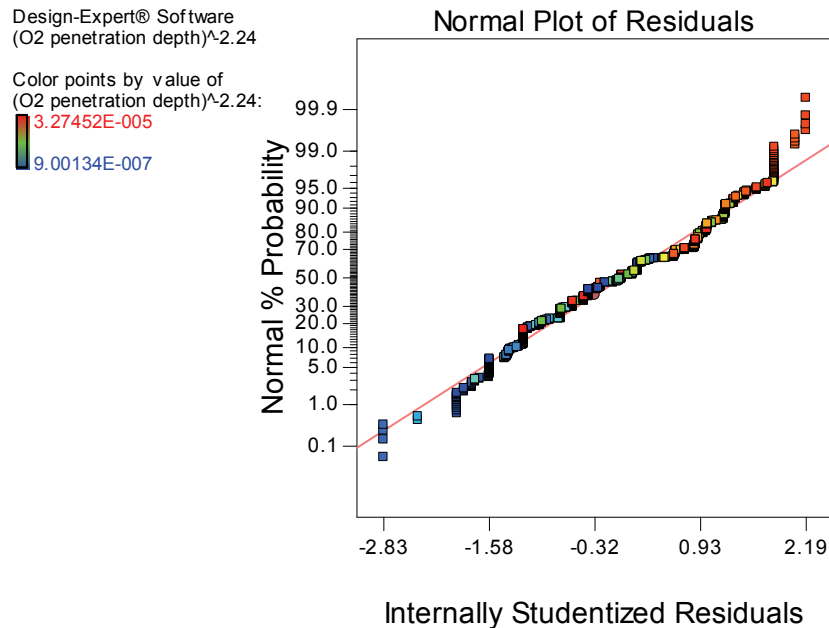(O2 penetration depth)^-2.24:
3.27452E-005
9.00134E-007

Figure F. 14: Residual plot for Analysis 2 and a power transformation, lambda = -2.24 (D_a included in regression model).

Design-Expert® Software
(O2 penetration depth)^-2.24

Color points by value of
(O2 penetration depth)^-2.24:
3.27452E-005
9.00134E-007

Figure F. 15: Residual plot for Analysis 2 and a power transformation, lambda = -2.24 (D_a and the interaction q_f and $k_{bio-matrix}$ included in regression model).

F.4 REFERENCES

Box, G.E.P. and Cox, D.R. 1964. An analysis of transformation. J. Roy. Statist. Soc. Ser. A., 26: 211-252.

Devore, J.L., and N.R. Farnum. 1999. Applied Statistics for Engineers and Scientists. Duxbury Press, an imprint of Brooks/Cole Publishing Company.

Montgomery, D.C., 2001. Design and Analysis of Experiments, 5th Edition. Wiley-Interscience Publication. John Wiley & Sons, Inc.

Myers, R.H. and D.C. Montgomery. 2002. Response Surface Methodology: Process and Product Optimization Using Designed Experiments. Second Edition. Wiley-Interscience Publication. John Wiley & Sons, Inc.

APPENDIX G   SCALING OF PARAMETERS FOR THE STAGE III DCM

CONTENTS

For parameterization of the DCM, it is necessary to scale the model parameters based on parameter values used in the DFM simulations. The following calculations outline this approach for a DFM-simulation that contains one fracture (aperture of 1×10^{-4} m) in a 1 m-wide matrix block extending to a depth of 500 m. The DCM contains two regions (mobile and immobile), each having a width of 1 m and a total depth of 500 m.

Scaling of porosity. Gerke and van Genuchten (1993) provide the following formula for total porosity (φ_t):

$$\varphi_t = w_f \varphi_f + (1 - w_f)\varphi_m \tag{G.1}$$
$$\text{where } w_f = V_f / V_t$$

w_f represents the volumetric weighting factor, φ_f is the porosity of the discrete fracture (1.0), and φ_m is the porosity of the matrix in the DFM (5×10^{-3}). Substituting respective values from the DFM into Eq.G.1 yields:

$$w_f = V_f / V_t = (1 \times 10^{-4}\, m * 1\,m * 500\,m) / (1\,m * 1\,m * 500\,m) = 1 \times 10^{-4}$$

$$\varphi_t = w_f \varphi_f + (1 - w_f)\varphi_m = 1 \times 10^{-4} * 1.0 + (1 - 1 \times 10^{-4}) * 5 \times 10^{-3}$$
$$= 0.0050995$$

The mobile fraction, $m_{f\text{-}DCM}$ may be calculated from:

$$m_{f\text{-DCM}} = (\varphi_f V_f)/(\varphi_t V_t) \tag{G.2}$$

Using the above value of φ_t in Eq. G.2 yields a value of $m_{f\text{-}DCM}$ = 0.01961 (= 1×10^{-4} / 0.0050995).

Porosity in the mobile region (fracture, $\varphi_{f\text{-}DCM}$) and immobile region (matrix, $\varphi_{m\text{-}DCM}$) of the DCM may be computed via the following formulas:

$$\varphi_{f\text{-DCM}} = m_{f\text{-DCM}}\, \varphi_t \tag{G.3}$$

$$\varphi_{m\text{-DCM}} = \varphi_t - \varphi_{f\text{-DCM}} \tag{G.4}$$

Substituting the values for φ_t and $m_{f\text{-}DCM}$ into Eq. G.3 and G.4 provides $\varphi_{f\text{-}DCM}$ = 1×10^{-4} and $\varphi_{m\text{-}DCM}$ = 0.0049995.

Scaling of velocity. The Darcy velocity is calculated such that the same mass loading exists for the DCM and DFM. Similar to the DFM, recharge is only applied to the fracture in the DCM. The fracture velocity of the DCM ($q_{f\text{-}DCM}$) may be expressed as follows:

$$(q_{f\text{-}DCM})_i \ = \ A_f \, / \, A_{f\text{-}DCM} \,{}^*(q_f)_i$$

$$= \ 1 \times 10^{-4} \text{ m} \,{}^* \ 1 \text{ m} \, / \, (1 \text{m} \,{}^* 1 \text{m}) \,{}^*(v_f)_i \ = \ 1 \times 10^{-4} \,{}^*(q_f)_i$$

$$i = \text{interglacial period and period of meltwater production} \qquad (G.5)$$

where A_f and $A_{f\text{-}DCM}$ refer to the fracture area in the DFM and DCM, respectively. Consequently, Eq. G.5 yields the following Darcy velocities for the DCM: 1 x 10^{-4} m yr^{-1} and 1 x 10^{-3} m yr^{-1} for the interglacial period and period of melt water production, respectively.

Scaling of mineral volume fractions. Mineral volume fractions are determined by equating the initial mineral mass for the DCM and DFM. For biotite and pyrite there are only minor changes in volume fractions as there is only a minor change in the width of the matrix, i.e., 1 m for the DCM versus (1 - 1 x 10^{-4}) m for the DFM. For chlorite there is a significant difference in volume fractions because the fracture width for the DFM is 1 x 10^{-4} m compared to a mobile region width of 1 m for the DCM.

Mineral mass is computed by multiplying mineral volume fraction by density and molecular weight of the respective mineral, and by domain volume occupied by the respective mineral. For both models the density and molecular weight of the same mineral are equal; consequently, the mineral volume fractions for the DCM ($f_{mineral\text{-}DCM}$) may be expressed as follows:

$$f_{mineral\text{-}domain\text{-}DCM} \ = \ \text{Domain}_{mineral} \, / \, \text{Domain}_{mineral\text{-}DCM} \,{}^* \ f_{mineral\text{-}domain} \qquad (G.6)$$

For example, for biotite in the reducing zone:

$$f_{bio\text{-}matrix\text{-}DCM} \ = \ \text{Domain}_{bio\text{-}matrix} \, / \, \text{Domain}_{bio\text{-}matrix\text{-}DCM} \,{}^* \ f_{bio\text{-}matrix}$$

$$= \ (1 - 1 \times 10^{-4}) \text{ m} \,{}^* \ 1 \text{ m} \,{}^* \ 400 \text{ m} \, / \, (1 \text{m} \,{}^* \ 1 \text{m} \,{}^* \ 400 \text{ m}) \,{}^* \ 0.05$$

$$= \ 0.049995 \approx 0.05 \qquad (G.7)$$

for pyrite in the reducing zone:

$$f_{pyr\text{-}matrix\text{-}DCM} \ = \ \text{Domain}_{pyr\text{-}matrix} \, / \, \text{Domain}_{pyr\text{-}matrix\text{-}DCM} \,{}^* \ f_{pyr\text{-}matrix}$$

$$= \ (1 - 1 \times 10^{-4}) \text{ m} \,{}^* \ 1 \text{ m} \,{}^* \ 400 \text{ m} \, / \, (1 \text{m} \,{}^* \ 1 \text{m} \,{}^* \ 400 \text{ m}) \,{}^* \ 1 \times 10^{-6}$$

$$= \ 9.999 \text{ x } 10^{-7} \approx 1 \times 10^{-6} \qquad (G.8)$$

and for chlorite in the fracture (mobile) region:

$$f_{chlo\text{-}fracture\text{-}DCM} \ = \ \text{Domain}_{chlo\text{-}fracture} \, / \, \text{Domain}_{chlo\text{-}fracture\text{-}DCM} \,{}^* \ f_{chlo\text{-}fracture}$$

$$= \ (1 \times 10^{-4} \text{ m} \,{}^* \ 1 \text{ m} \,{}^* \ 400 \text{ m}) \, / \, (1 \text{m} \,{}^* \ 1 \text{m} \,{}^* \ 400 \text{ m}) \,{}^* \ 0.1$$

$$= \ 1 \text{ x } 10^{-5} \qquad (G.9)$$

Scaling of reaction rates. The reaction rates for biotite and pyrite for the DCM are computed using the scaled values for mineral volume fractions ($f_{bio-matrix-DCM}$ = 0.049995 and $f_{pyr-matrix-DCM}$ = 9.999 x 10^{-7}) and porosity for the matrix domain (φ_{m-DCM} = 0.0049995). Values of 3.71 x 10^{-14} mol L^{-1} bulk s^{-1} and 1 x 10^{-12} mol L^{-1} bulk s^{-1} are obtained for the biotite reaction rate (= $10^{-12.25}$ mol m^{-2} s^{-1} * 1 m^2 g^{-1} * 2.65 g cm^{-3} * 1000 cm^3 L^{-1} *(1-0.0049995) / 2,000 * 0.049995) and pyrite reaction rate (= $10^{-7.42}$ mol m^{-2} s^{-1} * 1 m^2 g^{-1} * 2.65 g cm^{-3} * 1000 cm^3 L^{-1} *(1-0.0049995) / 100 * 9.999 x 10^{-7}) for the DCM, respectively. These values are only slightly different than the values using in the DFM.

In the computation of the chlorite reaction rate, a scaled fraction of chlorite on the fracture walls ($Fract_{chlo-wall-DCM}$) is required for the DCM. $Fract_{chlo-wall-DCM}$ is computed by equating the volume fraction of chlorite on the fracture walls of the DCM with the volume fraction of chlorite on the fracture walls of the DFM. Specifically this relationship takes the form:

$$Fract_{chlo-wall-DCM} = Domain_{chlo-fracture} / Domain_{chlo-fracture-DCM} * Fract_{chlo-wall}$$

$$= (1\times10^{-4}\,m*1\,m*400\,m)/(1\,m*1\,m*400\,m)*\ 0.2$$
$$= 2\times10^{-5} \tag{G.10}$$

Multiplying this value by the physical surface area of the fracture used for the DFM (10 m^2 L^{-1} H_2O) and by the intrinsic reaction rate of $10^{-12.25}$ mol m^{-2} s^{-1}, provides a value of 1.1 x 10^{-16} mol L^{-1} bulk s^{-1} for the chlorite reaction rate for the DCM.

G.1 REFERENCES

Gerke, H.H., and M.T. van Genuchten. 1993. A dual-porosity model for simulating the preferential movement of water and solutes in structured porous media. Water Resources Research. 29(2): 305-319.

APPENDIX H   TESTING AND PARAMETER DETERMINATION FOR FRACTURE ZONE MODELLING USING THE EPM APPROACH

CONTENTS

LIST OF FIGURES

H.1 COMPARISON OF DFM AND EPM APPROACH FOR FZ SIMULATIONS

For the factorial analysis simulations of the fracture zone (FZ) scenario, an equivalent porous medium (EPM) approach is preferable because it is computationally more efficient. Before conducting the parameter uncertainty analysis, it was investigated whether an EPM representation of the fracture zone (FZ) can be used to adequately describe the system evolution. This appendix presents an example of how discrete fracture model (DFM) parameters are scaled to obtain EPM parameters. In addition, the results from selected EPM-based and DFM simulations are compared and the applicability of the EPM for the fracture zone is assessed.

H.2 SCALING OF PARAMETERS FOR EPM-BASED FZ-SIMULATIONS

For parameterization of an EPM model of a fracture zone it is necessary to determine effective model parameters (e.g. FZ-porosity, the Darcy flux in the fracture zone, and volume fractions and reaction rates of the reducing minerals in the fracture zone). The following calculations detail the determination of EPM parameters for a fracture zone that contains 49.5 fractures (N_F = 49.5), each with an aperture of 1 x 10^{-4} m, for a half width (FZ-width) of 2.4995 x 10^{-1} m and an extent to a depth of 500 m.

FZ-porosity. The equation given by Gerke and van Genuchten (1993), as provided in Appendix G (Equation G.1), can be used to compute an effective porosity for the EPM representation of the FZ ($\varphi_{FZ\text{-}EPM}$). Substituting appropriate values from the DFM into Eq.G.1 yields:

$$w_{FZ} = V_{f\text{-}FZ}/V_{t\text{-}FZ} = (49.5 * 1 \times 10^{-4} \, m * 1 \, m * 500 \, m)/(2.4995 \times 10^{-1} \, m * 1 \, m * 500 \, m)$$
$$= 1.9803961 \times 10^{-2} \approx 2 \times 10^{-2}$$

$$\varphi_{FZ-EPM} = w_{FZ}\varphi_{f-FZ} + (1 - w_{FZ})\varphi_m = 2 \times 10^{-2} * 1.0 + (1 - 2 \times 10^{-2}) * 5 \times 10^{-3}$$
$$= 2.470494 \times 10^{-2} \approx 2.47 \times 10^{-2} \tag{H1}$$

FZ Darcy flux. The fracture zone Darcy flux can be obtained from the single fracture Darcy velocity, the number of fractures, and geometric parameters (fracture zone width and aperture of individual fractures. The general formula for the FZ Darcy flux is:

$$q_{FZ} = (N_F \delta q_f)/FZ\text{-width} \tag{H.2}$$

For the parameters considered here, q_{FZ} becomes:

$$q_{FZ} = (49.5 x 10^{-4} \, m \, x 1.6 x 10^{-7} \, m/s)/2.4995 \times 10^{-1} \, m = 3.17 \times 10^{-9} \, m/s$$

EPM FZ mineral volume fractions. Similar to the formula used for scaling of mineral volume fractions for the DCM (Equation G.6), a formula for the EPM representation of the FZ can be derived from a mass balance:

$$f_{mineral-FZ-EPM} = FZ\,domain_{mineral} / domain_{mineral-FZ-EPM} * f_{mineral-domain} \tag{H.3}$$

Specifically this gives, for biotite in the reducing zone of the matrix of the FZ :

$$f_{bio-FZ-EPM} = FZ\,domain_{bio-matrix} / domain_{bio-FZ-EPM} * f_{bio-matrix}$$

$$= ((2.4995\times10^{-1} - 49*1\times10^{-4} - 5\times10^{-5})\,m * 1\,m * 400\,m)/$$
$$(2.4995\times10^{-1}\,m * 1\,m * 400\,m)* 0.05$$
$$= 0.0490098 \approx 0.049 \tag{H.4}$$

for pyrite in the reducing zone of the matrix of the FZ :

$$f_{pyr-FZ-EPM} = FZ\,domain_{pyr-matrix} / domain_{pyr-FZ-EPM} * f_{pyr-matrix}$$

$$= ((2.4995\times10^{-1} - 49*1\times10^{-4} - 5\times10^{-5})\,m * 1\,m * 400\,m)/$$
$$(2.4995\times10^{-1}\,m * 1\,m * 400\,m)* 1\times10^{-6}$$
$$= 9.80196\times10^{-7} \approx 9.80\times10^{-7} \tag{H.5}$$

and for chlorite in the reducing zone of the FZ :

$$f_{chlo-FZ-EPM} = FZ\,domain_{chlo-fracture} / domain_{chlo-FZ-EPM} * f_{chlo-fracture}$$

$$= ((49*1\times10^{-4} + 5\times10^{-5})\,m * 1\,m * 400\,m)/(2.4995\times10^{-1}\,m * 1\,m * 400\,m)* 0.1$$
$$= 1.980396\times10^{-3} \approx 1.98\times10^{-3} \tag{H.6}$$

EPM FZ reaction rates. The general formula for scaling the reaction rates is similar to Equation H.3:

$$k_{mineral-FZ-EPM} = FZ\,domain_{mineral} / domain_{mineral-FZ-EPM} * k_{mineral-domain} \tag{H.7}$$

Specifically this relationship yields, for biotite in the reducing zone of the FZ :

$$k_{bio-FZ-EPM} = FZ\,domain_{bio-matrix} / domain_{bio-FZ-EPM} * k_{bio-matrix}$$

$$= ((2.4995\times10^{-1} - 49*1\times10^{-4} - 5\times10^{-5})\,m * 1\,m * 400\,m)/$$
$$(2.4995\times10^{-1}\,m * 1\,m * 400\,m)* 3.71\times10^{-14}\,mol\,L^{-1}\,bulk\,s^{-1}$$
$$= 3.63347\times10^{-14}\,mol\,L^{-1}\,bulk\,s^{-1} \approx 3.63\times10^{-14}\,mol\,L^{-1}\,bulk\,s^{-1} \tag{H.8}$$

for pyrite in the reducing zone of the FZ :

$$k_{pyr\text{-}FZ\text{-}EPM} = FZ\,domain_{pyr\text{-}matrix} \,/ \,domain_{pyr\text{-}FZ\text{-}EPM} * k_{pyr\text{-}matrix}$$
$$= ((2.4995 \times 10^{-1} - 49*1 \times 10^{-4} - 5 \times 10^{-5})\,m * 1\,m * 400\,m)\,/$$
$$(2.4995 \times 10^{-1}\,m * 1\,m * 400\,m) * 1 \times 10^{-12}\,mol\,L^{-1}\,bulk\,s^{-1}$$
$$= 9.82612 \times 10^{-13}\,mol\,L^{-1}\,bulk\,s^{-1} \approx 9.83 \times 10^{-13}\,mol\,L^{-1}\,bulk\,s^{-1} \qquad (H.9)$$

and for chlorite in the reducing zone of the FZ :

$$k_{chlo\text{-}FZ\text{-}EPM} = FZ\,domain_{chlo\text{-}fracture} \,/ \,domain_{chlo\text{-}FZ\text{-}EPM} * k_{chlo\text{-}fracture}$$
$$= ((49*1 \times 10^{-4} + 5 \times 10^{-5})\,m * 1\,m * 400\,m)\,/$$
$$(2.4995 \times 10^{-1}\,m * 1\,m * 400\,m) * 1.12 \times 10^{-12}\,mol\,L^{-1}\,bulk\,s^{-1}$$
$$= 2.22732 \times 10^{-14}\,mol\,L^{-1}\,bulk\,s^{-1} \approx 2.23 \times 10^{-14}\,mol\,L^{-1}\,bulk\,s^{-1} \qquad (H.10)$$

H.3 COMPARISONS BETWEEN EPM AND DFM REPRESENTATIONS OF THE FRACTURE ZONE

The first comparison presented is for the case of conservative (i.e. nonreactive) transport. This comparison will therefore highlight any differences that may occur because of the different representations of the transport properties of the FZ. The comparison was made for the base case FZ scenario parameters (Table 8-1) and for a case where transport is maximized (i.e. 2 x base case Darcy flux, etc.). Figure H- 1 shows, that for the case of maximized transport, there is no visible difference in total mass outflux between the two approaches.

For reactive transport, the comparison was conducted with two values of the Darcy velocity as indicated in the FZ1 and FZ2 parameters sets given in Table 8-1. As shown in Figure H- 2, after 12,000 years the DFM results exhibit slightly deeper penetration for O_2. For the FZ2 case, the difference is approximately 4.3 m for a pO_2 value of 10^{-6} atm. The normalized biotite distribution (for the FZ2 case) within the first matrix slice in the fracture zone is also shown in Figure H- 3. It can be seen that there is very good agreement between the two distributions, although consistent with the corresponding O_2 results (Figure H- 2), the DFM results are advanced slightly. The maximum width of alteration in the unfractured matrix adjacent to the fracture zone is approximately 52 cm for both the DFM and EPM.

To investigate a more extreme case, the reactive transport comparison is also made using the worst case parameters with respect to oxygen ingress (i.e. 2*[fracture aperture], the Darcy velocity of case FZ2, 2*pO_2 for boundary condition, $D_a/2$ and 2*φ_{FZ}, $f_{bio\text{-}FZ}/2$, $f_{pyr\text{-}FZ}/2$, $f_{chlo\text{-}FZ}/2$, $k_{bio\text{-}FZ}/2$ and $k_{chlo\text{-}FZ}/2$). For this case there is a difference at the leading edge of the O_2 distributions of about 25 m after 12,000 years (Figure H- 4). This difference is considered small compared to a total O_2 penetration depth of over 430 m. Note that although a fairly good agreement has been obtained between the DFM and EPM for the cases investigated, this may not be true in general.
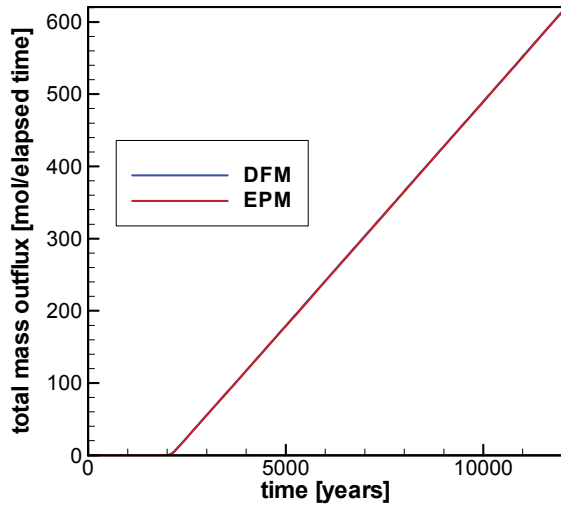
Figure H- 1: Total mass outflux versus time for conservative transport for the DFM and EPM representations of the FZ.
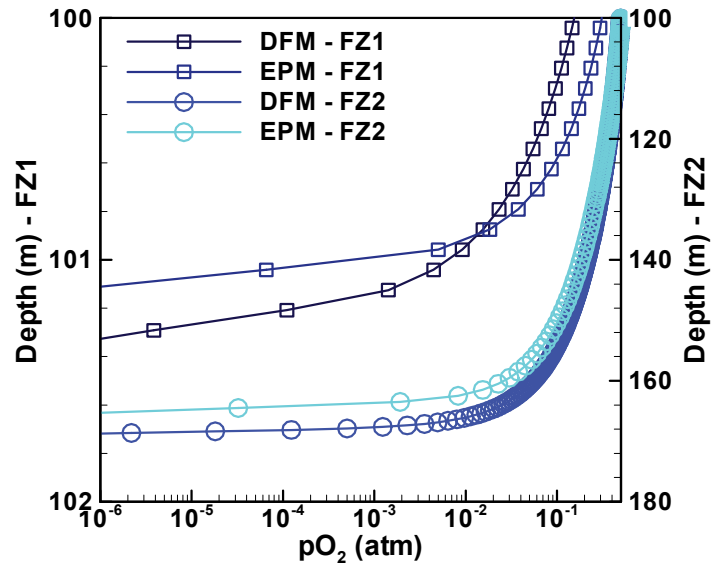
Figure H- 2: Dissolved oxygen concentration at 12,000 years for FZ1 and FZ2 Darcy velocities (see Table 8-1).
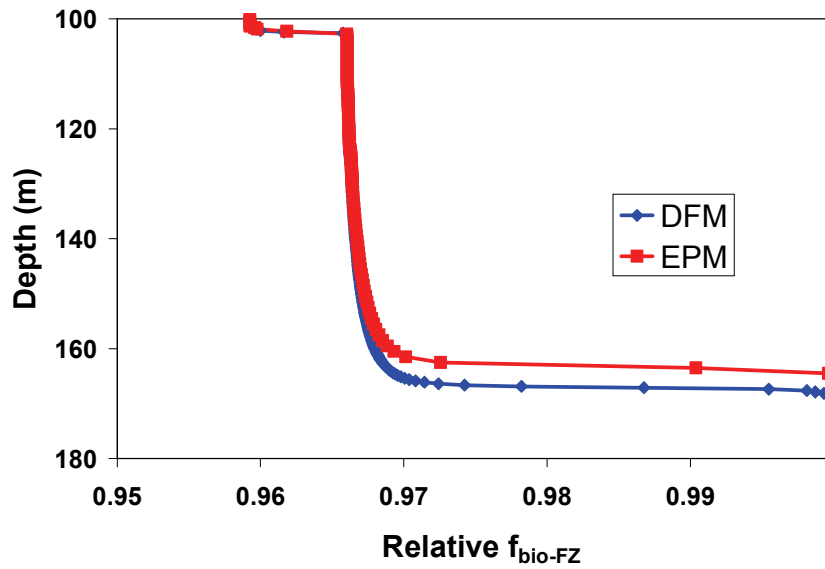

Figure H- 3: Relative biotite distribution at 12,000 years for the EPM-DFM-FZ simulation in the first column of the matrix within FZ, with the FZ2 Darcy velocity (see Table 8-1).
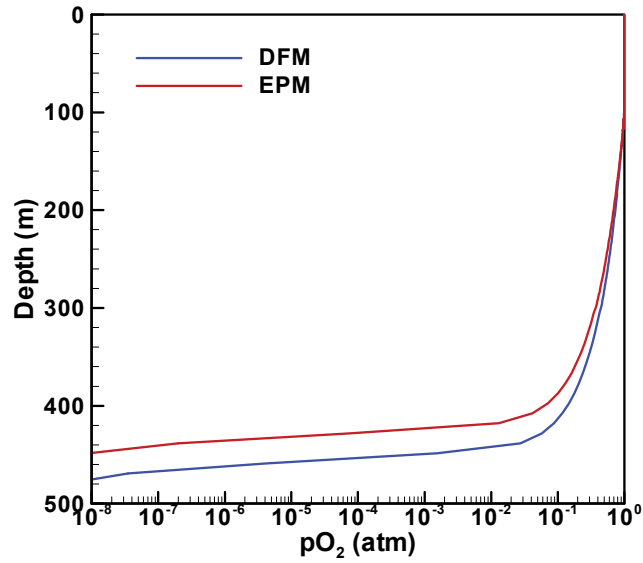
Figure H- 4: Dissolved oxygen concentration at 12,000 years for worst case reactive parameters of the fractional analysis using the DFM and EPM

H.4 REFERENCES

Gerke, H.H., and M.T. van Genuchten. 1993. A dual-porosity model for simulating the preferential movement of water and solutes in structured porous media. Water Resources Research. 29(2): 305-319.

APPENDIX I   IDENTIFICATION OF MOST IMPORTANT PARAMETERS AND INTERACTIONS FOR THE FRACTURE ZONE (FZ) SCENARIO

CONTENTS

LIST OF TABLES

LIST OF FIGURES

The analysis of the data from the fracture zone (FZ) 2^k factorial analysis parallels that discussed in more detail in Appendix F. In addition to plots of internally and externally studentized residuals, plots of residuals versus predicted values, and predicted versus actual values are used to help identify important parameters and parameter interactions. As skewed distributions could be identified in the computed effects, transformation of the response values was also required.

I.1 TRANSFORMATION

The Box-Cox plots suggest a range of optimal lambda values from -1.15 to -1.30 (selected results shown in Table I. 1) for the transformation (pO$_2$ penetration depth)^{lambda}, depending on which parameters and interactions are included in the regression model.

I.2 IMPORTANT PARAMETERS AND PARAMETER INTERACTIONS

As indicated in Figure 8-9, q_f, pO_2, $k_{bio-matrix}$ are among the most important parameters affecting O_2 ingress in the FZ scenario. The results for internally (Figure I. 1) and externally studentized residuals, residuals versus predicted values (Figure I. 2), and predicted versus actual values (Figure I. 3) support this finding. The residuals appear to be normally distributed and reasonably random when compared to the predicted values. The external residuals remain within the control limits of ± 3 (i.e., maximum value: 2.27 minimum value: -1.95; Table I. 1).

The addition of $f_{chlo-fracture}$, $k_{chlo-fracture}$, FZ-width, the combination of $k_{chlo-fracture}$ and $f_{chlo-fracture}$ or $k_{bio-matrix}$ and FZ-width to the first grouping of parameters also produces acceptable external residuals (Table I. 1), which suggests that these parameters may also be considered important. However, as more parameters are included in the regression (response) model, the plot of residual versus predicted values becomes less random and therefore less satisfactory. Although additional parameters can be added to the initial grouping (Table I. 1 provides a relative ranking based on the randomness of the residuals), these additional parameters are considered of secondary importance for the FZ scenario. This is also consistent with the relatively small deviation of these parameters from the straight line (which represents no effect on O_2 penetration depth) in Figure 8-9.

Table I. 1: Selected parameters and results from the FZ scenario factorial analysis.

| Order of important parameter groups	Parameters included in regression model	Lambda	Externally studentized residuals	
			Minimum	Maximum
1	q_f, pO_2, $k_{bio-matrix}$	-1.15	-1.95	2.27
2	q_f, pO_2, $k_{bio-matrix}$, $f_{chlo-fracture}$	-1.18	-2.41	2.03
3	q_f, pO_2, $k_{bio-matrix}$, $f_{chlo-fracture}$, $k_{chlo-fracture}$, $f_{chlo-fracture}$ & $k_{chlo-fracture}$	-1.23	-2.05	2.30
4	q_f, pO_2, $k_{bio-matrix}$ $f_{chlo-fracture}$, $k_{chlo-fracture}$, FZ-width, $f_{chlo-fracture}$ & $k_{chlo-fracture}$,	-1.27	-2.28	2.34
5	q_f, pO_2, $k_{bio-matrix}$ $f_{chlo-fracture}$, $k_{chlo-fracture}$, FZ-width, $f_{chlo-fracture}$ & $k_{chlo-fracture}$, $k_{bio-matrix}$ & FZ-width	-1.30	-2.80	2.33
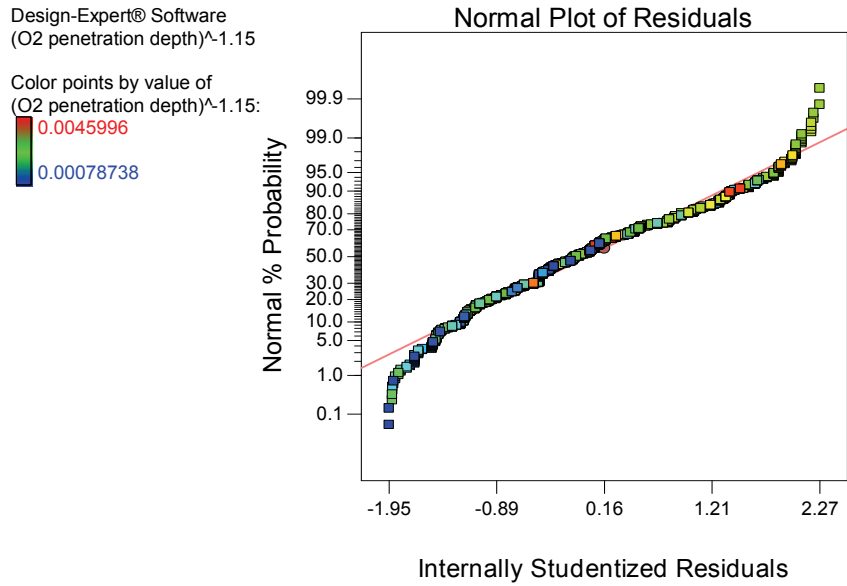
Figure I. 1: Residual plot for the FZ scenario and a power transformation, lambda = -1.15 (regression model includes: q_f, pO_2, $k_{bio\text{-}matrix}$).
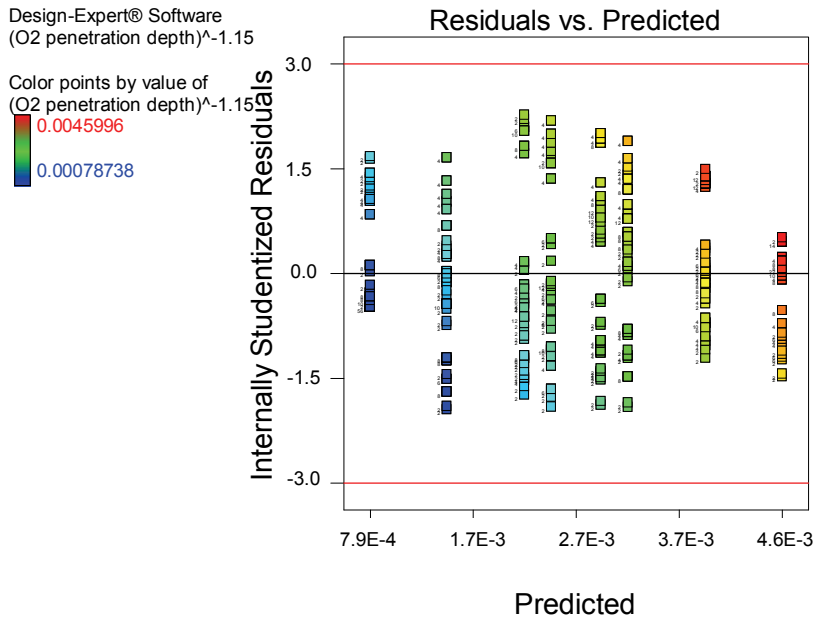

Figure I. 2: Plot of residuals versus predicted values for the FZ scenario and a power transformation, lambda = -1.15 (regression model includes: q_f, pO_2, $k_{bio\text{-}matrix}$).
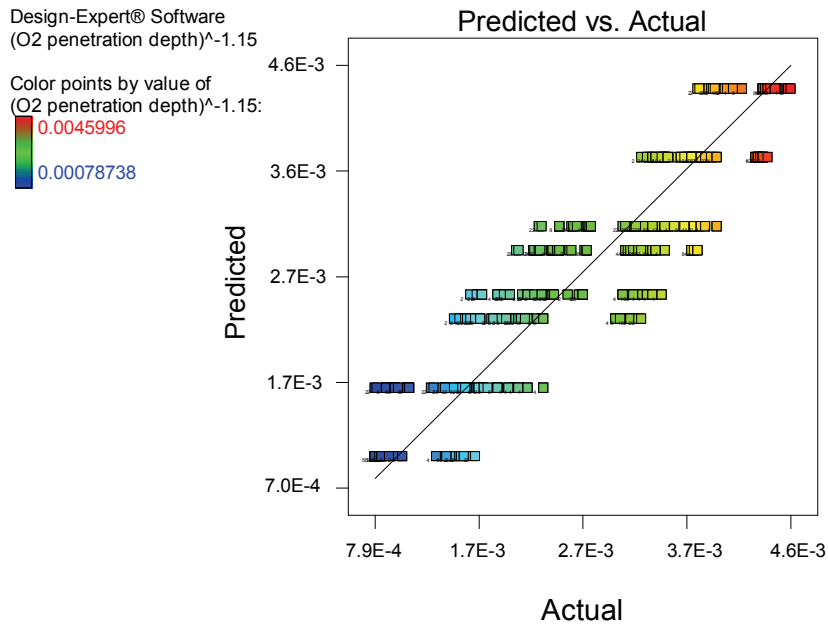
Figure I. 3: Plot of predicted versus actual values for the FZ scenario and a power transformation, lambda = -1.15 (regression model includes: q_f, pO_2, $k_{bio\text{-}matrix}$).